University of Brasilia
Physics Institute

Doctoral Thesis

Energy pathways in organic systems: From excitation to emission

Rotas energéticas em sistemas orgânicos: da excitação à emissão

Fernando Teixeira Bueno
Advisor: Prof. Pedro Henrique de Oliveira Neto
Co-Advisor: Dr. Leonardo Evaristo de Sousa

Energy pathways in organic systems: from excitation to emission

Written by

Fernando Teixeira Bueno

Presented to the Physics Institute at the University of Brasilia for obtaining the title of Doctor from the Physics Institute Graduate Program.

Physics Institute - University of Brasilia.

Brasilia. November, 2025.

“Fear is the mind-killer.”

Frank Herbert, Dune

Acknowledgments

I want to start by thanking my family; my parents, Anamaria and Roberto, my sister, Gabriela, and my grandmother, Lucia, for their support during my academic path and during my pursuit of a career related to the grand area of Physics. I am immensely grateful to my advisor Professor Dr. Pedro Henrique for all the friendship and incentive for the last eight years. I also thank my co-advisor and friend Dr. Leonardo Evaristo, without whom much of this work would not have come to fruition, for the numerous valuable contributions during my formative years in academia; he has a privileged mind and I am grateful to have had the opportunity to have worked with him very closely since he was himself a doctoral student. I thank my friend in the research group, Larissa Born, who has been on this path with me for nearly a decade and I am confident she will have a very successful career in whatever path she chooses after the conclusion of her doctorate. I thank my life long friends Laura Kuser, Thais Filgueiras, Kauê Venzi, Michella Vaz and Isabel Perez for all the friendship and support over the last 15 years; you were all vital for me to get this far. I am immensely grateful to the friends that volleyball gave me, Guilherme Rucinski, Thiago Campelo, Vinicius Nattan and Andre Luis for making all my days lighter and volleyball that much more fun, as well as for the heart to heart friendship that will no doubt continue and grow outside of the court. Since the pandemic in 2020, I have met incredible people and made incredible friends across the world through an unique online community; thank you Sahra, Melissa, Austin S., Rikki, Austin, Anders, Rosy, Felix, Jericho, Ell, Nicole S., Alysa, Nicole B., Charlotte, Owen, Brandy, Breanna, Jason, Magen and Kyn for giving me the most unexpected friendships I could ever imagine to have, each and every one of you added joy to my life over the last few years as well as relentless support and encouragement from thousands of miles away. To my dear friend, Rafael, who tragically passed away in 2023, know that your memory is forever kept in the hearts of all the friends you made; thank you for all the laughs and great moments we shared. I would also like pay my respects to late Professor Jorge Fernandes Barroso, who I carry in my memory very fondly. Lastly, I thank my late grandparents Marietta and Roberto Bueno, who I wish could be here to be a part of this moment, I am hoping they would be proud.

Abstract

The efficiency of organic optoelectronic devices depends critically on how excitons are generated, transferred, and converted between electronic states. This thesis provides a theoretical investigation of these phenomena across two complementary fronts: the mechanisms of triplet harvesting through intermolecular triplet-to-singlet (TTS) energy transfer, and the role of solvent- and environment-induced polarization in shaping electronic excitation energies.

In the first part, a complete photophysical characterization of the hostguest system composed of NPB (N,N-di(naphtha-1-yl)-N,N-diphenylbenzidine) and DCJTB (4-(dicyanomethylene)-2-tert-butyl-6-(1,1,7,7-tetramethyljulolidyl-9-enyl)-4H-pyran) was carried out. Using non-empirically tuned DFT and TD-DFT calculations combined with the nuclear ensemble method, we simulated absorption and emission spectra while including vibrational and dielectric effects. The results reveal that NPB exhibits very low reverse intersystem crossing (rISC) and nonradiative decay rates, making it simultaneously a dual emitter and an efficient donor for TTS Förster transfers. DCJTB, in turn, behaves as a strong acceptor whose triplet excitons are rapidly quenched. Calculated Förster radii confirm that TTS transfer between NPB and DCJTB is energetically viable and competitive with phosphorescence. Kinetic Monte Carlo simulations demonstrate that this mechanism alone can reproduce the experimentally observed delayed fluorescence on sub-second timescales, thus establishing TTS as a fundamental pathway for persistent luminescence in purely organic materials.

The second part extends this theoretical framework to the domain of solvatochromism. A general model for solvent susceptibility was developed to describe the stabilization of excited states by environmental polarization and to quantify non-equilibrium solvation effects. Through electronic-structure calculations for multiple donor-acceptor fluorophores, we show that the molecular susceptibility χ provides a direct measure of charge-transfer character and enables the empirical determination of dielectric constants from fluorescence spectra. This approach eliminates the reliance on empirical polarity scales such as ET(30), providing a physically grounded method to connect microscopic solute–solvent interactions with macroscopic dielectric response.

Taken together, these studies elucidate how exciton dynamics and environmental polarization act as two aspects of a single physical principle governing the behavior of excited states in molecular materials. The methodology developed — combining tuned functionals, ensemble spectroscopy, solvent susceptibility analysis, and KMC simulations — constitutes a transferable toolkit for studying excited-state phenomena in diverse environments. The findings not only clarify the mechanisms underlying triplet harvesting and solvatochromic shifts but also pave the way for the design of next–generation luminescent and sensing materials that exploit both molecular architecture and environmental effects to control emission properties.

Resumo

A eficiência de dispositivos optoeletrônicos orgânicos depende criticamente de como os éxcitons são gerados, transferidos e convertidos entre estados eletrônicos. Esta tese apresenta uma investigação teórica unificada desses fenômenos em duas frentes complementares: os mecanismos de aproveitamento de tripletos por meio da transferência intermolecular de energia tripleto-singleto (TTS) e o papel da polarização induzida pelo solvente e pelo meio na determinação das energias de excitação eletrônica.

Na primeira parte, foi realizada uma caracterização fotofísica completa do sistema *host–guest* composto por NPB (N,N-di(naftal-1-il)-N,N-difenilbenzidina) e DCJTB (4-(dicianometileno)-2-terc-butil-6-(1,1,7,7-tetrametiljulolidil-9-enil)-4H-piran). Utilizando cálculos de DFT e TD-DFT ajustados de forma não empírica, combinados ao método do ensemble nuclear, foram simulados espectros de absorção e emissão levando em conta efeitos vibracionais e dielétricos. Os resultados mostram que o NPB apresenta taxas extremamente baixas de *intersystem crossing* reverso (rISC) e de decaimento não radiativo, além de ser naturalmente um emissor duplo, o que o torna um eficiente doador para transferências TTS via mecanismo de Förster. Já o DCJTB atua como um aceitador eficaz, cujos estados tripleto são rapidamente desativados de forma não radiativa. Os raios de Förster calculados confirmam que a transferência TTS entre NPB e DCJTB é energeticamente viável e competitiva com a fosforescência. Simulações de Monte Carlo cinético demonstram que esse mecanismo, por si só, reproduz a fluorescência tardia observada experimentalmente em escalas de sub-segundo, estabelecendo TTS como um caminho fundamental para luminescência persistente em materiais orgânicos.

A segunda parte amplia esse arcabouço teórico para o fenômeno do solvatocromismo. Desenvolveu-se um modelo geral de suscetibilidade do solvente para descrever a estabilização de estados excitados pela polarização do meio e quantificar efeitos de solvatação fora do equilíbrio. Por meio de cálculos de estrutura eletrônica para diversos fluoróforos com arquitetura doador-aceitador, demonstrou-se que a suscetibilidade χ fornece uma medida direta do caráter do estados excitado — seja de transferência de carga ou de excitação localizada — e permite a inferência empírica da constante dielétrica em filmes finos a partir de espectros de fluorescência em solução. Essa abordagem elimina a dependência de escalas empíricas de polaridade, como o ET(30), oferecendo um método fisicamente fundamentado para conectar as interações microscópicas soluto-solvente à resposta dielétrica macroscópica.

Em conjunto, os estudos elucidam como a dinâmica dos éxcitons e a polarização constituem duas manifestações de um mesmo princípio físico que governa o comportamento dos estados excitados em materiais moleculares. A metodologia desenvolvida — combinando funcionais ajustados, espectroscopia de ensemble, análise de suscetibilidade de solvente e simulações de Monte Carlo cinético — forma um conjunto de ferramentas transferível para o estudo de fenômenos em estados excitados em diversos ambientes. As conclusões esclarecem os mecanismos subjacentes à conversão de tripletos e aos deslocamentos solvatocrômicos, ao mesmo tempo em que abrem caminho para o projeto de novos materiais luminescentes e sensores que exploram tanto a arquitetura molecular quanto os efeitos do ambiente para controlar suas propriedades de emissão.

CONTENTS

CHAPTER 1

OVERVIEW

Organic optoelectronics is the field concerned with using carbon-based molecular and polymeric materials to generate, control, and detect light. These systems — spanning organic light-emitting diodes (OLEDs), solar cells, lasers, and sensors — rely on the ability to convert electrical energy into optical energy and vice versa. Organic materials are appealing for several reasons, including their low–cost, solution–processable nature, but also in the tunability of their optical and electronic properties through chemical design[1, 2, 3].

At the microscopic level, when a molecule is excited, wether by absorbing light or by an electrical current, an electron gets elevated from the HOMO (Highest Occupied Molecular Orbital) to the LUMO (Lowest Unoccupied Molecular Orbital), leaving behind a hole. If the excitation is not strong enough to remove the electron, the electron-hole pair remains bounded and acts as a particle. This quasiparticle is called an exciton[4, 5, 6]. It is responsible for storing energy and diffusing through a material hopping between molecules, which allows for energy transport. The working principle of organic optoelectronic devices is governed by the creation, migration, and recombination of these excitons. In inorganic semiconductors, the dielectric screening is strong and excitons are weakly bound, often being dissociated into a free electron and a free hole too quickly, which prevents them from acting as main energy carriers in that class of materials[7, 8]. In organic semiconductors, however, the typically low dielectric constant and localized molecular orbitals lead to strongly bound excitons that must migrate via intermolecular energy transfer processes before decaying radiatively[9, 10].

The formation route of an exciton affects its spin character. When an exciton is created optically, that is, through the absorption of photons, the molecules are taken to their first singlet excited state, yielding an exciton in its singlet state. A solar panel, or organic photovoltaic device (OPV), is the most classical example of a device in which excitons are created optically. Solar panels convert light into an electrical current. When light is absorbed and singlet excitons are generated, they diffuse throughout the material by means of resonance energy transfer up until it reaches a molecular interface, where it has a probability of dissociating back into separate electron and hole — free charges — which are then collected. The Förster resonance energy transfer process between singlet excitons (S-S FRET) occurs nonradiatively and its details are discussed in chapter 2. Although the efficiency of organic based solar panels is historically low, new materials and combinations of existing materials in smart architectures are being continuously developed, still making organics a promising developing field, as shown in Figure 1.1.

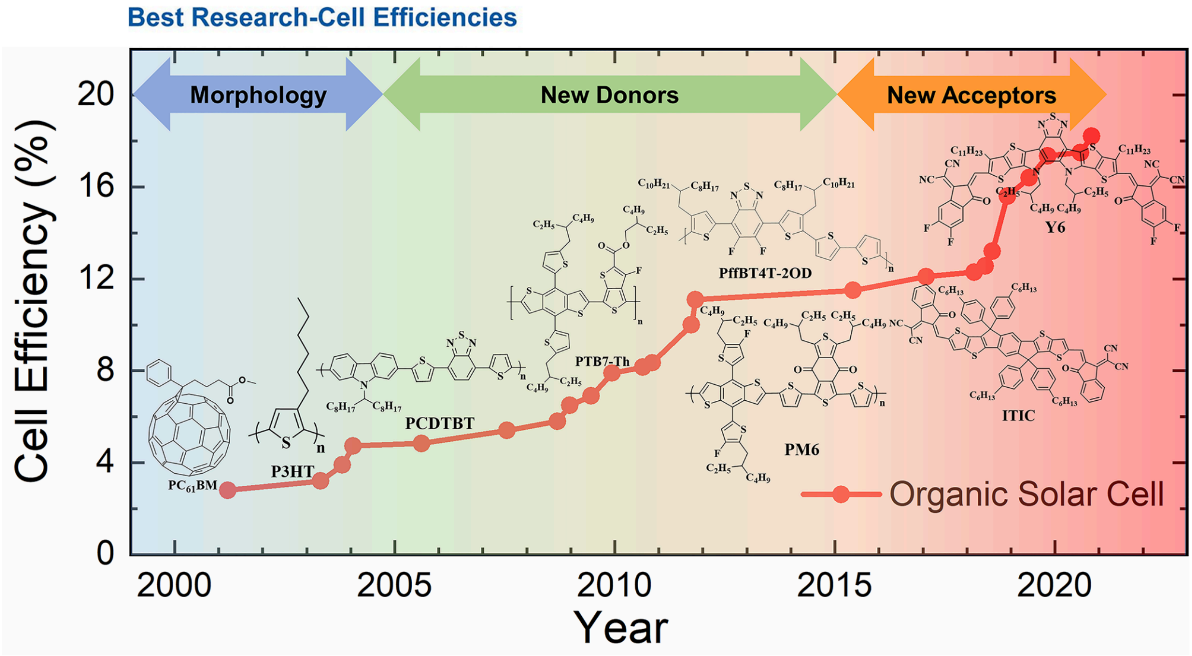

Figure 1.1: Highest certified efficiencies of organic solar cells (OSCs) recorded by the National Renewable Energy Laboratory (NREL) (USA) from 2001 to 2021. The development of OSCs has advanced via the following three stages: (i) the optimization of bulk heterojunction morphology based on P3HT:PC61BM; (ii) the development of new donors, such as PCDTBT, PTB7-Th, PffBT4T-2OD, and PM6; and (iii) the development of new nonfullerene acceptors, from the ADA-type ITIC series to the ADA DA-type Y6 series. Extracted from ref. 11.

Under electrical excitation, electrons and holes are injected into a material that, after diffusing, recombine randomly with respect to spin. Due to the nature of the eigenvalues of the spin operator, the statistics of generated excitons is of three triplets for one singlet. OLEDs are a typical example of devices where excitons are formed through electrical excitation, which are then recombined into a photon. Nevertheless, in first view, only the singlet excitons are of emissive nature in the nanosecond scale, making OLEDs have, in principle, a maximum 25% efficiency if triplet excitons cannot be harvested. The radiative decay of a singlet and a triplet exciton are known as fluorescence and phosphorescence, respectively. Fundamental research for the development of todays OLED technology can be traced back to the early 1960s when eosin was found to emit delayed fluorescence[12] and the application of high voltage to anthracene crystals succeeded in electroluminescence [13]. Although numerous organic compounds with fluorescence in the visible region were known, low efficiencies and high operating voltages had to be overcome, before the great potential of OLEDs was manifested[14]. In 1987, at Eastman Kodak, Tang et al. built the first OLED device operated at sufficiently low voltages which marks the breakthrough of OLED technology. Since then, research and development of OLED technology have continuously evolved in academia as well as in industry (see Figure 1.2).

Over the years, several strategies have been employed to promote a more efficient triplet management, such as the use of rare-earth-based phosphors and molecular complexes based on transition metals, which enhance triplet decay, although inefficiently[15, 16, 17, 18]. Alternatively, in 2012, the process of thermally activated delayed fluorescence (TADF) was observed to produce photoluminescence with high efficiency [19, 20]. This process usually consists on the up-conversion — driven by thermal energy when the energy gap between singlet and triplet states is small — of non-emissive triplets into emissive singlet state through what is known as the reverse intersystem crossing mechanism (rISC)[21, 22, 23]. Intersystem crossing (ISC) is the process in which a singlet exciton is converted to a triplet exciton, while its opposite is called rISC. However, they can only occur if there is relevant spin-orbit coupling of the two states and if the energy gap between them is small enough. TADF molecules usually follow a donor-acceptor architecture that induces a charge-transfer (CT) character to their first singlet state[24, 25, 26]. Additionally, different combinations of TADF molecules have been shown to report efficiencies of up to 100%, making it a breakthrough on triplet management.

With that in mind, it becomes clear that the efficiency of OPVs and OLEDs rely on the energy carriers having clear energy pathways for transfer and recombination. The interplay between conversion and transfer processes is paramount to determine the efficiency of a device. In order to better understand these phenomena, one must consider the specificities of the electronic structure of the materials of interest as well as the interactions of the plethora of processes that can occur in organic devices. Figure 1.3

displays the monomolecular and bimolecular processes each kind of exciton can undergo. The Förster resonance energy transfer in which a triplet exciton from a donor molecule is transferred to the acceptor molecule as a singlet exciton is known as TTS (triplet-to-singlet energy transfer). The details regarding the conditions for which said transfer can happen competitively in respect to other occurring phenomena is discussed further ahead. Lastly, it is worth noting that S_1 and T_1 states can decay nonradiatively, i.e. the excitation energy is lost to the lattice in the form of heat. Nevertheless, the rates for that kind of transition vary a great deal depending on the individual materials, as well as on the combination of donor and acceptor molecules and the competitiveness with other existing processes.

Among the many luminescence-related processes found in molecular materials, afterglow is particularly interesting. Also referred to as persistent luminescence, afterglow is defined as the emission of light that persists long after the external excitation source has ceased. Researchers have observed this phenomenon since the 18th century, prompting early theoretical explanations that ranged from the caloric theory[28, 29, 30], to the luminiferous ether[31, 32], to chemical reactions when exposed to light[33, 34], culminating in the distinct categorization of phosphorescence in the 19th century by Sir George Stokes[35]. Throughout the latter half of the 20th century, experimental studies extensively explored various facets of afterglow luminescence. Initially focused on understanding chemical reactions involving nitrogen-base compounds in the 1950s and 1960s[36, 37, 38, 39, 40], research in this field has now expanded to encompass a wide array of materials and applications. These include carbon quantum dots[41], TADF molecules[42], light-emitting diodes, solar cells[43], textile dyeing, data encryption [44], bioimaging[45, 46, 47, 48], warning signs and anti-counterfeiting [49].

Usually, afterglow is a result of late phosphorescence. As such, the efficiency of this process

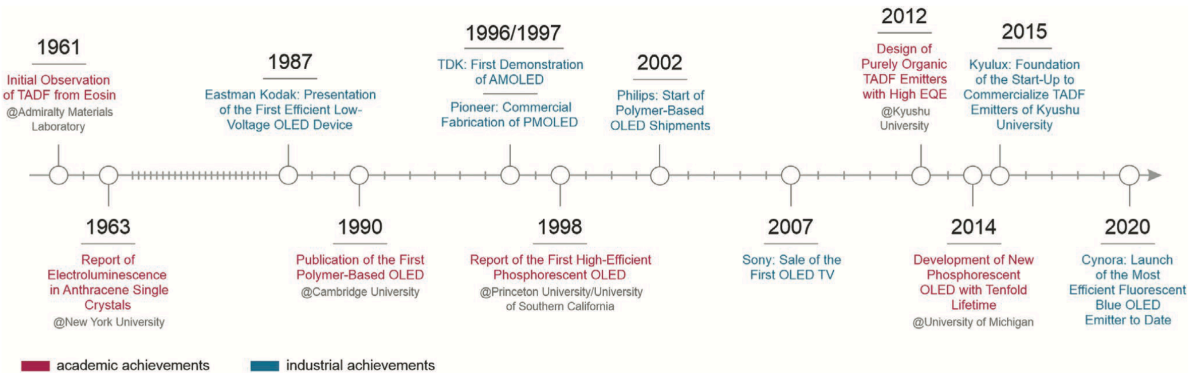

Figure 1.2: Overview of milestones in OLED technology; PMOLEDpassive matrix OLED, AMOLEDactive matrix OLED. Extracted from ref. 27.

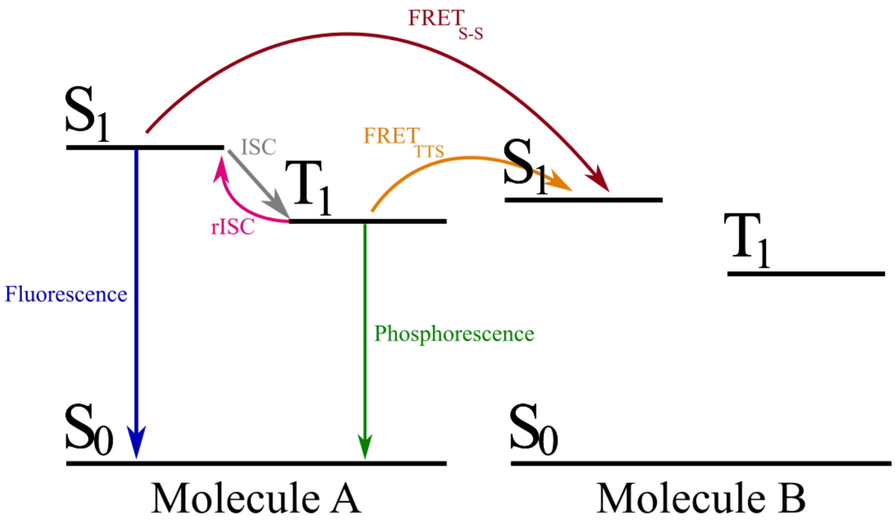

Figure 1.3: Radiative decay (fluorescence and phosphorescence), conversion (ISC and rISC) and transfer (S-S FRET and TTS FRET) processes each exciton can undergo considering two molecules.

depends on the quantum yield of triplet generation and on suppression of nonradiative decay pathways. As mentioned above, materials based on transition metals have been used for precisely that goal, since the presence of heavy atoms results in higher spin-orbit coupling and consequently higher ISC and phosphorescence rates. However, this approach increases costs and results in less sustainable devices. Furthermore, TADF has also been presented as a viable and efficient process from which afterglow can be obtained. Nevertheless, another, less popular approach relies on triplet conversion by means of the aforementioned TTS Förster transfers[50, 51].

Recently, an experimental study demonstrated the achievement of afterglow by leveraging TTS transfers between two organic compounds[52]. This host-guest system was composed of NPB [N,N-di(naphtha-1-yl)-N,N-diphenylbenzidine] (1.4-a) embedded in a rigid PMMA [poly(methyl methacrylate)] matrix, with varying concentrations of the fluorescent dye DCJTB [4-(dicyano-methylene)-2-tert-butyl-6-(1,1,7,7-tetramethyljulolidyl-9-enyl)-4H-pyran] (1.4-b). NPB is a biluminescent molecule, i.e. capable of fluorescence and phosphorescence in similar intensities, typically used as a hole-transport material in OLEDs[53, 54, 55, 56] and DCJTB is a fluorescent emitter known as an optimal dopant for a range of devices to achieve maximum fluorescence efficiency [57, 58, 59]. In this experimental setting, NPB molecules were optically excited, producing singlet excitons that converted into triplets by ISC. It was proposed that these triplet excitons migrate to DCJTB molecules by means of TTS Förster transfers, after which they fluoresce producing afterglow.

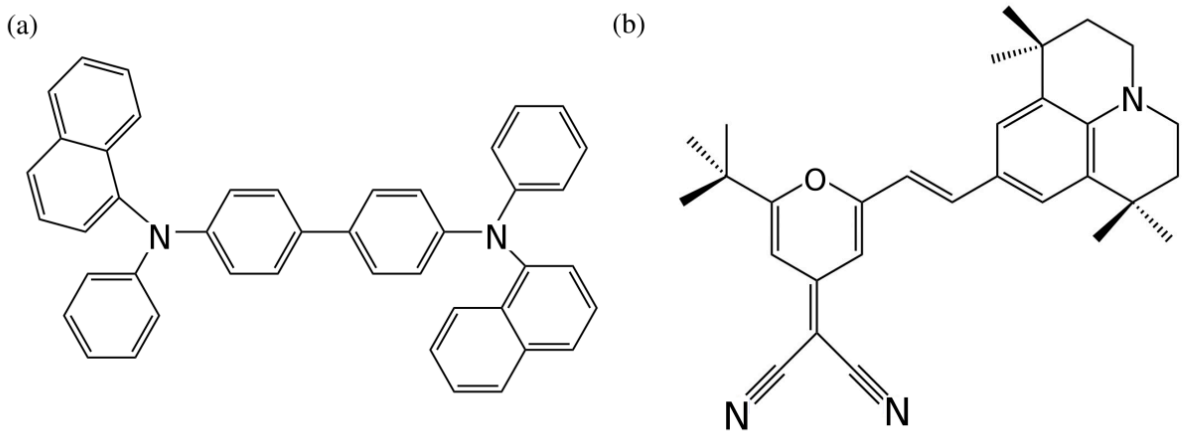

Figure 1.4: NPB [N,N-di(naphtha-1-yl)-N,N-diphenylbenzidine] (a) and DCJTB [4-(dicyano-methylene)-2-tert-butyl-6-(1,1,7,7-tetramethyljulolidyl-9-enyl)-4H-pyran] (b).

As a first system to investigate the interplay between all these phenomena, we perform a full theoretical characterization of the photophysics of NPB and DCJTB while accounting for vibrational and medium effects. We simulate absorption and emission spectra; estimate the rates of fluorescence, phosphorescence and (r)ISC for both molecules; and compute the Förster rate for regular singlet-to-singlet transfers and TTS transfers. Finally, we use the characterization results to parameterize kinetic Monte Carlo (KMC) simulations of exciton dynamics in solid films with varying relative amounts of NPB and DCJTB and varying dielectric constant. We demonstrate that rISC rates in NPB are very low and unable to explain the observed delayed fluorescence. In contrast, we show that TTS transfers are theoretically allowed and can outperform both phosphorescence and nonradiative decay in NPB, resulting in fluorescence-derived afterglow stemming from DCJTB molecules. Lastly, we track the combination of electronic and morphological properties responsible for efficient TTS transfers. These results shed light on the working of this less popular though highly relevant triplet conversion mechanism.

The detailed investigation while performing the appropriate electronic structure calculations for NPB and DCJTB, as will be detailed in Chapter 3, led us to identify a self-polarizing and solvatochromic behavior of DCJTB. That is an example of molecules that follow the donor-acceptor structure, which causes it to have a strong CT character, with a considerable spatial separation between HOMO and LUMO[60]. Due to the fact that CT states couple strongly with the dipoles of surrounding solvent molecules, their emission is highly sensitive to medium polarity and often display solvatochromism. In practice, this means that increasing solvent polarity generally induces red-shifts in fluorescence emission, providing a direct link between the photophysical response of the molecule and its environment. This realization opened the door to a broader set of questions as to how relevant the environment — its polarity, its capacity for stabilization of charge-transfer states, even subtle local interactions — is and why it was leaving a fingerprint in the form of optical signatures observed in experimental works. As a result, donor-acceptor fluorophores have been employed as environment-responsive probes for detecting changes in local polarity [61, 62].

Additionally, one of the striking aspects of solvatochromism is how diverse its applications are, spanning areas that would otherwise seem unconnected. In biology, solvatochromic probes take on a more practical role: their environment-responsive fluorescence makes them invaluable for imaging cellular compartments, mapping membrane polarity, and even tracking processes such as lipid metabolism or protein conformational changes in real time. Solvatochromism acts as a window into fundamental intermolecular interactions and as a versatile functional property that can be engineered into systems for real-world sensing, imaging and diagnostics.

In order to better understand the effects of solvent presence in transition energies, we perform multiple electronic structure calculations according to our methodology for different molecules used in several applications and provide detailed comparison with experimentally obtained fluorescence spectra. In addition, through fluorescence spectra in different solutions, we are able to empirically estimate static dielectric constants for different solid state samples. All of the procedures are detailed in the chapters to come.

This thesis is divided into four following chapters and three appendices: Chapter 2 presents the necessary general physical background regarding the theory of methods and models used in the field and in all of the investigations here performed; Chapter 3 displays the methodology and modeling employed in our first system of interest as well as their results; Chapter 4 further details the theory and the model used to investigate solvatochromic effects in a myriad of molecules used for different applications in addition to all the results that came to be upon the use of said models; Chapter 5 presents the conclusions from both studies; The appendices include relevant mathematical development of milestone expressions used throughout the text.

CHAPTER 2

PHYSICAL BACKGROUND

2.1 Framework for Rate Calculations

A solvation process is defined as the rearrangement of solvent molecules upon the insertion of a solute. How this process happens depends on how fast the solute changes state versus how fast the solvent can respond. Based on that, we can characterize a solvation process in two different kinds:

- **Equilibrium solvation**: for this process, the solvent molecules have had enough time to fully reorganize themselves around the solute's electronic structure, implying that both solute and solvent are in equilibrium with each other. For instance, a molecule in its ground state in solution implies that the solvent molecules around it are fully relaxed and oriented optimally around the solute's charge distribution and their dipole moments are, on average, aligned, depending on the solute's dipole strength and the polarity of the solvent.
- **Non-equilibrium solvation**: a case like this happens when the solute undergoes a sudden change in electronic distribution, usually due to the absorption of a photon, and the solvent molecules are not able to reorient themselves to the new charge distribution. Note that electronic transitions are much faster than nuclear motion (i.e. solvent molecules). At that point, the solute and solvent are in "different electronic states", and thus, in different configurations. With time, the solvent reorients itself to stabilize the excited state, reaching what is known as solvent relaxation.

In spectroscopy, the Stokes shift arises largely from non-equilibrium vs. equilibrium solvation (largely being the operative word here). Absorption processes from the ground state solvent arrangement are characterized as non-equilibrium with respect to excited state. On the other hand, emission processes happen after solvent relaxation around the excited state, thus, happening in equilibrium. It is worth addressing a possible point of confusion here. When we say a process occurs in equilibrium, we are referring to the fact in the initial moment, we consider the alignment and equilibrium between solvent and solute, regardless if that is the ground or excited state. As a consequence, in the final state immediately after a transition takes place, there will not yet be an equilibrium between solvent and solute. That said, in absorption processes, the initial state is S_0 and there is equilibrium with the solvent, while the final state is an excited state, but still with ground state solvation (i.e. solvent is still in the S_0 "configuration"), thus being in non-equilibrium. Likewise, for emission processes, the initial state is an excited state, which is in equilibrium with the solvent, while the final state is the ground state, but with the solvent still arranged for the excited state dipole, implying non-equilibrium. It is suggested to remember that in optical transitions the initial state is always considered to be in equilibrium with the solvent, while the final state is, by definition, in a non-equilibrium solvation configuration.

The goal of this section is to establish the general formalism used to compute the photophysical rates presented in Chapter 1 and employed throughout this work — absorption, fluorescence, phosphorescence, (reverse) intersystem crossing, and nonradiative decay. All these processes can be described within the same theoretical framework derived from time-dependent perturbation theory, in which the transition probability per unit time is proportional to the square of the coupling between the involved electronic states.

The following expressions are expanded from Ref. 63. We begin by considering the general expression used for computing rates and spectra:

$$k_S(E) = \frac{2\pi f}{\hbar\sqrt{2\pi\sigma^2}} \exp\left[-\frac{(E+\Delta E)^2}{2\sigma^2}\right], \tag{2.1}$$

where f is a coupling term that specifies the property being calculated, $\hbar$ is Planck's reduced constant, E is the photon energy (relevant only for absorption and emission processes), ΔE is the vertical transition energy, and σ is the width of the Gaussian convolution, which accounts for the overlap between vibrational wave functions and is approximately $k_B T$.

To include solvent effects, we consider the interaction between the system and its surrounding environment, modeled as a classical bath with a line-shape function given by [64]

$$k_b(E) = \frac{1}{\sqrt{4\pi\lambda_b k_B T}} \exp\left[-\frac{(E+\lambda_b)^2}{4\lambda_b k_B T}\right], \tag{2.2}$$

where λ_b is the solvent reorganization energy. The total rate can then be obtained through the convolution of both terms, yielding

$$k(E) = (k_s \cdot k_b)(E) = \frac{2\pi}{\hbar}\frac{f}{\sqrt{2\pi\sigma_T^2}} \exp\left[-\frac{(E+\Delta E+\lambda_b)^2}{2\sigma_T^2}\right], \tag{2.3}$$

where $\sigma_T^2 = 2\lambda_b k_B T + \sigma^2$ is the effective width that includes solvent and thermal contributions.

In practice, these quantities must be evaluated over an ensemble of molecular conformations. For flexible organic molecules — the main class of systems considered here — the geometries of the ground and excited states can differ substantially, affecting the corresponding transition energies. In such cases, the traditional Franck–Condon approximation, which assumes the transition probability to be proportional to the squared overlap between vibrational wave functions [65, 66], becomes insufficient. To overcome this limitation, we employ the nuclear ensemble method, in which the molecule's normal-mode frequencies obtained from an optimized geometry define a multidimensional distribution of configurations. The molecule is approximated as a coupled harmonic oscillator. Mathematically, that can be treated as a set of independent harmonic oscillators when the molecule is described in terms of its normal modes. The ensemble of geometries is sampled from the Wigner distribution:

$$\rho(\vec{r},T) = \prod_{i=1}^{3N-6} \sqrt{\frac{m\omega_i}{\pi\hbar}\tanh\left(\frac{\hbar\omega_i}{2k_B T}\right)} \exp\left[-\frac{\mu_i\omega_i}{\hbar} r_i^2 \tanh\left(\frac{\hbar\omega_i}{2k_B T}\right)\right], \tag{2.4}$$

where $\vec{r}$ represents the normal coordinates, T the temperature, k_B the Boltzmann constant, and μ_i and ω_i are the reduced mass and normal-mode frequency of the i-th mode, respectively. The derivation of this distribution is presented in Chapter 8. Thus, we add the rates for each geometrical conformation, indexed by j, such that we arrive at

$$k(E) = (k_s \cdot k_b)(E) = \frac{2\pi}{\hbar}\frac{1}{N}\sum_{j=1}^{N}\frac{f_j}{\sqrt{2\pi\sigma_T^2}} \exp\left[-\frac{(E+\Delta E_j+\lambda_{bj})^2}{2\sigma_T^2}\right], \tag{2.5}$$

Absorption spectra

The absorption cross section is obtained as a function of photon energy E by making

$$f_j = \frac{e^2\hbar^2}{4nmc\varepsilon_0} o_j \tag{2.6}$$

where n is the refractive index of the medium, c is the speed of light, e is the electron charge, ε_0 is the vacuum's permittivity and o_j is the oscillator strength for the electronic transition of the j-th geometrical conformation.

Emission spectra

For emission processes, the coupling becomes,

$$f_j = \frac{n^2e^2}{4\pi^2mc^3\varepsilon_0} \Delta E_j^2 o_j \tag{2.7}$$

in which ΔE_j^2 is the vertical transition energy of the j-th molecular conformation. In the case of phosphorescence, the oscillator strengths require second order perturbation theory that will not be further explored here, but it can be found in ref. 67. The total emission rate can be obtained by

$$k_{emi} = \frac{1}{\hbar} \int_0^\infty k(E) dE. \tag{2.8}$$

Intersystem crossing and reverse intersystem crossing

Using the general expression shown in 2.3, we can calculate the intersystem crossing and reverse intersystem crossing rates by considering $E = 0$ — no photon has a part in the transition — and considering the coupling f_j to be the square of the spin-orbit coupling between the relevant states involved in the transition transition of the j-th molecular conformation,

$$f_j = H_{SO,j}^2 \tag{2.9}$$

2.1.1 Solvent corrected expression

Let us further detail how we can extrapolate the ensemble calculated to a specific solvent to another without having to repeat all the calculations for the new solvent. We start by looking at the energy term in expression 2.3,

$$\Delta E_j + \lambda_{bj} = (E_{fj}^{eq} - E_{ij}^{eq}) + (E_{fj}^{neq} - E_{fj}^{eq}) = E_{fj}^{neq} - E_{ij}^{eq} \tag{2.10}$$

in which j indexes the geometrical conformations and considering the solvent reorganization energy to be the energetic penalty associated with the solvent's inability to instantaneously adjust its polarization to the new electronic configuration of the solute upon transition, thus $\lambda_{bj} = E_{fj}^{neq} - E_{fj}^{eq}$. We will not be using the j from now on, but we shall keep in mind that the expressions apply to each conformation within the ensemble. By looking at the right side of equation 2.10 and eliminating the index we have

$$\begin{aligned} E_f^{neq} - E_i^{eq} &= (E_f^0 - \lambda_f^{neq}) - (E_i^0 - \lambda_i^{eq}) \quad (2.11) \\ &= (E_f^0 - E_i^0) + \lambda_i^{eq} - \lambda_f^{neq} \quad (2.12) \\ &= \Delta E_{fi}^0 + \lambda_i^{eq} - \lambda_f^{neq} \quad (2.13) \end{aligned}$$

in which ΔE_{fi}^0 is the difference between the zeroth-order energies of the final and initial states of the transition, i.e., the energy that would be considering in the spectrum without the solvent. The term λ_i^{eq} corresponds to the first order correction to the energy of the initial state i, considering that the solvation occurs in equilibrium, while λ_f^{neq} is the first order correction to the energy of the final state f considering a non-equilibrium solvation.

The point of this formulation is to be able to use a single ensemble, calculate their transition energies for a solvent, namely solvent 1, and extrapolate same energies for a different solvent without recalculating those for the entire ensemble. The work performed in ref [63] shows that the energy corrections for the different solvents are proportional to each other, provide the two solvents have known refractive indexes and dielectric constants. Such relation of proportionality is given by

$$\lambda_{S_1}^{neq(2)} = \frac{\alpha_{opt}^{(2)}}{\alpha_{opt}^{(1)}} \lambda_{S_1}^{neq(1)}, \tag{2.14}$$

where the final state is the first singlet state and the $(m) = 1,2$ refer to the solvents. The proportionality coefficients are

$$\alpha_{opt} = \frac{n^2 - 1}{n^2 + 1} \tag{2.15}$$

and

$$\alpha_{st} = \frac{\varepsilon - 1}{\varepsilon + 1} \tag{2.16}$$

in which n and ε are the refraction index and the dielectric constant for the solvents in question, respectively. The indexes *st* and *opt* refer to static and optical, respectively.

Dielectric constant: it quantifies how strongly a material responds to an applied (static or low-frequency) electric field. It is experimentally defined as the ratio between the capacitance of a parallel-plate capacitor filled with a given material, C, and the same capacitor in vacuum, C_0, thus $\varepsilon = C/C_0$. In the context of this work, ε appears as the indicator of how polarizable the medium is. A higher ε corresponds to a more effective screening of charge separation and stabilizes charge-transfer (CT) states, typically leading to red-shifted emission — the phenomenon known as solvatochromism. Measurements of ε are frequency-dependent, so that $\varepsilon(\omega)$ is generally complex, $\varepsilon(\omega) = \varepsilon'(\omega) + i\,\varepsilon''(\omega)$). The static (low-frequency) dielectric constant $\varepsilon(0)$ includes both orientational and electronic polarization, whereas the high-frequency (optical) component, $\varepsilon_\infty \approx n^2$, represents the purely electronic response. This distinction separates the slow (dipolar) and fast (electronic) polarization regimesa categorization revisited later when discussing solvent susceptibility.

Refractive index: refraction is commonly described as the change in velocity (and consequently direction) of a wave when it enters a different medium. As elegantly shown in Feynmans lecture “The Origin of the Refractive Index”, the apparent slowing of light arises from coherent re-emission and interference, giving rise to the relation $n = c/v$ and ultimately to Snells Law. For an electromagnetic plane wave, $\vec{E}(t) = \vec{E}_0\, e^{i(\vec{k}\cdot\vec{r}-\omega t)}$, we have:

$$\nabla^2 \vec{D} = \mu\varepsilon \frac{\partial^2 \vec{D}}{\partial t^2} \quad \Rightarrow \quad k^2 = \mu\varepsilon \frac{\omega^2}{c^2}. \tag{2.17}$$

Since the phase velocity is $v = \omega/k$, the refractive index can be written as $n = c/v = ck/\omega$, which gives

$$n^2 = \mu\varepsilon. \tag{2.18}$$

For non-magnetic materials ($\mu \approx 1$),

$$n^2 \approx \varepsilon_\infty. \tag{2.19}$$

Here, we define the solvent susceptibility χ_i of a molecule's i-th electronic state as the ratio of the first order non-equilibrium correction in solvent 1, $\lambda_i^{neq(1)}$, and the corresponding optical proportionally coefficient for the same solvent $\alpha_{opt}^{(1)}$, i.e.,

$$\chi_i \equiv \frac{\lambda_i^{neq(1)}}{\alpha_{opt}^{(1)}} \tag{2.20}$$

That allows equation 2.14 to be reduced to

$$\lambda_{S_1}^{neq(2)} = \alpha_{opt}^{(2)} \chi_{s_1} \tag{2.21}$$

For the initial state, namely i, we have

$$\lambda_i^{eq(2)} = \frac{\alpha_{st}^{(2)}}{\alpha_{st}^{(1)}} \lambda_i^{eq(1)}. \tag{2.22}$$

The terms λ^{eq} and λ^{neq} are solvent corrections that are related to the solvent's reorganization energy and they are calculated for each state by Q-chem[68]. The equilibrium and non-equilibrium corrections are connect by

$$\lambda^{eq(1)} = \frac{\alpha_{st}^{(1)}}{\alpha_{opt}^{(1)}} \lambda^{neq(1)} \Rightarrow \lambda^{eq(1)} = \alpha_{st}^{(1)} \chi, \tag{2.23}$$

such that equation 2.22 becomes

$$\lambda_i^{eq(2)} = \frac{\alpha_{st}^{(2)}}{\alpha_{st}^{(1)}} \alpha_{st}^{(1)} \chi_i = \alpha_{st}^{(2)} \chi_i. \tag{2.24}$$

The scaling relationship was found by the authors by running these calculations for several molecules and solvents.

These relations can be inserted into equation 2.13 to yield

$$E_f^{neq} - E_i^{eq} = \Delta E_{fi}^0 + \alpha_{st}^{(2)} \chi_i - \alpha_{opt}^{(2)} \chi_f \tag{2.25}$$

which is also a general expression in the sense that it does not refer to a specific transition process. It is important to distinguish this solvent susceptibility from the conventional electromagnetic susceptibilities.

Susceptibility: The electric susceptibility, χ_e, is dimensionless and describes how much a material polarizes in response to an electric field in the form of $\vec{P} = \varepsilon_0 \chi_e \vec{E}$, with $\vec{P}$ being the polarization and $\vec{E}$ being the electric field. The magnetic susceptibility, χ_m, is also dimensionless and defines how much magnetization a material develops in response to an applied magnetic field through $\vec{M} = \chi_m \vec{H}$ and is also dimensionless. Both χ_e and χ_m are linear-response coefficients that characterize how the macroscopic fields $\vec{D}$ and $\vec{B}$ relate to $\vec{E}$ and $\vec{H}$, respectively:

$$\vec{D} = \varepsilon_0 (1 + \chi_e) \vec{E}, \qquad \vec{B} = \mu_0 (1 + \chi_m) \vec{H}. \tag{2.26}$$

Their microscopic origins are different: χ_e arises from charge displacement (electronic and orientational polarization), while χ_m arises from spin alignment or magnetic-moment reorientation.

In this work, the quantity referred to as solvent susceptibility (χ_f, or simply χ when the state index is omitted) is a state-specific energy term that measures how strongly the electronic component of the solvent stabilizes a given excited state. It has units of energy, not a dimensionless response like the electric or magnetic susceptibilities used in electromagnetism.

Physically, χ_f represents how much the fast electronic polarization of the surrounding medium stabilizes a given electronic state. As the name suggests, one can think of susceptibility as the physical quantity that tells you how sensitive a molecule is to a change in environment, when it comes fluorescence energy. That sensitivity is intimately linked to the character of the excited state, allowing for it to also be a character indicator.

The solvent susceptibility χ_f used in this thesis is therefore a state-specific energetic quantity, not a linear-response coefficient in the electromagnetic sense. It converts the dimensionless optical coupling factor α_{opt} into an actual stabilization energy, thereby linking the dielectric environment to the electronic energy of the molecule. To avoid confusion for readers from magnetic resonance or electromagnetism, it should be interpreted explicitly as an energetic solvent-response parameter rather than a susceptibility in the traditional field-theory sense.

Absorption processes

In the case of absorption processes, the initial state is S_0 whereas the final state can be any singlet state, hence there is no first-order correction to the initial state — first order corrections only exist in excited states, thus $\chi_{s_0} \to 0$. However, for the final state, we have the first order perturbative correction term (λ^{neq}), which specifies 2.25 to

$$E_f^{neq} - E_{s_0}^{eq} = \Delta E_{fs_0}^0 - \alpha_{opt}^{(2)} \chi_f, \tag{2.27}$$

which implies that the corrected energy for absorption processes in a solvent will be lower than that of in the vacuum. It is worth noting that if the solvents are the same, then expression 2.27 becomes the regular perturbative correction for absorption energies in which the first order perturbative correction is added to PCM vertical excitation.

Emission processes

Now we turn our attention to emission processes. In such cases, the final state will always be the ground state, whereas the initial one can be any excited state of interest, meaning that $\chi_f = 0$. This implies that $\Delta E_{fi}^0 < 0$, due to the fact that the final state's energy will always be lower in emissive processes. We will take the module of ΔE_{fi}^0 and adjust the signs so we can treat the $E_f^{neq} - E_i^{eq}$ as a positive, yielding

$$E_f^{neq} - E_i^{eq} = |\Delta E_{fi}^0| - \alpha_{st}^{(2)} \chi_i, \tag{2.28}$$

ISC and rISC processes

For the case of intersystem crossing we have the conversion between an singlet (triplet) excited state to a triplet (singlet) excited state (rISC). Although both initial and final states are excited, they are of opposite spin. Nevertheless, both states with have their corresponding corrections, which brings the energy difference to

$$E_f^{neq} - E_i^{eq} = \Delta E_{fi}^0 + \alpha_{st}^{(2)} \chi_i - \alpha_{opt}^{(2)} \chi_f. \tag{2.29}$$

Solvent reorganization energy

The developments presented thus far have combined the solvent reorganization energy to the energy difference, but we still need to explicitly obtain these reorganization energies since they are used in the broadening factor σ_T. The reorganization energy is given by

$$\lambda_b = E_f^{neq} - E_f^{eq}. \tag{2.30}$$

When the final state is an excited state (absorption and (r)ISC), such energy difference is reduced to the difference between first order corrections,

$$\lambda_b = \lambda_f^{eq} - \lambda_f^{neq} \tag{2.31}$$

$$= \chi_f(\alpha_{st}^{(2)} - \alpha_{opt}^{(2)}) \tag{2.32}$$

However, when the final state is the ground state — emission processes —, the energy of said state in the PCM approach is given by

$$E_{S_0} = \langle 0|\hat{H}_{vac}|0\rangle + \frac{1}{2}\langle 0|\hat{R}_0|0\rangle \tag{2.33}$$

where $\hat{H}_{vac}$ is the vacuum Hamiltonian and $\hat{R}_0$ is the reaction-field potential that refers to the PCM correction to the ground state, which scales with α_{st}, thus being identified as $\lambda_{S_0}^{eq}$. Then, applying the scaling relation to write the solvent reorganization energy in terms of the equilibrium correction in equation 2.32, we have

$$\lambda_b^{emi} = \left(\frac{\alpha_{st}^{(2)}}{\alpha_{st}^{(1)}} - \frac{\alpha_{opt}^{(2)}}{\alpha_{st}^{(1)}}\right)\lambda_{S_0}^{eq}. \tag{2.34}$$

which is the value we are going to use when calculating the broadening factor. The expressions used in each situation are summarized in Table 2.1.

Process	Coupling (f)	Energy ($\Delta E + \lambda_b$)	Solvent reorganization energy (λ_b)
Absorption	$\frac{e^2\hbar^2}{4nmc\varepsilon_0}o$	$\Delta E_{fs_0}^0 - \alpha_{opt}^{(2)}\chi_f$	$\chi_f(\alpha_{st}^{(2)} - \alpha_{opt}^{(2)})$
Emission	$\frac{n^2e^2}{4\pi^2mc^3\varepsilon_0}\Delta E^2 o$	$\lvert\Delta E_{fi}^0\rvert - \alpha_{st}^{(2)}\chi_i$	$\left(\frac{\alpha_{st}^{(2)}}{\alpha_{st}^{(1)}} - \frac{\alpha_{opt}^{(2)}}{\alpha_{st}^{(1)}}\right)\lambda_{S_0}^{eq}$
r(ISC)	H_{SO}^2	$\Delta E_{fi}^0 + \alpha_{st}^{(2)}\chi_i - \alpha_{opt}^{(2)}\chi_f$	$\chi_f(\alpha_{st}^{(2)} - \alpha_{opt}^{(2)})$

Table 2.1: Processes and their respective couplings, energies and solvent reorganization energies in solvent environments.

2.2 Förster Resonance Energy Transfer

Excitons can be transferred in two known different processes, Dexter and Förster. The former operates through a short-range electron-exchange mechanism that relies on direct wavefunction overlap between donor and acceptor molecular orbitals. Consequently, it decays exponentially with distance and is only significant for distances typically shorter than 5 Å[69]. It also allows for both singlet-singlet and triplet-triplet transfers because it involves actual electron exchange rather than dipole coupling. The latter, on the other hand, is a long-range, nonradiative dipole–dipole coupling process where the excitation energy is transferred from a donor in its excited state to an acceptor in its ground state through resonance between their transition dipole moments. Because it depends on the overlap of donor emission and acceptor absorption spectra, FRET is efficient over distances of 10 to 100 Å, and requires minimal orbital overlap between the molecules.

Considering a donor-acceptor (D/A) pair, the transfer takes place in such way that the donor returns from its first excited state to its ground state. The acceptor, in turn, absorbs the excitation and goes from its ground state to its first excited state, as shown in figure 2.1's schematic representation.

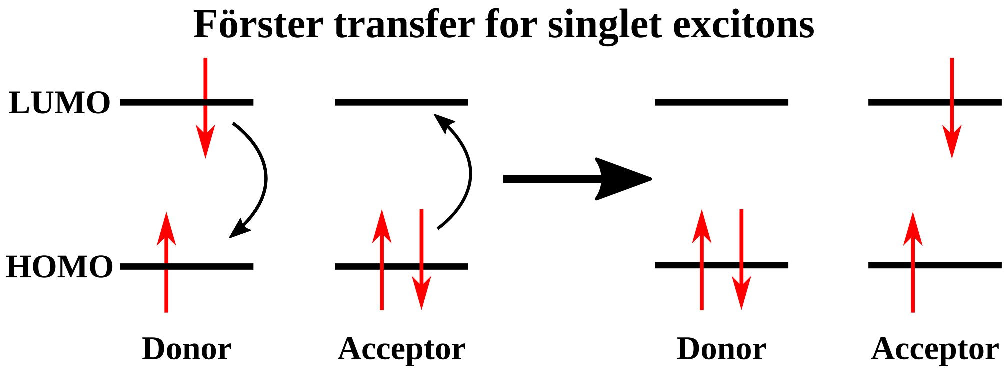

Figure 2.1: FRET mechanisms for singlet excitons.

By looking at the representation shown in figure 2.1, we can identify two states. First, to the left, in which the donor is excited (D^1) and the acceptor is not (A) which we can name $|D^1A\rangle$. Second, to the right, shows the donor back to its ground state (D) and the acceptor is now in its first excited state (A^1), namely $|DA^1\rangle$. If said state is stable enough in the system where it's located, this superposition state is the characterization of the exciton in terms of quantum states[70].

The rate for which FRET takes place is given by [71]

$$k_F(r) = \frac{9c^4\kappa^2}{8\pi r^6}\int_0^\infty \frac{d\omega}{\omega^4}\phi_D(\omega)\sigma_A(\omega), \tag{2.35}$$

where c is the speed of light, r is the intermolecular distance (also know as the average hopping distance), $\phi_D(\omega)$ is the donor's differential emission rate and $\sigma_A(\omega)$ is the donor's absorption cross section. As said before, the transfer rate requires the existence of energy overlap between $\phi_D(\omega)$ and $\sigma_A(\omega)$, otherwise the excitation cannot hop from D to A. The orientation factor, κ, describes the relative orientation between the transition dipole moment of the donor ($\vec{\mu_D}$) and that of the acceptor ($\vec{\mu_A}$), as well as the their orientation with respect to the intermolecular vector $\hat{r}$ connecting donor and acceptor. Mathematically,

$$\kappa = \vec{\mu_D} \cdot \vec{\mu_A} - 3(\vec{\mu_D} \cdot \hat{r})(\vec{\mu_A} \cdot \hat{r}) \tag{2.36}$$

The Förster rate depends on (κ^2), which can range between 0 and 4. If we assume isotropic and independent orientation distributions over the ensemble, we get $\kappa^2 = 2/3$[72], which is what we typically use when computing Förster rates.

The recombination (or emission) rate may be estimated by

$$k_{emi} = \frac{1}{\tau_{emi}} = \int_0^\infty \phi_D(\omega) d\omega \tag{2.37}$$

where τ_{emi} is the exciton's radiative lifetime.

The distance for which spontaneous recombination and hopping by FRET are equally probable is known as the Förster radius. An expression for it can be obtained by making $k_{emi} = k_F$,

$$R_F^6 = \frac{9c^4\kappa^2\tau_{emi}}{8\pi} \int_0^\infty \frac{d\omega}{\omega^4} \phi_D(\omega)\sigma_A(\omega). \tag{2.38}$$

We can also represent k_F in terms of the Förster radius,

$$k_F = \frac{1}{\tau_{emi}} \left(\frac{R_F}{\bar{r}} \right)^6 \tag{2.39}$$

Studies show that equation (2.39) overestimates the Förster rate for short distances, even if the definition of what a *short* distance means is unclear [73]. A correction for such problem takes the transition dipole moment μ into consideration to adjust the denominator in equation (2.39),

$$k_F = \frac{1}{\tau_{emi}} \left(\frac{R_F}{\gamma\mu + \bar{r}} \right)^6 \tag{2.40}$$

where $\gamma = 1.15\ e^{-1}$. Such correction defines an effective intermolecular distance [74, 75, 76].

2.3 Best Practices for Excited-State Rate Calculations

The accurate description of the excited-state processes discussed above requires particular care in the choice of the underlying electronic-structure methods. Density functional theory (DFT) was used for all electronic structure calculations in this work. While DFT provides a practical balance between accuracy and computational cost, its performance strongly depends on the exchange–correlation functional, the treatment of long-range interactions, and the chosen excited-state formalism. The following considerations summarize the best practices adopted in this work. Additionally, the development of the core expressions and background regarding DFT is done in Appendix 7.

2.3.1 Choice of exchange–correlation functional

Hybrid and range-separated hybrid functionals are generally preferred for excited-state calculations because they correct for the self-interaction errors that plague semilocal functionals and lead to underestimated excitation energies. Range-separated hybrids (RSHs), such as CAM-B3LYP or ωB97X and $LC - \omega PBE$ include a fraction of Hartree–Fock exchange that increases with interelectronic distance, improving the behavior of the exchange potential. This correct treatment of the long-range electron–hole interaction is essential for processes in which donor and acceptor orbitals are spatially separated.

2.3.2 Non-empirical tuning of the range-separation parameter.

The range-separation parameter ω in RSH functionals can be empirically fitted or non-empirically optimized. In this work, the latter approach is employed by enforcing the ionization potential theorem, which minimizes the deviation between the highest occupied and lowest unoccupied Kohn–Sham eigenvalues and the vertical ionization potential and the electronic affinity, respectively, within the associated limitations of DFT. This procedure ensures that the functional reproduces the correct asymptotic potential for each molecule, reducing delocalization errors and yielding excitation energies that are consistent with experimental optical gaps.

2.3.3 Tamm–Dancoff approximation (TDA):

Systematic underestimating results regarding the triplet excitation energies have been observed when TD-DFT is employed to perform such calculations. This problem appears to be more severe as the amount of exact orbital exchange in the functional increases. It is also well known that triplet instability problems can lead to inaccuracies in other molecular properties [77, 78, 79] that depend on the characterization of triplet excited states, as is the case for indirect nuclear spin-spin coupling constants[80]. That said, calculations involving excited states were performed using the Tamm-Dancoff approximation (TDA) [81], given it mitigates triplet instability issues[82], as well as provides accurate results in spectrum simulations[83].

2.3.4 Consistency between singlet and triplet manifolds:

When evaluating ISC and rISC rates, it is crucial that both singlet and triplet states are described at the same theoretical level and with the same functional, basis set, and solvent model. Inconsistencies between these descriptions can lead to artificial energy gaps or inaccurate spin–orbit coupling matrix elements, directly affecting rate predictions.

2.3.5 Vibrational and environmental effects:

It is preferred that all electronic-state quantities entering the rate expressions are averaged over nuclear geometries sampled from the ensemble distribution (Eq. 2.4), ensuring that the computed rates account for vibrational broadening and thermal fluctuations. Solvent effects are included within the linear-response and perturbative state-specific framework, using the same dielectric parameters employed in the susceptibility analysis that will be discussed in Chapter 4, thus guaranteeing methodological consistency across all photophysical processes. However, even if the calculation framework is as close to perfect as possible, it will always be highly dependent and sensitive to the quality of the optimized geometry employed in the ensemble generation.

Overall, this combination of tuned range-separated hybrid functionals, TD(A)-based excited-state calculations, and ensemble-averaged electronic properties provides a balanced and transferable protocol for describing radiative and nonradiative transitions in molecular emitters and donor–acceptor systems.

CHAPTER 3

AFTERGLOW IN HOST-GUEST SYSTEMS

3.1 Overview

As introduced in Chapter 1, the afterglow phenomenon in organic systems can emerge from different triplet harvesting pathways. Among these, TTS energy transfer offers a route to delayed emission without the involvement of heavy atoms or strong spin-orbit coupling for competitive rISC rates. The experimental observations on NPB/DCJTB blends in a PMMA matrix made by ref. 52 showed long-lived luminescence following optical excitation of NPB, with the delayed component originating from DCJTB fluorescence that did not present itself in pure DCJTB samples. This behavior suggested that triplet excitons formed in NPB are able to migrate and transfer to DCJTB through TTS Förster coupling. In this chapter, we build directly upon those findings, providing a theoretical description of the relevant photophysical rates and morphological details of the NPB/DCJTB system to identify the microscopic origin of the observed afterglow and to quantify the relative importance of competing radiative and nonradiative processes.

3.2 Modeling and methodology

3.2.1 Electronic structure

All electronic structure-related calculations contemplated in this work were performed using QChem 5.0[68] and Gaussian 16 [84]. These softwares employ DFT and its time-dependent extension.

Due to its long-range correction, the ωB97XD functional was employed with the $6-31G(d,p)$ basis set. All the calculations explained in this section were performed for NPB and DCJTB due to PMMA's lack of interaction with both dopant molecules.

For each molecule of interest, the functional's range separation parameter was tuned non-empirically, according to the protocol presented in ref. 85. Once tuning was achieved, optimized geometries and their respective normal mode frequencies were obtained for both compounds in their ground (S_0), first singlet (S_1) and triplet (T_1) excited states. Additionally, these calculations yield other important quantities, such as the vertical transition energies and the transition dipole moment, necessary for other steps. It is worth mentioning that although different solvent environments are being investigated, the polarization continuum model (PCM) and any other solvent related method were not employed for geometry optimization or the obtention of normal mode frequencies. This is due to the fact that geometries are not significantly altered when these methods are employed[86].

3.2.2 Spectra Simulation

Using the nuclear ensemble method via electronic structure results as inputs, we were able to simulate absorption, fluorescence and phosphorescence spectra for S_0, S_1 and T_1 states respectively. Ensembles comprised of 500 conformations were sampled from the Wigner distribution (equation 2.4) at $T = 300$ K. PCM along with a perturbative state specific and perturbative linear response solvation corrections were used in all excited state calculations to provide more accurate solvent corrections to the energies of electronic states[86, 87, 63, 88, 89, 90, 91].

From each ensemble, the solvent extrapolation method, detailed in Chapter 2, was employed and ISC, rISC, fluorescence, phosphorescence and nonradiative decay (for triplet excitons) rates were calculated in different mediums. Additionally, the Förster radius for singlet-singlet and triplet to singlet transfers were calculated, allowing us to determine the possible transfer pathways in the system. All aforementioned values are displayed further ahead in this chapter. These rates were used as parameters in a KMC simulation implemented to better understand how each phenomenon can impact the energy transfer processes in our system.

3.2.3 Medium polarity

Due do the aforementioned self-polarizing effect of DCJTB, we can use our solvent model to better characterize the system in different DCJTB concentrations. Solvent susceptibility and E_{vac} can be determined by fitting experimental emission peaks measured in different solvents with Equation 2.28. Once that is done, experimental emission peaks measured in films of varying dopant concentration can be used to infer the ε values of each film. Finally, the dielectric constant values obtained this way can be fitted as a function of dopant concentration providing ε values for any desired concentration. Results of this procedure are shown in Table 3.4.

3.2.4 Kinetic Monte Carlo

Morphology

In order to perform KMC simulations, the system's morphology needs to be obtained in terms of the number of each molecule and how they are spread across a lattice. To that end, we took the experimental concentrations of each dopant (NPB and DCJTB) within a PMMA matrix. The experimental data kept the concentration of NPB, ρ_{NPB}, constant at 2.0 wt% while varying the acceptor's concentration, ρ_{DCJTB}, between 0.0 wt% and 2.0 wt%. Assuming the increase of acceptor concentration meant a reduction of PMMA concentration while not altering donor concentration, we were able to calculate the number of molecules in the system for each acceptor concentration using

$$N_i = \frac{\rho_i N_A M_{total}}{M_i}, \tag{3.1}$$

where N_i is the number of each molecule, N_A is Avogadro's number, ρ_i is the concentration in wt%, M_{total} is the sample's total mass and M_i is its molecular weight. Thus, the total number of molecules is,

$$N_{total} = \sum N_i = N_A M_{total} \sum \frac{\rho_i}{M_i} \tag{3.2}$$

The probability of finding a certain molecule is simply given by the ratio of the number of said molecule and the sum of all molecules,

$$P_i = \frac{\rho i}{M_i \sum \frac{\rho_i}{M_i}} \tag{3.3}$$

Our KMC model consists of a cubic lattice of 50x50x50 sites that only accounts for dopants in its sites, with an average intermolecular distance that varies according to concentration due to the different number of acceptor molecules. To obtain the intermolecular distance between donor and acceptor molecules we calculate the probability of finding one of the dopants within the PMMA matrix as

$$P_{dop} = \frac{P_{NPB} + P_{DCJTB}}{P_{NPB} + P_{DCJTB} + P_{PMMA}}, \tag{3.4}$$

which can be interpreted as the percentage of dopants in the system. With that in mind, the intermolecular distance between dopants, d_{avg}, was calculated as

$$d_{avg} = d_0 \sqrt[3]{\frac{1}{P_{dopants}}} \tag{3.5}$$

in which d_0 is a estimated intermolecular distance between all molecules, including the PMMA matrix. Considering $d_0 = 5$ Å, we were able to calculate the average intermolecular distance and the relative percentage of materials present in the lattice's sites. The parameters described above are shown in Table 3.1. For all cases displayed, the probability of having NPB in the system is of 0.35%, due to the fixed concentration of 2.0 wt%.

ρ_{NPB}	ρ_{DCJTB}	ρ_{PMMA}	P_{NPB} (%)	P_{DCJTB} (%)	P_{PMMA} (%)	P_{dop} (%)	d_{avg} (Å)	$DCJTB_{sites}$ (%)
2.0	0.0	98.0	0.35	0.00	99.65	0.346	33.05	0.0
	0.2	97.8		0.05	99.61	0.394	31.65	12.1
	0.5	97.5		0.12	99.53	0.467	29.92	25.5
	0.8	97.2		0.19	99.46	0.539	28.51	35.4
	1.1	96.9		0.26	99.39	0.612	27.33	43.0
	1.4	96.6		0.34	99.31	0.686	26.32	49.0
	1.7	96.3		0.41	99.24	0.759	25.44	53.8
	2.0	96.0		0.48	99.17	0.833	24.66	58.7

Table 3.1: Donor concentration (ρ_{NPB}), acceptor concentration (ρ_{DCJTB}) and PMMA matrix concentration (ρ_{PMMA}) in molecular weight percentage (wt%). Contribution to sample composition by NPB (P_{NPB}), DCJTB (P_{DCJTB}) and PMMA (P_{PMMA}), according to equation 3.3. Probability of a dopant to be found within the sample (P_{dop}), average intermolecular distance between dopants (d_{avg}) and the percentage of sites containing acceptor molecules ($DCJTB_{sites}$) are shown in the last three columns, respectively.

Exciton dynamics

As the name Monte Carlo suggests, the occurrence of events in our model is probabilistic. We have the rates with which each individual process occurs. With that, when can define the probability of any given process, namely i, as

$$P_i = \frac{k_i}{\sum_j k_j}. \tag{3.6}$$

The probabilities are then ordered and added to get 1.0 (100%). A random number between 0 and 1 is then draw. The interval in which this number falls on determines the process to take place. To illustrate this, consider that $P_{fluor} = 0.3$, $P_{ISC} = 0.3$, $P_{FRET} = 0.4$, such that by normalizing the probabilities and considering a random number q, we get that fluorescence occurs when $0.0 \leq q < 0.3$, ISC happens when $0.3 \leq q < 0.6$ and FRET happens when $0.6 \leq q < 1.0$.

To reproduce experimental conditions, singlet excitons are generated uniquely in NPB sites. They are then allowed to move by Förster transfer. Since we simulate optically generated excitons, triplet excitons are only created as a product of ISC. ISC rates are taken as the sum of ISC rates from S_1 to the first five triplet states, but given usually high internal conversion rates, we consider these transfers to effectively happen between S_1 and T_1. As such, once the singlet exciton is generated on NPB, it undergoes one of three possible processes: singlet-to-singlet transfer between molecules; ISC to the T_1 state; or fluorescence. The probability of these processes are given by:

$$P_{ISC} = \frac{k_{ISC}}{k_{ISC} + k_{Fluor} + k_{FRET_{NPB-NPB}} + k_{FRET_{NPB-DCJTB}}} \tag{3.7}$$

$$P_{Fluor} = \frac{k_{Fluor}}{k_{ISC} + k_{Fluor} + k_{FRET_{NPB-NPB}} + k_{FRET_{NPB-DCJTB}}} \tag{3.8}$$

$$P_{FRET_{NPB-NPB}} = \frac{k_{FRET_{NPB-NPB}}}{k_{ISC} + k_{Fluor} + k_{FRET_{NPB-NPB}} + k_{FRET_{NPB-DCJTB}}} \tag{3.9}$$

$$P_{FRET_{NPB-DCJTB}} = \frac{k_{FRET_{NPB-DCJTB}}}{k_{ISC} + k_{Fluor} + k_{FRET_{NPB-NPB}} + k_{FRET_{NPB-DCJTB}}} \tag{3.10}$$

In the case of ISC, the resulting triplet exciton can either phosphoresce or undergo TTS transfer to DCJTB. Once transferred, the exciton is now in a singlet state, subject to the same possible processes as when it was first generated. For this system, the calculated average intermolecular distances prevent orbital overlap, which means that triplet excitons do not undergo energy transfer via the Dexter mechanism[92, 69]. The process that takes place is selected by a weighted random selection algorithm that is repeated until recombination occurs. Each simulation is run with 10^6 excitons. Figure 3.1 is a flowchart illustrating the possible pathways for a singlet exciton generated on NPB.

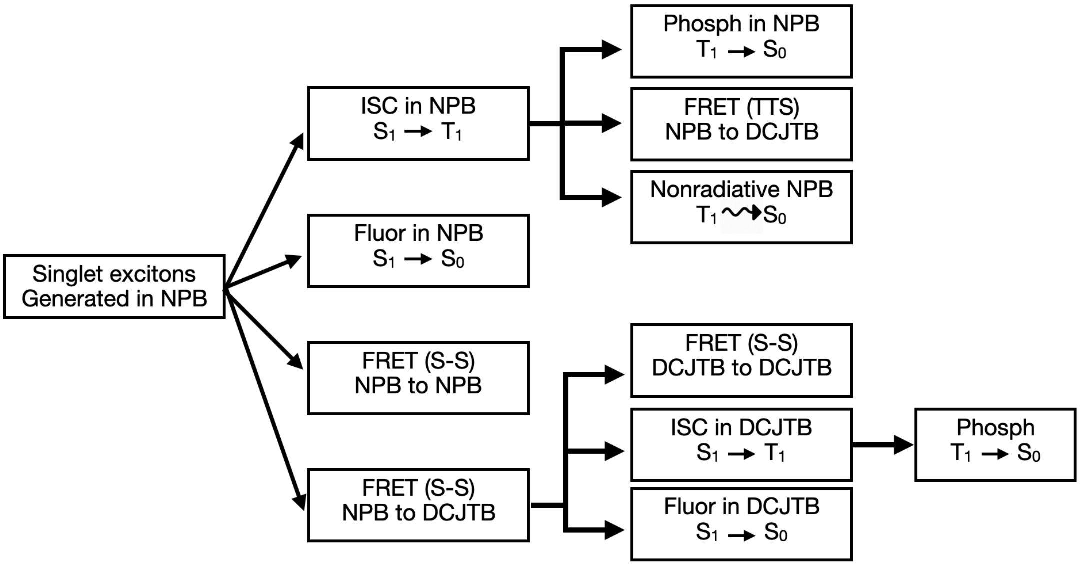

Figure 3.1: Flowchart of the possible pathways for a singlet exciton generated on NPB.

3.3 Results

3.3.1 Electronic structure and spectra simulation

Before we treat the phenomenon of energy transfer, we focused on the optical characterization of each individual molecule. Experimental and simulated absorption, fluorescence, and phosphorescence peaks are shown in Table 3.2 for both NPB and DCJTB in different media. As shown in the table, there is excellent agreement between simulated and experimental maximum wavelengths for NPB's absorption, with a corresponding energy variation lower than 0.1 eV. Although it does not display the same level of agreement, its phosphorescence spectral is still in reasonable agreement, the maximum energy difference is under 0.25 eV.

Molecule	Transition	Medium	ε	n	F_{max}^{calc} (eV)	F_{max}^{exp} (eV)
NPB	$S_0 \rightarrow S_1$	Thin film	3.000	1.785	3.69	3.61[93, 94, 95]
	$S_1 \rightarrow S_0$	$[PMMA:NPB]_{sc}$	3.000	1.485	2.82	2.92[96, 52]
		$[TCTA:NPB]_{sc}$	3.035	1.718	2.81	2.82[96]
		$[TCTA:NPB]_{evap}$	3.035	1.718	2.81	2.88[96]
	$T_1 \rightarrow S_0$	$[PMMA:NPB]_{sc}$	3.000	1.485	2.05	2.30[96],2.25[52]
		$[TCTA:NPB]_{sc}$	3.035	1.718	2.12	2.30[96]
		$[TCTA:NPB]_{evap}$	3.035	1.718	2.12	2.30[96]
DCJTB	$S_1 \rightarrow S_0$	C_6H_6	2.270	1.490	2.23	2.20[97, 98]
		$CHCl_3$	4.810	1.446	2.17	2.08[98]
		C_2H_5OH	24.300	1.361	2.04	1.92[98]
		$DMSO,(CH_3)_2:SO$	46.700	1.386	2.02	2.02[52],1.87[97]
	$T_1 \rightarrow S_0$	$PMMA$	3.000	1.485	1.59	-

Table 3.2: Calculated (F_{max}^{calc}) and experimental (F_{max}^{exp}) photoluminescence peaks for NPB and DCJTB in different media. Media's dielectric constants (ε) and refractive indices (n) are displayed.

In the case of DCJTB extra care is necessary when comparing experimental and simulation re-

Molecule	Transition	Concentration (wt%)	ε^{calc}	F_{max}^{exp} (nm)	F_{max}^{calc} (nm)
DCJTB	$S_1 \rightarrow S_0$	0.8	4.16	606	566
		1.5	5.64	613	577
		3.0	8.84	635	592

Table 3.3: Experimental (F_{max}^{exp}) and simulated (F_{max}^{calc}) fluorescence peaks for AlQ_3 thin films doped with DCJTB in different concentrations. Estimated dielectric constants (ε^{calc}) are shown. Experimental data taken from Ref. 97

sults. This is so because films doped with DCJTB as emitter have been shown to exhibit a concentration-dependent red-shift due to self-polarization [97, 98], similarly to what happens in solution when solvent polarity increases. Thus, it is necessary to map the different DCJTB concentrations into corresponding dielectric constants for use in calculations. To do that, we take into account the results from Ref. 97, which reports on AlQ_3 films doped with three concentrations of DCJTB: 0.8 wt%, 1.5 wt% and 3.0 wt%. We then use those values for our simulated spectra. Results are shown in Table 3.3. The interpolation of dielectric constants and their use in simulating the corresponding spectra reproduce the experimental peaks within reasonable agreement, with a peak to peak difference no higher than 0.15 eV.

Now that we have shown that our tools have displayed satisfactory results, we can employ the aforementioned procedure to determine the dielectric constants of the host-guest system in question with different DCJTB concentrations. Results of this are shown in Table 3.4. Those values for dielectric constant will be used from now on to compute the spectra for both molecules and its associated information.

NPB Conc. (wt%)	DCJTB Conc. (wt%)	ε	n
2.0	0.0	2.45	1.485
	0.2	2.88	
	0.5	3.52	
	0.8	4.16	
	1.1	4.80	
	1.4	5.44	
	1.7	6.08	
	2.0	6.72	

Table 3.4: Interpolated dielectric constants corresponding to different acceptor concentrations.

In Figure 3.2-a, the normalized fluorescence spectrum for pure NPB with dielectric constants corresponding to several DCJTB concentrations (Table 3.4) is shown. Notably, NPB's experimental fluorescence spectrum peaks at around 2.85 eV (435 nm)[52]. This closely aligns with the simulated spectrum, which peaks at 2.80 eV (442 nm) when no DCJTB is present ($\varepsilon = 2.45$). With increasing DCJTB concentration, the simulated spectrum undergoes a redshift and broadening. Turning to DCJTB, Figure 3.2-b showcases its fluorescence spectrum under varying concentrations. In spite of reasonable agreement, the experimental redshift is more intense than the predicted one. Our simulation shows a fluorescence peak at 2.12 eV (586 nm) for the highest concentration versus an experimental peak of 2.02 eV (615 nm)[52]. It can be seen thus, that our spectrum simulations capture most of the redshift in the fluorescence spectrum that results from changes in the medium's polarity. It is worth noting that higher spectral broadening is also associated with increased solvent reorganization energies. However, since spectrum simulations do not include non-radiative decay, which quenches higher wavelength emission more strongly, the resulting simulated fluorescence spectra become broader than their experimental counterparts.

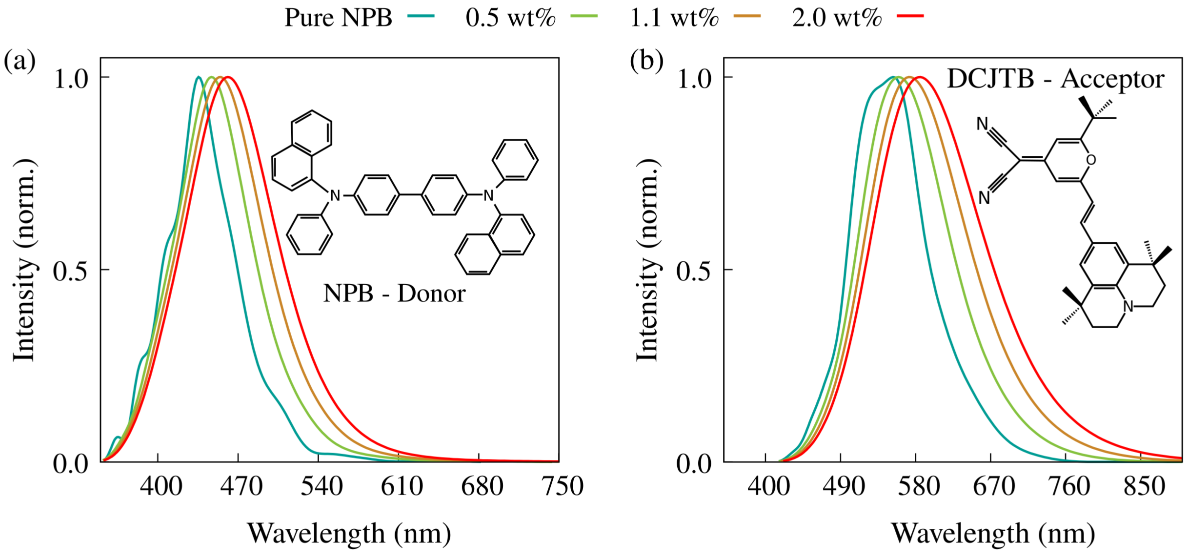

Figure 3.2: Simulated fluorescence spectra for both NPB (a) and DCJTB (b) molecules for different DCJTB concentrations (different dielectric constants).

Changes in medium polarity due to DCJTB concentration have broader implications beyond just altering the spectra. In Figure 3.3, we present an energy level diagram including the most relevant electronic transitions and their corresponding rates for NPB in the lowest (Figure 3.3-a) and highest (Figure 3.3-b) DCJTB concentrations ($\varepsilon = 2.45$ and $\varepsilon = 6.72$, respectively). Comparison between these two figures show a 0.16 eV redshift in the S_1 energy, which is consistent with a charge-transfer state.

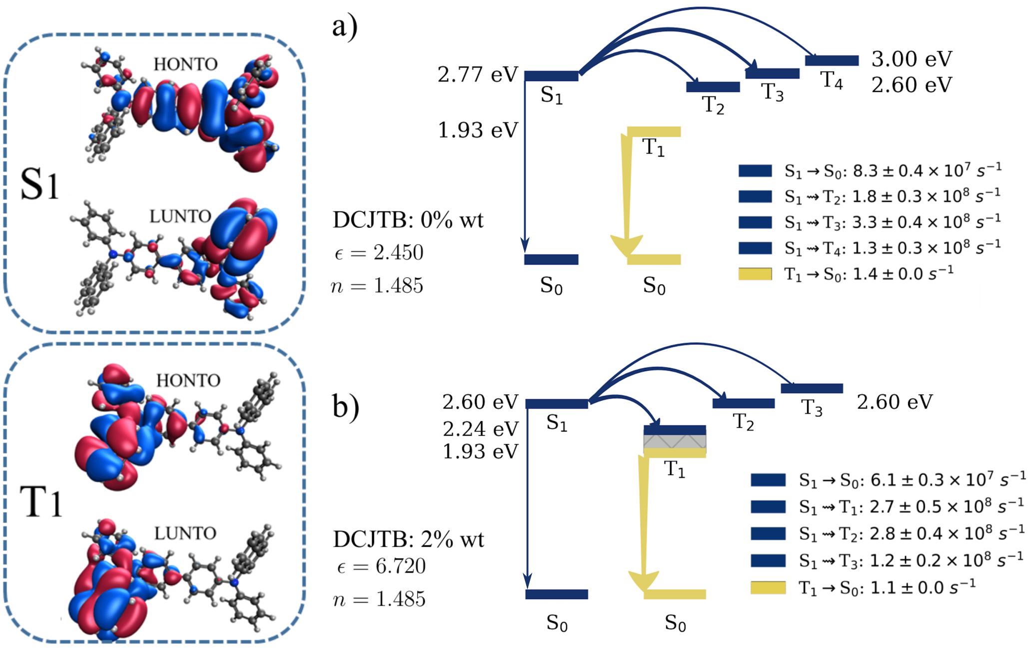

Figure 3.3: Natural transition orbitals (HONTO and LUNTO) for the S_1 and T_1 states along with energy level diagrams of NPB with (a) 0% DCJTB concentration ($\varepsilon = 2.45$) and (b) 2% concentration ($\varepsilon = 6.72$). Curved and straight arrows represent ISC and emission, respectively. The girth of the arrows are proportional to the rate value.

Natural transition orbitals (NTOs) for the S_1 state are also shown in Figure 3.3 and confirm the CT character of the first singlet state of NPB. The redshift of the S_1 state also affects the ISC processes. At low polarity, calculations show ISC to the second, third and fourth triplet states as the most relevant, due to lower energy gaps. It is expected that internal conversion from these states down to T_1 should follow, though. In the high polarity scenario, ISC to T_1 occurs at similar rate as ISC to the T_2 and T_3 states, due to availability of triplet states in the ensemble with energies closer to S_1. After ISC, relaxation in the triplet potential energy surface — represented by the gray area in the figure — ensues. It is worth mentioning that T_1 energies are unaffected by medium polarity. This is due to the localized character of the T_1 state as evidenced by the NTOs in Figure 3.3. Once in the T_1 state, calculations show phosphorescence as the main deactivation pathway, beating rISC and nonradiative decay (ISC to the ground state). In Figure 3.4, NPB's phosphorescence spectra are shown for three different DCJTB concentrations. Due to the localized character of the T_1 state, these spectra are not very sensitive to changes in medium polarity. Figure 3.4 also shows the existence of spectral overlap between NPB phosphorescence and DCJTB absorption spectra, indicating the possibility of TTS transfers. The equivalent level diagram for DCJTB in the same concentrations can be seen in Figure 3.5, showing that DCJTB does not present rISC either but rather efficient nonradiative decay pathway for triplets, indicated by the $T_1 \rightsquigarrow S_0$ transition.

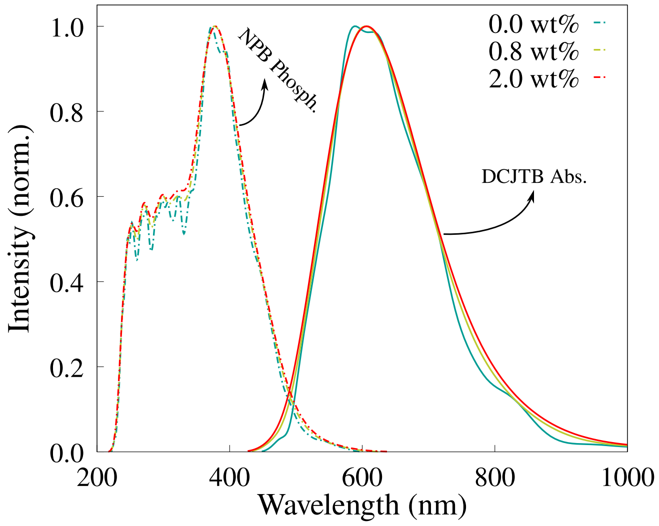

Figure 3.4: Phosphorescence spectra for NPB (dashed lines) computed with dielectric constants associated with three different concentrations of DCJTB, 0 wt%, 0.8 wt% and 2.0 wt%. The full lines display the DCJTB absorption spectra for the corresponding concentrations.

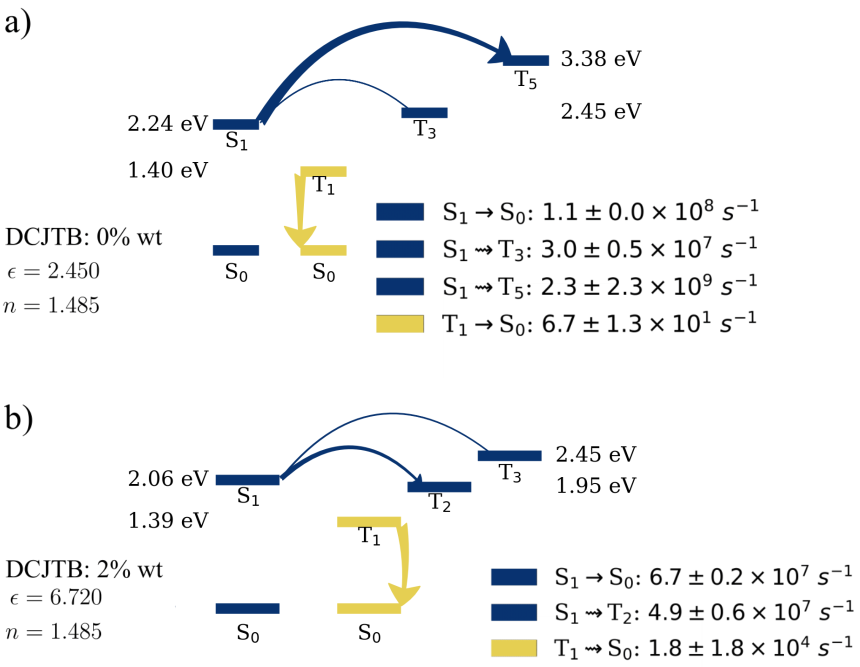

Figure 3.5: Energy level diagram for DCJTB with (a) 0 wt% DCJTB concentration ($\varepsilon = 2.450$) and (b) 2 wt% concentration ($\varepsilon = 6.720$). Here, energy levels are computed as ensemble averages.

Figure 3.6 shows how the change in the system's polarity resulting from the increasing DCJTB concentration alters different rates. In Figure 3.6-a, we present the fluorescence rates for both molecules across various concentrations. Notably, these rates follow similar trends for both molecules, decreasing with concentration while remaining within the same order of magnitude. This behavior is also observed in the phosphorescence rates, as depicted in Figure 3.6-b, despite the almost two orders of magnitude difference between each other.

Examining the intersystem crossing rates shown in Figure 3.6-c, we note that NPB exhibits rates ranging from 6.4×10^{8} s^{-1} to 6.6×10^{8} s^{-1}, while DCJTB's go from 3.3×10^{7} to 5.7×10^{7} s^{-1}, differing by one order of magnitude. The ISC rate is inherently linked to the spin-orbit coupling (SOC) of the molecule. Average coupling values were calculated for each DCJTB concentration and are depicted in figures 3.7-a and 3.7-b for both molecules. They range from 0.18 meV to 0.32 meV in NPB and from 0.05 meV to 0.09 meV in DCJTB. Furthermore, the ISC rate of NPB is also one order of magnitude larger than its fluorescence rate. This means that a singlet exciton is roughly ten times more likely to undergo ISC into a triplet state than to fluoresce. In the case of DCJTB, due to both rates being within the same order of magnitude, there is a 48 % chance of ISC taking place, according to calculations.

Figure 3.8-a depicts the Förster radii as a function of DCJTB concentration for the most relevant singlet-to-singlet and TTS exciton transfers. All curves related to singlet-singlet transfer exhibit a trend of slightly decreasing radius with increasing DCJTB presence, while the TTS related radius increases with DCJTB presence. Experimental estimates of the Förster radius for singlet-singlet transfer from NPB to DCJTB put it at 36.0 ± 10 Å[52]. Moreover, our simulations yielded a range of 51.3 Å to 49.4 Å, with an average of 50.1 ± 1.7 Å. Regarding the TTS Förster radius, the same experimental study reported it at 25.0 ± 10 Å, whereas our results placed it between 30.5 Å and 33.0 Å, averaging 32.1 ± 2.5 Å.

Figure 3.8-b displays the Förster rate between first neighbors for each transfer as a function of DCJTB concentration. A decrease in Förster radius translates into less effective transfers only if the effective interaction distance remains constant. However, intermolecular distances are affected by an increased presence of DCJTB, altering the system's morphology as detailed in Chapter 3. Notably, even with a slight reduction in radius, the rates increase for every transfer. Therefore, the reduction in the average intermolecular distance offsets the decrease in spectral overlap and radiative lifetime. Although all processes are depicted together, it is worth noting that the TTS transfer rate is much lower than that of the remaining processes. However, TTS transfers do not directly compete against singlet-singlet transfers, but rather against phosphorescence and nonradiative decay for triplet excitons. At a 0.2 wt% DCJTB concentration, the TTS transfer rate to a first neighbor is 1.21 s^{-1}, whereas the

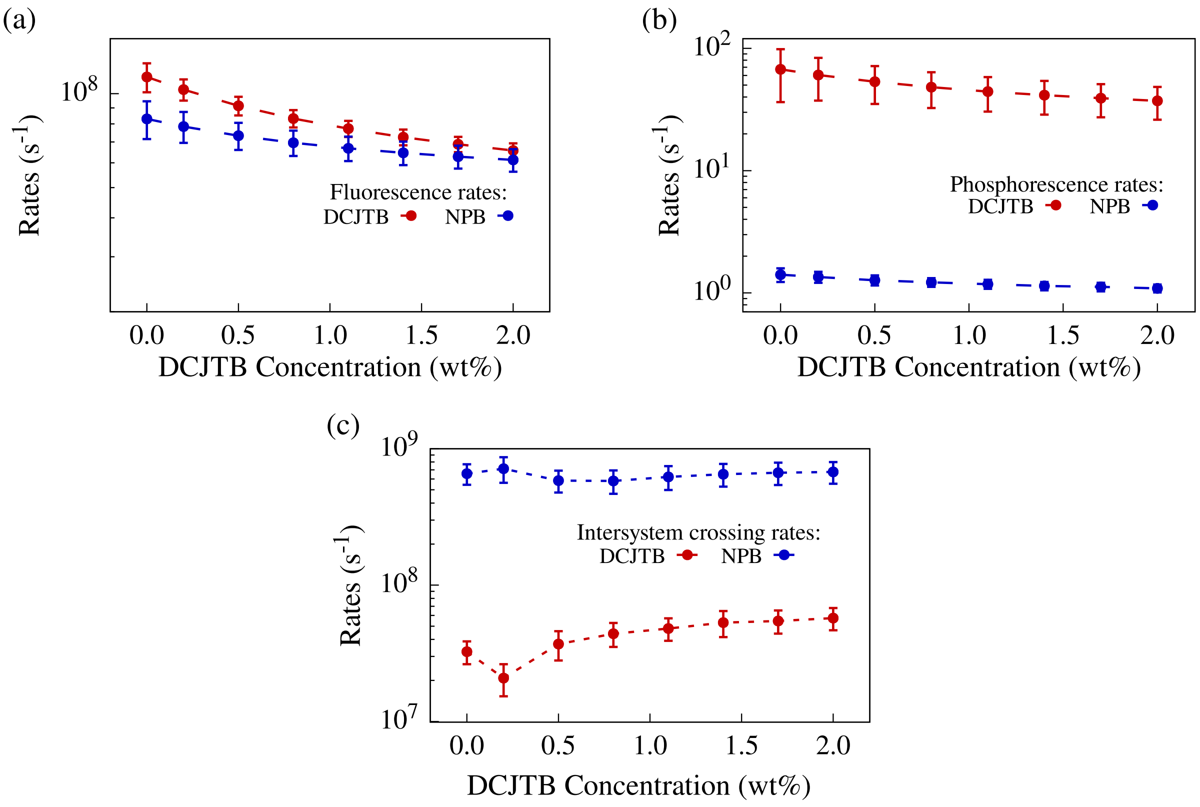

Figure 3.6: Calculated fluorescence (a), phosphorescence (b) and intersystem crossing (c) rates for NPB and DCJTB as a function of DCJTB concentration.

phosphorescence rate reaches 1.35 s^{-1}. This implies that a triplet exciton in NPB has around a 47% chance of undergoing TTS and 53% chance of undergoing phosphorescence. When the presence of DCJTB reaches its maximum, these probabilities become 85% and 15% respectively, almost doubling TTS efficiency. Additionally, another potential competing event is the nonradiative decay from T_1 to S_0. However, at the same concentration, this event has an essentially null calculated rate. As DCJTB concentration rises, the nonradiative decay rate increases, but it remains four orders of magnitude lower than the other competing rates. Therefore, it does not significantly alter the probabilities of each event occurring in our calculations. This is attributed to the high energy of the T_1 state in NPB. Incidentally, these extremely low rISC and triplet nonradiative decay rates are a decisive factor that makes NPB an excellent candidate for serving as an efficient TTS Förster donor molecule. As a matter of fact, these very same properties make NPB an efficient dual emitter when on its own. As such, if one is looking for molecules with an expected efficient TTS transfer mechanism, dual emitters are the natural candidates.

The experimental study examining the interactions between these two compounds successfully

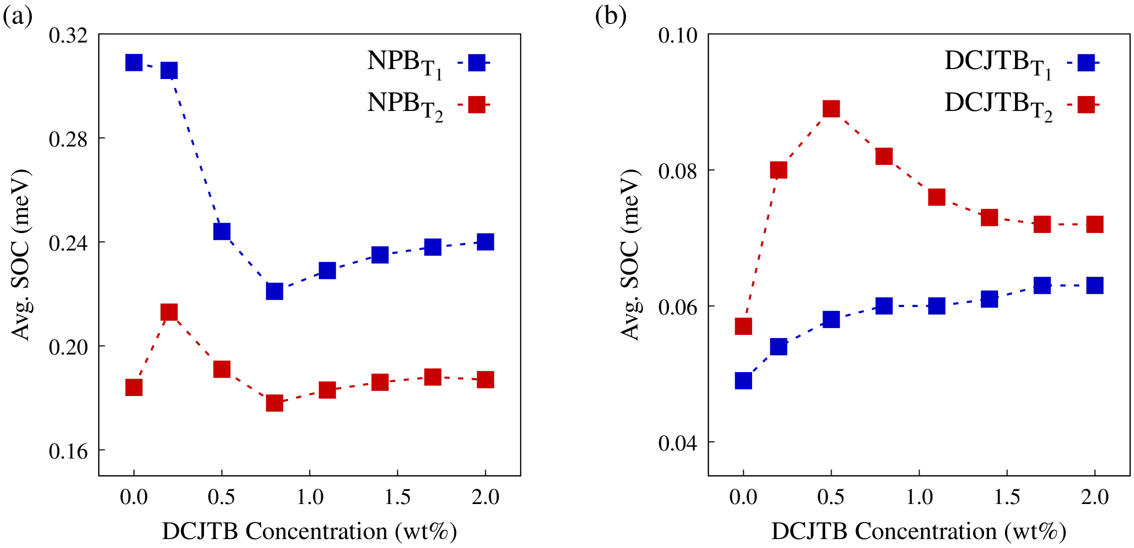

Figure 3.7: Average spin-orbit coupling between the triplet states, T_1 (in blue) and T_2 (in red), and the first excited, S_1, for NPB (a) and DCJTB (b).

obtained time-resolved photoluminescence spectra (TRPL) for NPB as a function of acceptor concentration. Figure 3.9 presents this result, directly extracted and reprinted from ref. 52. It is evident that as acceptor concentration increases, the singlet exciton lifetime decreases. Figure 3.9-a displays the simulated TRPL derived from our KMC simulations, maintaining the same color scheme for acceptor concentration. Notably, the experimental curves for concentrations between 0.8 wt% and 2.0 wt% exhibit a greater skew, indicating that the TRPL is not monoexponential but rather biexponential. While our simulated results align qualitatively with the experimental findings, our model does not fully replicate the skewness observed at higher concentrations. Nevertheless, the overall similarity between both plots indicates that our simulations accurately capture the interactions between NPB and DCJTB.

In the absence of rISC, TTS transfers are the sole mechanism for triplet excitons to be converted into singlet states. Figure 3.10-a depicts the TTS transfer efficiency as measured by the ratio between the number of excitons that underwent TTS followed by fluorescence and the number of $S_1 \rightarrow T_1$ ISC events in NPB at each acceptor concentration. Notably, with higher DCJTB concentration, TTS transfers decrease from over 18% in the lowest non-null acceptor concentration to approximately 5% at a 2.0 wt% DCJTB concentration. This is the result of a combination of factors. First, the highest transfer rate is the singlet-singlet exciton transfer from NPB to DCJTB. Naturally, as the number of DCJTB molecules increase, singlet excitons in NPB are more likely to undergo said transfer than to suffer ISC. Second, with an increase of singlet excitons in DCJTB, the small difference between fluorescence and ISC rates

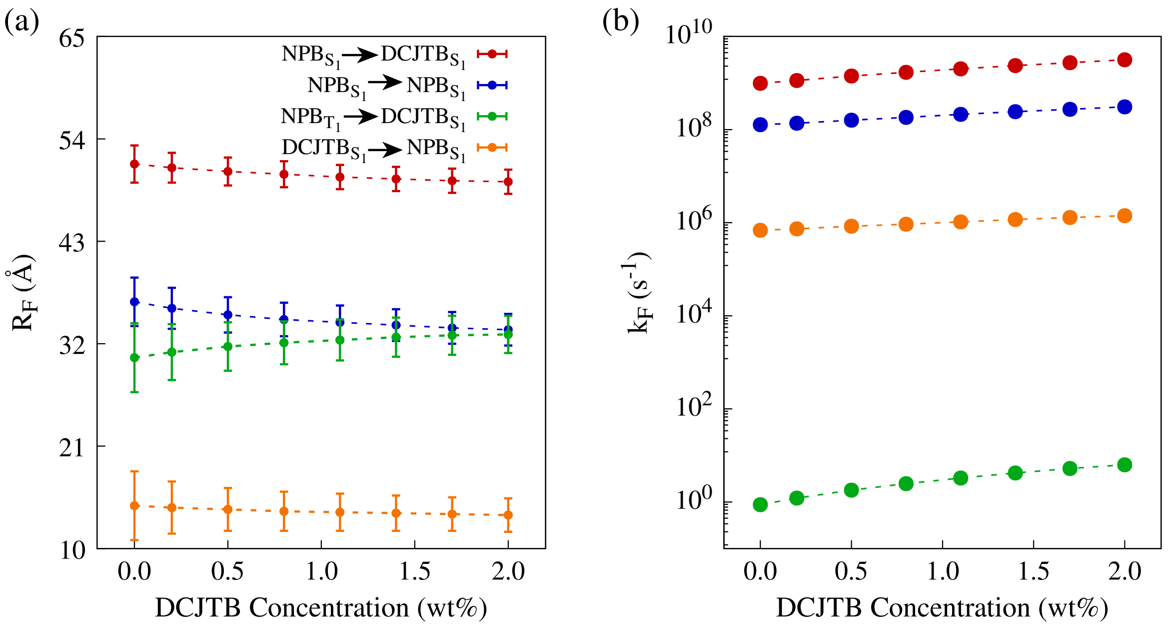

Figure 3.8: (a) Förster radii for different energy transfers within the NPB-DCJTB system. (b) Förster rates to first neighbor as a function of DCJTB concentration.

in that material shows an approximately 40% of ISC taking place. However, due to there being no efficient rISC or TTS mechanism for triplet excitons in DCJTB, after suffering ISC, the resulting triplet can only suffer nonradiative decay or undergo phosphorescence. The inset plot in Figure 3.10-a shows the increase of the nonradiative decay rate for triplet excitons in DCJTB as concentration rises. Notably, said rate can get up to 4×10^4 s^{-1}, which is two orders of magnitude higher than the phosphorescence rate shown in 3.6-c. This means that any triplet exciton resulting from ISC in DCJTB has a 98% probability of decaying nonradiatively. Thus the triplet states in DCJTB would not significantly contribute with any afterglow, which is observed experimentally, seen that samples of pure DCJTB show no afterglow, while samples of NPB in low DCJTB concentrations do display afterglow. Video of the experimental measurements from ref. 52 can be found in https://pubs.acs.org/doi/10.1021/acs.jpclett.8b03668 in the Supporting Information section.

Besides TTS transfers, singlet excitons in DCJTB can be generated by means of regular singlet-to-singlet Förster transfers to DCJTB. However, this happens at a completely different time scale than TTS-derived emission. In Figure 3.10-b, we show the relative contribution of singlet excitons that fluorescence in different timescales in DCJTB. The blue bars account for excitons that fluoresced in DCJTB before 1 μs, which will include prompt fluorescence. The red bars account for excitons that fluoresced

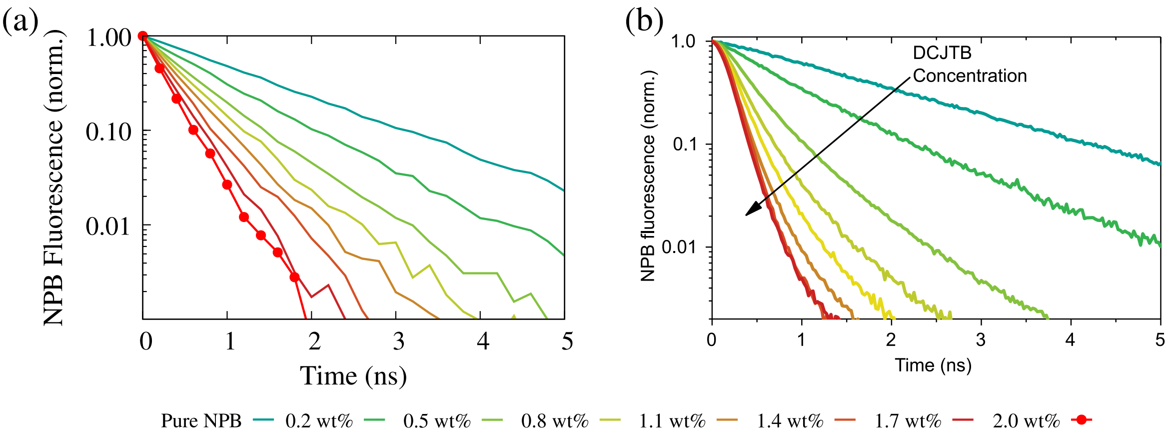

Figure 3.9: Simulated (a) and experimental (b) time-resolved photoluminescence spectra for NPB. Experimental plot is reprinted (adapted) from J. Phys. Chem. Lett. 2019, 10, 310-315. Copyright 2019 American Chemical Society.

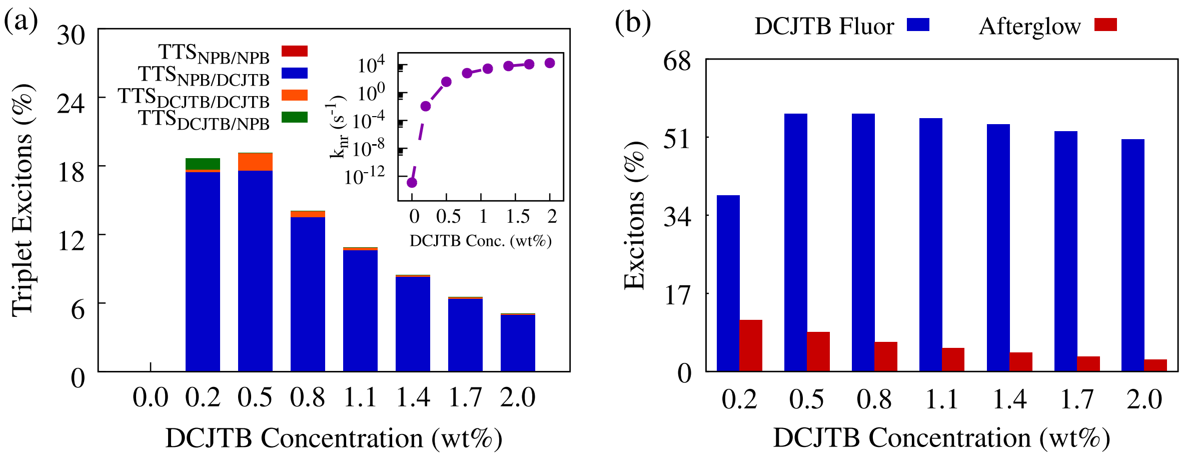

Figure 3.10: (a) Relative amount of TTS occurrence on triplet excitons that resulted in fluorescence in either material. Inset shows the increase of the nonradiative decay for triplet excitons in DCJTB, k_{nr} with acceptor concentration. (b) Percentage of excitons that fluoresced in DCJTB under 1 μs (shown in blue) and over 1 μs (shown in red) relative to the total amount of generated excitons.

after the 1 μs mark. These emissions were labeled as afterglow. The average fluorescence time for each group is shown in Table 3.5, in which we can observe that excitons that fall into the afterglow category are fluorescing in the scale of fractions of a second, much larger than the other group, which fluoresce in the nanoseconds time scale. As DCJTB concentration rises, afterglow occurrence is reduced, which is observed experimentally with samples with lowest non-null DCJTB concentration displaying the most intense afterglow. This result, coupled with the relevant nonradiative decay process of triplet excitons in this material, reveals that afterglow in this system originates not from phosphorescence, as commonly observed, but rather from highly delayed fluorescence resulting from TTS transfers from NPB to DCJTB.

DCJTB Conc. (wt%)	Average fluorescence time (s)	
	Prompt Fluorescence	Afterglow
0.2	1.07×10^{-8}	7.26×10^{-1}
0.5	9.21×10^{-8}	7.19×10^{-1}
0.8	9.30×10^{-8}	6.92×10^{-1}
1.1	9.31×10^{-8}	6.66×10^{-1}
1.4	9.38×10^{-8}	6.66×10^{-1}
1.7	9.46×10^{-8}	6.84×10^{-1}
2.0	9.52×10^{-8}	7.13×10^{-1}

Table 3.5: Average fluorescence time for excitons that fluoresced in DCJTB in the different time scales it occurs, prompt and delayed (afterglow).

CHAPTER 4

SOLVATOCHROMISM THROUGH SOLVENT SUSCEPTIBILITY

4.1 Introduction

In Chapter 1, the phenomenon of solvatochromism was presented as one of the clearest manifestations of how the electronic structure of a molecule interacts with its surrounding medium. Donor–acceptor fluorophores, such as those discussed earlier, often display strong solvent-dependent spectral shifts because their excited states exhibit partial charge-transfer character. While these shifts are routinely used as qualitative indicators of polarity and local environment, their microscopic origin is still most often described in phenomenological terms. The connection between the measurable spectral response and the underlying state-specific stabilization energy remains ambiguous, and empirical scales like ET(30) or Lippert–Mataga relations, although widely applied, do not directly reveal how solvent polarization couples to the electronic configuration of the solute.

In this work, we address that limitation by developing a quantitative framework to describe how different environments stabilize excited states through the concept of solvent susceptibility, χ. As stated, this parameter expresses the first-order solvent correction to the energy of a given electronic state, linking it directly to measurable optical properties. The model formalizes how equilibrium and non-equilibrium solvent polarization contribute separately to the overall energy shift, and introduces scaling relations that allow results obtained for one solvent to be extrapolated to others with known dielectric and refractive indices. This state-specific treatment bridges the gap between purely continuum descriptions and electronic-structure calculations, providing a coherent picture of solvent influence on excited states.

To validate and illustrate the model, we apply it to a series of donor–acceptor fluorophores with diverse electronic characters and practical relevance in optoelectronic and sensing applications. These include molecules commonly used as emitters, polarity probes, and organic semiconductors, whose solvatochromic responses have been experimentally characterized across a wide range of media. By comparing computed and experimental fluorescence shifts, we demonstrate that χ not only captures the direction and magnitude of solvatochromic trends, but also enables the empirical estimation of dielectric constants for thin-film samples directly from optical data. In doing so, this work extends the concept of solvatochromism beyond its traditional descriptive use, presenting solvent susceptibility as a transferable and predictive quantity for connecting environmental polarization to excited-state energetics.

4.1.1 Test molecules

The molecule 4-(dicyanomethylene)-2-methyl-6-(p-dimethylaminostyryl)-4H-pyran, known as DCM2, is a laser dye from the dicyanomethylene pyran family that has been extensively studied in the works of Vladimir Bulovic[99] for its role as a fluorescent dopant in organic optoelectronic devices. Structurally, DCM2 consists of a central pyran ring bearing a strongly electron-withdrawing dicyanomethylene group and an electron-donating dimethylaminostyryl substituent, connected through a conjugated π-system. This push-pull architecture promotes a pronounced intramolecular charge-transfer state, which underlies its broad visible absorption and intense red emission. The studies demonstrated that such features make DCM2 a model system for exploring exciton generation, energy transfer, and host-guest interactions in organic light-emitting diodes (OLEDs), while also serving as a benchmark emitter in understanding the design principles of highly efficient organic dyes. In addition, fluorescence spectra measurements in different solvents as well as in solid state thin films are abundantly available.

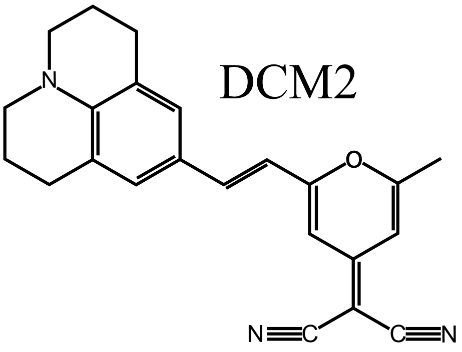

Figure 4.1: Molecular structure of DCM2.

In the same realm of optoelectronic applications, recent works have been performed around the properties one can obtain from the particular structure in the 1-Mes molecule, shown in Figure 4.2. 1-Mes is a triarylborane derivative built around a phenazaborine (PAzB) core, in which the boron atom is embedded within the heteroaromatic ring. Thanks to its architecture, 1-Mes has been explored as an efficient emitter or dopant in OLEDs, where strong intramolecular charge transfer produces tunable fluorescence, and as a responsive unit in chemosensing applications[100].

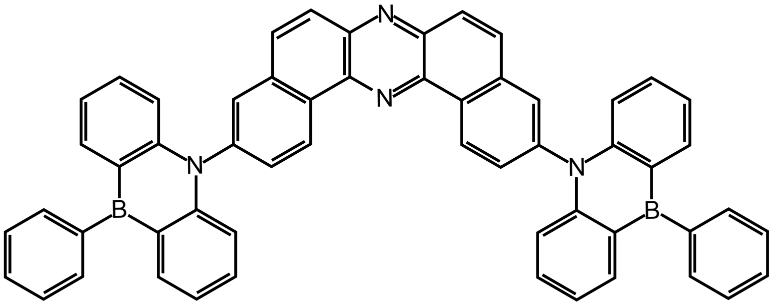

Figure 4.2: Molecular structure of 1-Mes.

In addition to the trending applications of molecules like those detailed above, i.e., TADF and OLEDs, the characteristics that make them ideal candidates for optoelectronic devices also open exciting possibilities in bioimaging. Specifically, in ref. 101, the authors report a new polarity-sensitive lipid-droplet fluorescent probe, named LDs-Red, shown in Figure 4.3. Lipid droplets (LDs) are organelles present in many eukaryotic cells. Their cores are mostly composed of neutral lipids, such as triglycerides and cholesterol esters, which are surrounded by a phospholipid monolayer decorated with proteins. LDs-Red features a donor-acceptor architecture enabling strong red to near-infrared (NIR) emission, minimizing interference from cellular autofluorescence and allowing deeper imaging in biological samples. In practice, it is applied directly to living cells, where it selectively accumulates in lipid droplets due to its lipophilic character. Once localized, its fluorescence intensity and spectral profile respond to the local polarity of the droplet environment, enabling researchers to visualize LDs and assess their biochemical properties in situ. This dual capability — imaging and polarity sensing — distinguishes LDs-Red as a tool for studying lipid metabolism, disease-related lipid alterations, and cellular energy storage, making it a compelling example of the biological application of organic fluorophores, distinct from traditional OLED or TADF uses. In the aforementioned work, authors performed spectral scan imaging to visualize lipid droplets in different cells, both cancerous and not. They observed that the droplets in cancerous cells have typically lower polarity and quantify the effect in terms of the polarity index ET(30)[61], although that is not the most effective way to compare local polarity as we will demonstrate in the following sections.

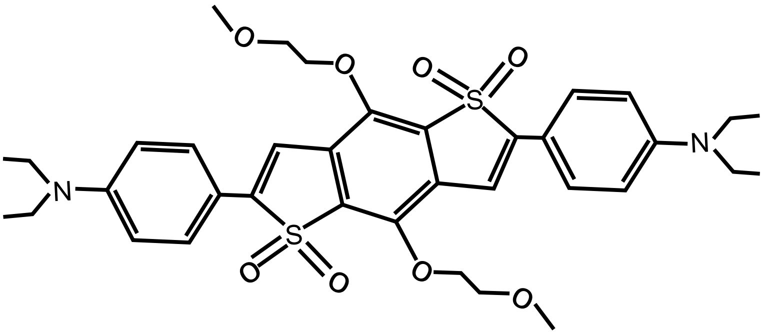

Figure 4.3: Molecular structure of LDs-Red.

In a very similar approach to that of LDs-Red, a quinazolinone-based fluorescent dye, 6-dimethylamino-2-(quinolin-2-yl)- quinazolin-4(3H)-one (DMAQQ) was designed and synthesized in 2019[102]. DMAQQ, shown in Figure 4.4 also features a donor-acceptor framework, in which a dimethylamino group acts as an electron donor and a quinolinyl-substituted quinazolinone core serves as the electron acceptor. This arrangement creates a push-pull system that is sensitive to the polarity of its surrounding environment. The rigid, π-conjugated structure promotes strong fluorescence, and the molecules design allows it to be effective in both one-photon and two-photon bioimaging, as it can penetrate tissues while maintaining high emission efficiency. Its environment-sensitive character makes it suitable for applications beyond simple visualization, including the mapping of cellular polarity, studying lipid-rich compartments, or monitoring local microenvironments in living cells. In their work, the authors observed blue and green on-photon fluorescence emission in HeLa cells with the Pearson's of 0.39, which implies a moderate positive correlation of the blue and green emissions. In practical terms, some regions displayed blue and green simultaneously, but not at a perfect match, i.e. there is overlap, but they could clearly differentiate both signals.

4.2 Modeling and methodology

4.2.1 Solvation model

The authors of ref. 63, whose solvent-related work I show in Chapter 2, elegantly described most of the solvent related interactions. However, a handful of important approximations were done in the

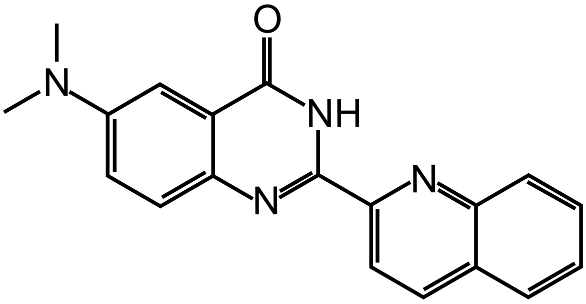

Figure 4.4: Molecular structure of DMAQQ.

process, such that not all molecular system fall within the realm of validity of those approximations. In order to discuss and consider the implications of said approximations, we propose that the energy of the electronic state f under non-equilibrium solvation should be written as:

$$E_f^{neq} = E_f^{vac} - \gamma_f \alpha_{st} - \chi_f \alpha_{opt}, \tag{4.1}$$

where E_f^{vac} is the vacuum energy and $\gamma_f \alpha_{st}$ and $\chi_f \alpha_{opt}$ are the PCM and state-specific contributions to solvent correction, respectively, with χ_f being the susceptibility, defined by equation 2.20. The α terms have already been defined as the proportionality constants that contain the dependence on solvent dielectric constants, whether static ($\alpha_{st} = (\varepsilon - 1)/(\varepsilon + 1)$) or optical ($\alpha_{opt} = (n^2 - 1)/(n^2 + 1)$), n being the solvent's refractive index.

The γ_i and χ_i terms can be calculated with two single point TD-DFT calculation, one in vacuum and one in solution with PCM and state-specific corrections. For the γ_i term we have

$$\gamma_i = \frac{E_i^{PCM} - E_i^{vac}}{\alpha_{st}}. \tag{4.2}$$

The molecules' solvent susceptibilities are calculated from combining the perturbative linear response (λ_i^{ptLR}) and perturbative state-specific (λ_i^{ptSS}) as the non-equilibrium terms and it can be expressed by:

$$\chi_i = \frac{\lambda_i^{ptLR} + \lambda_i^{ptSS}}{\alpha_{opt}}. \tag{4.3}$$

Under equilibrium solvation, Equation 4.1 is changed to

$$E_i^{eq} = E_i^{vac} - \gamma_i \alpha_{st} - \chi_i \alpha_{st}. \tag{4.4}$$

In the case of the ground state — where we assume equilibrium for when S_0 is the initial state —, we have

$$\begin{aligned} E_0^{eq} &= E_0^{vac} - \gamma_0\alpha_{st} - \chi_0\alpha_{st} && (4.5)\\ &= E_0^{vac} - (\gamma_0 + \chi_0)\alpha_{st} && (4.6)\\ &= E_0^{vac} - \gamma_0'\alpha_{st} && (4.7) \end{aligned}$$

in which we condensed γ_0 and χ_0 into a single term γ_0', since both of them scale with α_{st}, making them indistinguishable. This γ_0' term can be obtained by computing the ground state energy in vacuum and in solution with PCM.

Transition Energies

Transition energies between electronic states i and f are given by

$$\begin{aligned} \Delta E_{fi} &= E_f^{neq} - E_i^{eq} && (4.8)\\ &= E_f^{vac} - \gamma_f\alpha_{st} - \chi_f\alpha_{opt} - (E_i^{vac} - \gamma_i\alpha_{st} - \chi_i\alpha_{st}) && (4.9)\\ &= E_f^{vac} - E_i^{vac} + (\gamma_i + \chi_i - \gamma_f)\alpha_{st} - \chi_f\alpha_{opt} && (4.10)\\ &= \Delta E_{fi}^{vac} + (\gamma_i + \chi_i - \gamma_f)\alpha_{st} - \chi_f\alpha_{opt}. && (4.11) \end{aligned}$$

Note that equation 4.11 is identical to the general transition energy expression 2.25 except for the inclusion of the PCM terms. Said terms are originally discarded due to the fact they primarily affect the ground state by reshaping its orbitals and it was deemed negligible to the group of molecules analyzed. Additionally, calculating those terms would require a second single-point calculation, increasing the associated computational cost to the method. By including those corrections here, we improve the description of the model to be able to include molecules for which that difference between PCM terms are not negligible. Lastly, the solvent index (m), $m = 1,2$ is suppressed here without any loss of physical meaning.

When the initial state is the ground state ($i = S_0 \equiv 0$), we obtain the absorption energy, which can be written as follows:

$$\begin{aligned}\Delta E_{f0}^{abs} &= \Delta E_{f0}^{vac} + (\gamma_0 + \chi_0 - \gamma_f)\alpha_{st} - \chi_f \alpha_{opt} \qquad (4.12)\\ &= \Delta E_{f0}^{vac} + (\gamma'_0 - \gamma_f)\alpha_{st} - \chi_f \alpha_{opt} \qquad (4.13)\\ &= \Delta E_{f0}^{vac} - (\gamma_f - \gamma'_0)\alpha_{st} - \chi_f \alpha_{opt}. \qquad (4.14)\end{aligned}$$

Comparing equation 4.14 to equation 2.27, we can see that the latter is the former when $\gamma'_0 - \gamma_f \rightarrow 0$. However, it is worth noting that the second to last term on the right hand side of equation 4.14 can act as a blue shift term in cases when the polarity of the ground state is higher than that of the excited state, i.e. $\gamma'_0 - \gamma_f > 0$.

With the same approach, we write the emission energy considering the excited state as the initial one and the ground state as the final, yielding

$$\begin{aligned}\Delta E_{0i}^{emi} &= E_0^{neq} - E_i^{eq} \qquad (4.15)\\ &= E_0^{vac} - \gamma_0 \alpha_{st} - \chi_0 \alpha_{opt} - (E_i^{vac} - \gamma_i \alpha_{st} - \chi_i \alpha_{st}) \qquad (4.16)\\ &= (E_0^{vac} - E_i^{vac}) + (\gamma_i + \chi_i - \gamma_0)\alpha_{st} - \chi_0 \alpha_{opt} \qquad (4.17)\\ &= \Delta E_{0i}^{vac} + (\gamma_i - \gamma_0 + \chi_i)\alpha_{st} - \chi_0 \alpha_{opt}, \qquad (4.18)\end{aligned}$$

where we can use $\chi_0 + \gamma_0 = \gamma'_0$ such that $-\gamma_0 = \chi_0 - \gamma'_0$, which in turn leads to

$$\begin{aligned}\Delta E_{0i}^{emi} &= \Delta E_{0i}^{vac} + (\gamma_i - \chi_0 - \gamma'_0 + \chi_i)\alpha_{st} - \chi_0 \alpha_{opt} \qquad (4.19)\\ &= \Delta E_{0i}^{vac} + (\gamma_i - \gamma'_0 + \chi_i)\alpha_{st} + \chi_0(\alpha_{st} - \alpha_{opt}). \qquad (4.20)\end{aligned}$$

Note that in the case of emission $E_0 > E_i$, which would lead us to deal with negative numbers. However, it is practical to define it as a positive number, by defining that $|\Delta E_{0i}^{emi}| = \Delta E_{i0}^{emi}$, turning the last expression to

$$\Delta E_{i0}^{emi} = \Delta E_{i0}^{vac} - (\gamma_i - \gamma'_0 + \chi_i)\alpha_{st} - \chi_0(\alpha_{st} - \alpha_{opt}). \qquad (4.21)$$

Lastly, if we identify the ground state susceptibility (χ_0) with that of the initial state of this transition (χ_i), i.e. $\chi_0 = \chi_i$, we arrive at the expression:

$$\Delta E_{i0}^{emi} = \Delta E_{i0}^{vac} - (\gamma_i - \gamma'_0 + \chi_i)\alpha_{st} - \chi_i(\alpha_{st} - \alpha_{opt}). \qquad (4.22)$$

The inclusion of the PCM term in the energy of each state and by approximation the susceptibility of the ground state with that of the excited state, we allow for the last term to present itself naturally, which we promptly identify as the solvent reorganization energy, explicitly presented in equation 2.32. The previous absence of that term resulted in the overestimation of emission energies for high polarity solvents, as it only contributes significantly when $\alpha_{st} >> \alpha_{opt}$, i.e. high values of ε.

We must keep in mind that the shift depends on the initial state. If that state has a local excitation (LE) character, then the shift would have to be almost null, which is well documented, even for highly polar solvents. This entails that χ_i and the γ corrections would be small, which means the second term on the right hand side of equation 4.21 is expected to be negligible. In order to preserve the small shift of a LE initial state, the last term on the right hand side would also have to be neglected, regardless of the character of the ground state (and thus, regardless of the value of χ_0) and the polarity of the solvent, which entirely defeats the purpose of considering the solvent in the emission energies. Taking water as a solvent, for instance, we have $\varepsilon = 78.4$ and $n = 1.333$, leading to $\alpha_{st} - \alpha_{opt} \approx 0.695$. If that difference is not mitigated by χ_0, the shift would be severely overestimated, justifying the approximation $\chi_0 = \chi_i$ for LE states. However, if the initial state is of CT character, that is, of high susceptibility, the observed shift has to be larger than that of a LE state. If the final state has a stronger CT nature as well, for lower polarity solvents, the last term on the right hand side might be overestimated, leading to the underestimation of the energy. Another scenario of low polarity solvent and lower CT character than that of the initial state results in the last term on the right hand side to be underestimated, which would, in turn, result in a higher energy (lower shift). Now for a final state with stronger CT character in a high polarity solvent, then the aforementioned term would be overestimated and so on. Not making the approximation can act both as a factor of underestimation and overestimation of the energies in question, depending on the characters of the states involved. In that sense, we observed that making the approximation that $\chi_0 = \chi_i$ yields better results, seen that the character of the initial state tends to be of higher importance.

Solvent Reorganization Energies

As already defined, the solvent reorganization energy, λ^{sol}, quantifies the energetic penalty associated with the solvent not being in its optimal arrangement for the electronic state reached after a vertical transition. A large λ^{sol} implies that a significant portion of the solvent must physically rearrange upon excitation or emission. This tends to broaden the spectra and makes the Stokes shift larger. It is defined as $\lambda_f^{sol} = E_f^{neq} - E_f^{eq}$. We can subtract Equation 4.4 from Equation 4.1 for state f to obtain

$$\lambda_f^{sol} = E_f^{neq} - E_f^{eq} \tag{4.23}$$

$$= E_f^{vac} - \gamma_f \alpha_{st} - \chi_f \alpha_{opt} - (E_f^{vac} - \gamma_f \alpha_{st} - \chi_f \alpha_{st}) \tag{4.24}$$

$$= \chi_f (\alpha_{st} - \alpha_{opt}). \tag{4.25}$$

In the case of emission, the final state is the ground state and $\lambda_f^{sol} = \chi_0(\alpha_{st} - \alpha_{opt})$. Nonetheless, since we defined before the ground state susceptibility to be equal to that of initial excited state, then

$$\lambda_0^{sol} = \chi_i(\alpha_{st} - \alpha_{opt}). \tag{4.26}$$

With this expression for the solvent reorganization energy, we note that Equation 4.22 corresponds to

$$\Delta E_{i0}^{emi} = \Delta E_{i0}^{vac} - (\gamma_i - \gamma_0 + \chi_i)\alpha_{st} - \chi_i(\alpha_{st} - \alpha_{opt}) \tag{4.27}$$

$$= E_i^{vac} - E_0^{vac} - \gamma_i \alpha_{st} + \chi_i \alpha_{st} + (\gamma_0 + \chi_0)\alpha_{st} - \lambda_0^{sol} \tag{4.28}$$

$$= (E_i^{vac} - \gamma_i \alpha_{st} - \chi_i \alpha_{st}) - (E_0^{vac} - \gamma_0 \alpha_{st} - \chi_0 \alpha_{st}) - \lambda_0^{sol} \tag{4.29}$$

$$= (E_i^{eq} - E_0^{eq}) - \lambda_0^{sol}, \tag{4.30}$$

which means that the emission energy is the difference between the equilibrium solvation energies of the excited and ground state discounted by the solvent reorganization of the ground state. In a previous work, a similar expression was employed for emission energies, but without the extra λ_0^{sol} term[63]. This previous work also employed a single TD-DFT calculation in solution, which prevented the determinations of the γ terms.

4.2.2 The Stokes' Shift

As we know, the Stokes' shift is the difference between absorption and emission energies. Neglecting variations in γ and χ with geometry, we get it by subtracting Equation 4.22 from Equation 4.14, which produces

$$\Delta_{Stokes}^{sol} = \Delta E_{f0}^{abs} - \Delta E_{i0}^{emi} \tag{4.31}$$

$$= \Delta E_{f0}^{vac} - \Delta E_{i0}^{vac} - \gamma_f \alpha_{st} + \gamma_0 \alpha_{st} - \chi_f \alpha_{opt} + \gamma_i \alpha_{st} - \gamma_0 \alpha_{st} + \chi_i \alpha_{st} + \chi_f \alpha_{st} - \chi_f \alpha_{opt}, \tag{4.32}$$

in which the difference of the first two terms on the right hand side is the Stokes shift in vacuum, hence Δ_{Stokes}^{vac}. In addition, note that the same excited state is indexed by f in the absorption and by i in the emission, in which case, we can replace all i indices by f, leading us to,

$$\Delta_{Stokes}^{sol} = \Delta_{Stokes}^{vac} - 2\chi_f \alpha_{st} - 2\chi_f \alpha_{opt} \tag{4.33}$$

$$= \Delta_{Stokes}^{vac} + 2\chi_f (\alpha_{st} - \alpha_{opt}) \tag{4.34}$$

Marcus Theory and the Partition of Reorganization Energy

Marcus theory was originally developed to describe rates of electron transfer reactions. Its central idea is that the energetics of transferring an electron between two molecular states can be modeled as the intersection of two harmonic free-energy surfaces, each corresponding to one electronic state. The key parameter controlling the activation barrier is the reorganization energy (λ), which quantifies how much the nuclei and environment must reorganize to accommodate the change in electronic distribution.

Traditionally, λ is partitioned into two contributions:

- **Inner-sphere reorganization energy (λ_{inner}):** Structural rearrangements of the solute itself (bond lengths, bond angles, torsions). This is the intrinsic cost of distorting the molecular geometry between electronic states. Exists even in the gas phase.

- **Outer-sphere reorganization energy (λ_{outer} or λ_{sol}):** Polarization and reorientation of the surrounding medium (solvent or environment). This depends on solvent polarity and vanishes in vacuum but can dominate in polar solvents.

Thus, the total reorganization energy is

$$\lambda = \lambda_{\text{inner}} + \lambda_{\text{outer}}.$$

In spectroscopy, this framework provides a natural interpretation of the Stokes shift, which can be expressed as approximately twice the total reorganization energy. The observed spectral shift arises from both internal geometric relaxation of the molecule (inner sphere) and solvent reorganization (outer sphere).

Borrowing the terminology from Marcus Theory shown above, it is reasonable to say that $\Delta^{vac}_{Stokes} \approx 2\lambda_{inner}$, where each λ_{inner} contribution comes from each transition (absorption and emission), we see that our expressions for absorption and emission energies produce the result that the total Stokes' shift is just twice the total reorganization energy:

$$\Delta^{sol}_{Stokes} = \Delta^{vac}_{Stokes} + 2\chi_f(\alpha_{st} - \alpha_{opt}) \tag{4.35}$$

$$\approx 2\lambda_{inner} + 2\lambda_{sol} \tag{4.36}$$

$$\approx 2(\lambda_{inner} + \lambda_{sol}). \tag{4.37}$$

4.3 Experimental determination of χ and ΔE^{vac}_{i0}

Equation 4.22 can be further analyzed to fit experimental emission energies, as measured from experimental peaks. We can expand the expression to

$$\Delta E^{emi}_{i0} = \Delta E^{vac}_{i0} - (\gamma_i - \gamma_0')\alpha_{st} - \chi_i\alpha_{st} - \chi_i(\alpha_{st} - \alpha_{opt}). \tag{4.38}$$

However, for this specific application, we can make use of the approximation $\gamma_i - \gamma_0' \approx 0$, which corresponds to saying that pure PCM corrections to the ground and excited states are nearly equal. As a proof of concept, we have calculated these corrections for DCM2 and DMAQQ ensembles, and calculated the distribution of the difference between those terms. In Figure 4.5 we see that the average and mean values for both molecules are sufficiently close to zero and confirm the validity of the approximation for some compounds.

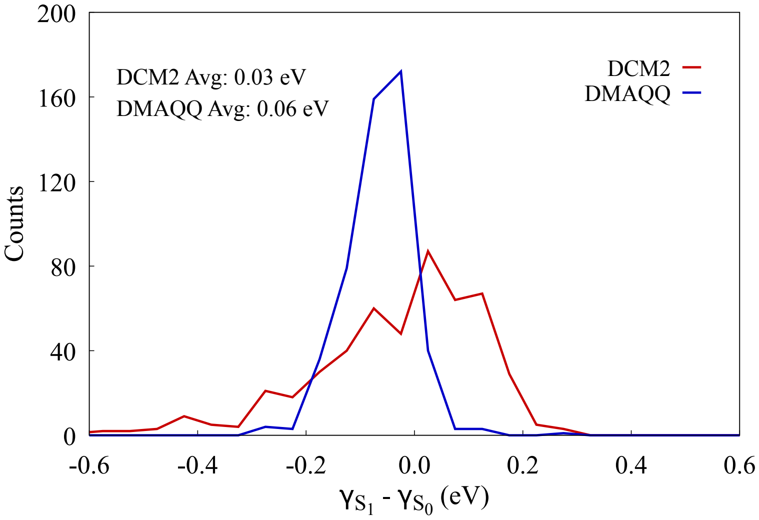

Figure 4.5: Distribution for $\gamma_{S_1} - \gamma_{S_0}$ for DCM2 and DMAQQ ensembles.

Thus, we arrive at

$$\Delta E_{i0}^{emi} = \Delta E_{i0}^{vac} - \chi_i (2\alpha_{st} - \alpha_{opt}). \tag{4.39}$$

This is a powerful expression due to the fact that if we have enough data points of emission energies in different solvents (whose ε and n are known, thus α_{st} and α_{opt} are known as well), ΔE_{i0}^{vac} and χ_i became parameters in a linear fit of the function ΔE_{i0}^{emi}, making them easily determinable. Furthermore, once they are obtained, we can reverse the process and infer the static dielectric constant of solid state samples from fluorescence spectra collected under several conditions. The fitting procedure provides us with the mean estimates $\mu = (\langle \Delta E_{emi}^{vac} \rangle, \langle \chi \rangle)$ and a covariance matrix M of the two parameters. From equation 4.39, we can write

$$\alpha_{st} = \frac{\Delta E_{emi}^{vac} - \Delta E_{emi}}{2\chi} + \frac{\alpha_{opt}}{2} \tag{4.40}$$

where ΔE_{emi} are emission peak energies taken from measurements conducted in some medium with unknown ε. We select the appropriate refractive index n to compute α_{opt}, then sample ΔE_{emi}^{vac} and χ values from a bivariate normal distribution with mean μ and covariance M — from where we obtain the adequate widths for both parameters, as well as the correlation between them — and apply to to equation 4.40. From each pair $(\langle \Delta E_{emi}^{vac} \rangle, \langle \chi \rangle)$, we compute the dielectric constant from

$$\varepsilon = \frac{1 + \alpha_{st}}{1 - \alpha_{st}}. \tag{4.41}$$

Then we discard all cases in which $\varepsilon < n^2$, since these are not physical. The remaining distribution gives us a median, which we report as the best estimator for ε. The error in the determination of ε comes from taking the 16th and 84th percentiles, where the former will serve as the lower bound of the estimation while the latter represents the upper uncertainty bounds. For each molecule to which we apply these proceedings, we employed a total of 10000 samples.

This analysis can be done through the use of the spec2epsilon package[103]. It allows the user to dynamically visualize the data in such way that the testing of multiple refractive indexes and the selective choice of solvents is processed on the fly. Although the analysis starts with a linear fit, the use of the correlation matrix to obtain the bivariate normal distribution is not as fast of a procedure and it is done without need for any work on the user's part.

4.4 Electronic structure

The electronic structure properties of the analyzed molecules were calculated by means of DFT and TD-DFT. The functional LC-ωPBE was employed with the 6-31G+(d,p) basis set for DCM2 and DMAQQ, while for 1-Mes the functional PBE0 with the same basis set was also employed for the geometry optimization. The difference of functional for 1-Mes will be detailed further ahead in the results section. For each molecule, the functional's range separation parameter was tuned non-empirically, following the protocol presented in ref. 85. After functional tuning, optimized geometries and their respective normal mode frequencies were obtained using the procedure detailed in Chapter 2. The calculations performed in that procedure provide us with all the γ corrections, as well the theoretical susceptibility, χ, according to expressions 4.2 and 4.3, respectively. Relevant photophysical rates were calculated using the NEMO software [104] interfaced with Q-Chem 5.0[68].

The following results related to the employment of these methods and proceedings will be broken into two sections. The first one will show the validity of expression 4.22 for a selection of organic molecules displaying the necessary nuances of the performed electronic structure calculations. The second one will show how to determine effective dielectric constants of solid state samples from empirical emission data in different solvents.

4.5 Results A - Electronic structure calculations with adequate solvent corrections

We start this section by providing the reader with the calculated values of each term present in equation 4.22 for the three test molecules that will be discussed in this section, DCM2, DMAQQ and 1-Mes. Table 4.1 shows the values of ΔE^{vac}, χ and $(\gamma_1 - \gamma_0)$ for said molecules. They were calculated over the two-step TD-DFT calculation on the optimized geometry, requiring the "opt" index as results coming from nuclear ensembles will be included further ahead.

We can see that 1-Mes presents itself as the most solvent sensitive compound due to it having the highest solvent susceptibility, with a value of 0.77 eV, followed by DMAQQ with 0.48 eV and DCM2 with 0.46 eV. That ordering of χ values indicates the corresponding order of CT state intensity in each compound. Although DCM2 and DMAQQ have very different applications, their similar value of susceptibility make them sensitive enough to act as polarity probes. We can also see that the $(\gamma_1 - \gamma_0)^{opt}$

Molecule	ΔE_{vac}^{opt} (eV)	χ^{opt} (eV)	$(\gamma_1 - \gamma_0)^{opt}$ (eV)
DCM2	2.56	0.46	-0.007
DMAQQ	2.94	0.48	-0.050
1-Mes	3.01	0.77	-0.370

Table 4.1: Vacuum energies, solvent susceptibilities and the difference between PCM corrections for DCM2, DMAQQ and 1-Mes obtained from a single optimized geometry of each molecule.

term nears zero for DCM2 and DMAQQ, while that is not the case for 1-Mes. As we will discuss further ahead, 1-Mes presents itself as a challenging molecule to be characterized in terms of its photophysics.

The independent works of E. Lippert and N. Mataga in the last century established that solvent polarity can significantly alter a molecule's emission properties. By studying the Stokes shift of various molecules in solvents of differing polarity, they independently derived an equation linking emission energy shifts to changes in the molecule's dipole moment. Their fundamental equation was derived under the linear response approximation for solute-solvent dipole interactions, with the solute assumed to be situated in a spherical Onsager cavity of radius a and unit dielectric constant. Using a dielectric continuum to represent the solvent, this model allowed them to describe solvation effects without detailing each solvent molecules interaction with the solute [105, 106].

While widely used, the Lippert-Mataga (LM) formalism remains a phenomenological approximation. It assumes a point dipole model of the solute, a spherical and static solvent cavity, and a linear and symmetric solvation response to dipole changes between the ground and excited states. These simplifications allow it to capture broad trends in solvent-induced spectral shifts, but they also introduce significant limitations. Most notably, the LM model treats the excited state as a simple dipole perturbation and neglects how the solventsolute system mutually polarizes in response to excitation. As a result, it cannot capture cases where the excited state has strong CT character, or where solvation leads to non-linear stabilization of the excited-state electron density. In such cases, the emission energy does not scale linearly with solvent polarity, and the assumptions of the LM model break down. When modeling absorption or emission, it is essential to account for the fact that the solvent response to vertical electronic transitions is only partially relaxed. These situations require a perturbative state-specific solvation model, like the one presented here, which treat the solvation energy differently for each electronic state and consider non-equilibrium effects appropriately [107, 108, 63].

The equation reads [106, 109, 110]

$$\Delta\nu = \nu_{abs} - \nu_{emi} = \frac{2\Delta f}{hc}\frac{(\mu_e - \mu_g)^2}{a^3} \tag{4.42}$$

in which ν refers to the absorption or emission wave numbers, Δf is known as the solvent polarity function [111, 112, 113], h is Planck's constant, c is the speed of light, μ_e and μ_g are dipole moments for the excited and ground states, respectively. The polarity function can be expressed in terms of the solvent's dielectric constant ε and its refractive index n, as shown in

$$\Delta f = \frac{\varepsilon - 1}{2\varepsilon + 1} - \frac{n^2 - 1}{2n^2 + 1} \tag{4.43}$$

It is worth noting that in the case of vacuum ($\varepsilon = 1, n = 1$), it would imply a null Stokes shift. However, that is not accurate for the absolute majority of organic molecules. Thus, we need to account for the red-shift in vacuum, which stems from the mere change in geometry between the ground and corresponding excited state. The equation then reads

$$\Delta\nu = \nu_{abs} - \nu_{emi} = \frac{2\Delta f}{hc}\frac{(\mu_e - \mu_g)^2}{a^3} + \Delta\nu^{vac} \tag{4.44}$$

which can be written in terms of the energy since $E = hc\nu$, yielding

$$\begin{aligned} E_{abs} - E_{emi} = &\left(\frac{\varepsilon - 1}{\varepsilon + 1/2}\right)\frac{(\mu_e - \mu_g)^2}{a^3} - E_{emi}^{vac} \\ &- \left(\frac{n^2 - 1}{n^2 + 1/2}\right)\frac{(\mu_e - \mu_g)^2}{a^3} + E_{abs}^{vac}. \end{aligned}$$

Additionally, can be reorganized in terms of the Stokes' shift and making $a^3 = V$, leading to

$$\Delta_{Stokes}^{sol} = \Delta_{Stokes}^{vac} + \frac{(\mu_e - \mu_g)^2}{V}\left(\frac{\varepsilon - 1}{\varepsilon + 1/2} - \frac{n^2 - 1}{n^2 + 1/2}\right). \tag{4.45}$$

We can compare equations 4.45 and 4.39 and see that they share a common structure. There is a small difference between the denominator of α_{st} and α_{opt} compared to the last term on the right hand side of equation 4.45. However, we can make a straight forward comparison between twice our solvent susceptibility (one coming from absorption and one coming from emission — important because LM equation is written in terms of Stokes shift, whereas our equations are for the corrections of each transition) and LM dipole term. However, our formulation decouples the absorption and emission contributions, allowing for the analysis of solvatochromism in terms of emission measurements only. We still make this comparison by considering our form of the α denominators. In order to do that, we apply the nuclear ensemble method with 500 geometries to DCM2 and DMAQQ to calculate the ptSS and ptLR corrections for each conformation. Additionally, we include a volume calculation for each of these conformations on top of the difference between the two dipole moments in order to obtain the value of the LM susceptibility. Figure 4.6-a shows that the ptSS corrections for both molecules is what correlates to the LM term. We can see that for both molecules, the relation between $2ptSS/\alpha_{opt}$ and $(\mu_e - \mu_g)^2/V$ is linear, but not of the $y = x$ type, which implies that the state-specific correction is only part of the problem's description. In Figure 4.6-b, we show the comparison of $2\chi_{S_1}$ and $(\mu_e - \mu_g)^2/V$. We can see the former revolves nearly constant around 0.9 eV for both molecules while the latter ranges from 0 eV to 0.5 eV for DCM2 and from 0.2 eV to 1.4 eV. Considering the values shown in Table 4.1, with χ^{opt} being 0.46 eV and 0.48 eV for DCM2 and DMAQQ, respectively, $2\chi_{S_1} \approx 0.9$ eV obtained from the ensembles are in excellent agreement with the optimized geometry calculation. For 1-Mes, the same agreement was not possible to achieve, for a variety of reasons.

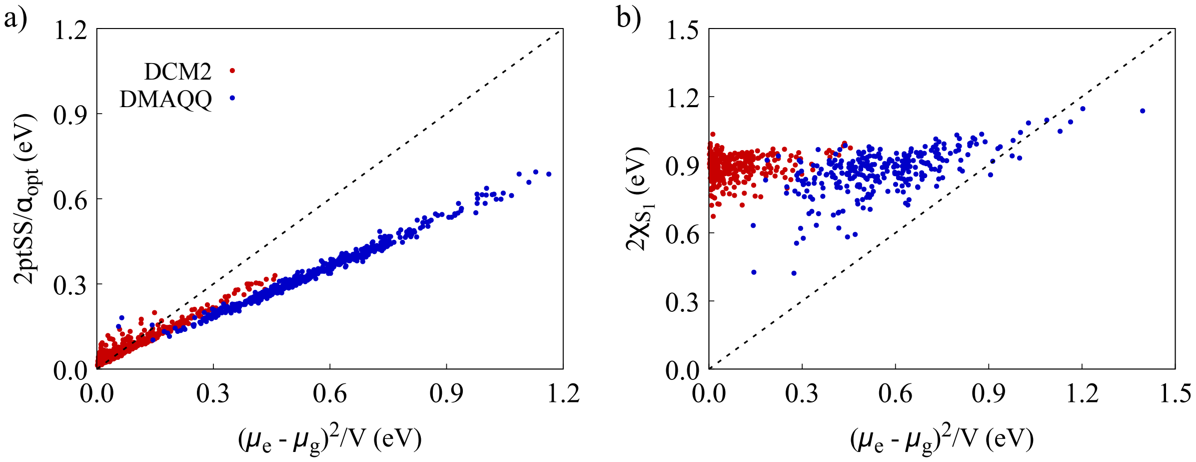

Figure 4.6: Comparison for susceptibility values from the Lippert-Mataga expression (χ_{LM}) and state-specific $(2ptSS/\alpha_{opt})$ solvent correction (a) and the susceptibility calculated from ensemble data (b) for DCM2 and DMAQQ.

In an attempt to perform the same comparison between the terms plotted in Figure 4.6 for 1-Mes, we stumbled upon a myriad of issues. Originally, we performed the geometry optimization with the same functional as DCM2 and DMAQQ, ωPBE. However, that showed an extremely low susceptibility for the S_1 state, which we know not to be the case from experimental data[100]. That led us to go back to the geometry optimization process, during which we changed the functional from ωPBE to $PBE0$. That functional led to the geometry optimization that when used as input to calculate the energies with the ωPBE functional, yielded the result for ΔE_{vac}^{opt}, χ^{opt} and $(\gamma_1 - \gamma_0)^{opt}$ shown in Table 4.1. The fact that $\gamma_1 - \gamma_0$ is not approximately zero for 1-Mes alone is by itself an indicator of the many peculiarities surrounding the characterization of that molecule.

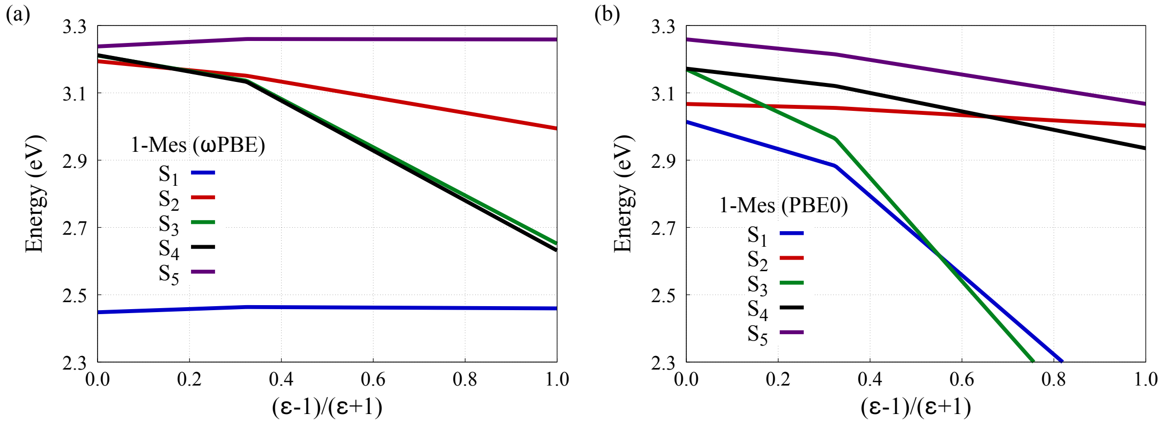

Figure 4.7: Emission energy for states S_1 through S_5 of 1-Mes as function of α_{st} using the ωPBE (a) and $PBE0$ (b)functionals.

Figure 4.7-a shows the emission energy for the first five excited states of 1-Mes as α_{st} increases with functional ωPBE. We can see that the first excited state barely has any change in energy as α_{st} progresses. States S_3 and S_4 are nearly degenerate as they share basically the same energy for all values of ε. S_5 has a similar profile to S_1, displaying little change due to solvent interaction. We can also see that at $\alpha_{st} \approx 0.17$, the S_2 and S_3 (and S_4) states have their energy inverted, with the latter having its energy decrease much more intensely than S_2, such that S_4 becomes S_2 and S_2 becomes S_4. This reorganization of excited state happens due to different CT characters of each state. In this case, S_3 and S_4 appear much more susceptible to solvation effects — higher χ — than S_2. Nevertheless, as previously stated, experimental data reports that S_1 is definitely a state of elevated CT character, indicating that ωPBE has failed to calculate the excited states energies. Figure 4.7-b, on the other hand, displays the same plot for the energies calculated with the geometry optimization performed with the $PBE0$ functional. It is noticeable that both the S_1 and S_3 states display a more elevated CT character, such that for $\alpha_{st} \approx 0.18$, S_3 quickly has lower energy than S_2 in vacuum; while for $\alpha_{st} \geq 0.55$, that is for $\varepsilon \geq 3.44$, the same state also flips S_1.

The same investigation is made for DCM2 and DMAQQ, with which we used the ωPBE functional to inquire whether their S_1 states are flipped by others at any solvent polarity. Figure 4.8-a shows

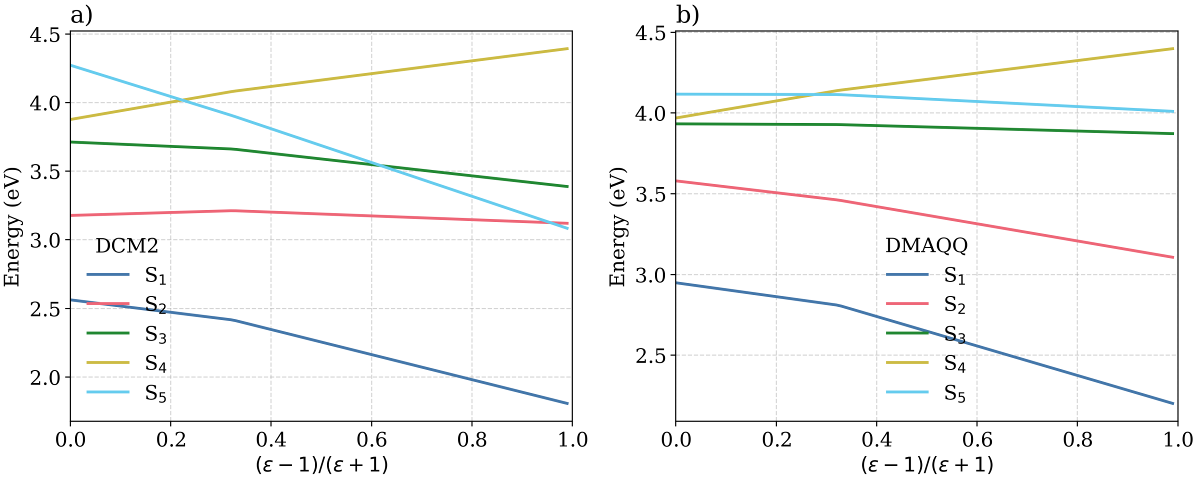

Figure 4.8: Emission energy for states S_1 through S_5 as function of α_{st} for DCM2 (a) and DMAQQ (b).

the energy plot for DCM2. One can see that state S_1, although it does not display the highest CT character, it shows a maximum energy variation of approximately 1.1 eV. States S_2 and S_3, on the other hand do not present themselves with elevated susceptibilities, seen as those do not display significant energy changes with α_{st}. Alternatively, we can see that S_4 and S_5 flip $\alpha_{st} \approx 0.25$, with the latter also flipping S_3 and S_2 at $\alpha_{st} \approx 0.6$ and $\alpha_{st} \approx 0.9$, respectively. Figure 4.8-b displays the equivalent plot for DMAQQ, in which we see that only S_4 and S_5 flip for $\alpha_{st} > 0.3$. States S_1 and S_2 have a similar profile in energy change, with the former displaying stronger CT character. Lastly, we can see that S_3 seems to be a strong localized excitation, i.e. $\chi \approx 0$, since its energy is constant for any solvent changes.

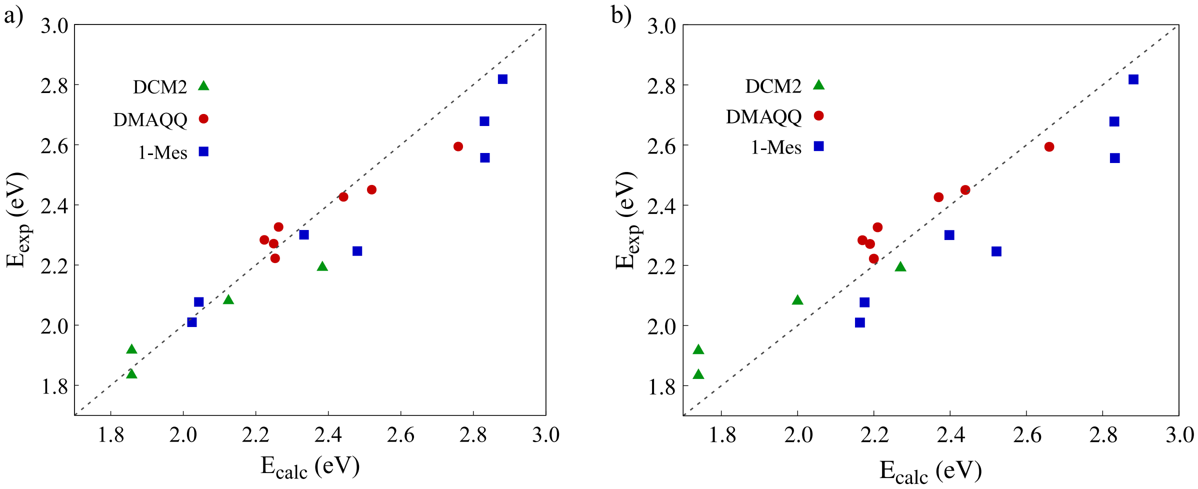

Figure 4.9: Experimental and calculated emission energies for DCM2, DMAQQ and 1-Mes in different solvents. The calculated energies were obtained from equation 4.22 with the inclusion of ZPVE. The function $f(x) = x$ is plotted in dashed lines for visual comparison between the data.

In order to definitively validate the calculations performed this far, we must be able to accurately reproduce the experimentally observed fluorescence energies for these molecules. Using equation 4.22, we calculate the expected fluorescence energy for all three test molecules. That process was twofold: first set of values were obtained using the optimized geometry of each molecule and performing the two-step TD-DFT on that to obtain ΔE_{i0}^{vac}, χ_i, γ_i and γ_0 and then calculate ΔE_{i0}^{emi}; the second approach consisted on using ensembles of all three molecules — instead of the single optimized geometry — from which we obtain values for the aforementioned parameters and the corresponding calculated emission energy for each geometrical conformation in the ensemble, that are then averaged over the vibrational manifold. Figure 4.9 presents this data in a plot where the the y-axis is the experimental energies while the x-axis corresponds to our calculated values for the optimized geometry (a) and the ensemble (b), the dashed lines represent the $y = x$ function, i.e. the functional in which the calculated energy perfectly matches the experimental one. The closer the data points are to the dashed line, the more accurate the theoretical result is. Numerical data can be found in Table 4.2. We also calculate the shift between experimental and calculated results for all cases. For DCM2, the shift between E_{calc}^{opt} and E_{exp} has an absolute average of 0.08 eV, while its ensemble has a corresponding absolute average of 0.11 eV. With more data points available for DMAQQ, the absolute average of the shifts are of 0.05 eV and 0.07 eV, respectively. Those results point to the accuracy of the modeling of DCM2 and DMAQQ. A slightly higher variation on ensemble shifts is expected, considering the possibility that a part of those geometries may possibly lead to excitations of slightly different character, specially in terms of CT strength.

The results from 1-Mes, on the other hand, take us back to the difficulty in appropriately performing electronic structure calculations of that molecule. The energy shift for optimized geometry results show an absolute average of 0.10 eV, which, although slightly higher than that of DCM2 and DMAQQ, still shows a good agreement. It is worth noting that we see a bigger shift in for solvents of lower polarity, such as the four blue squares of higher energy on the left hand side plot, which have individual shifts of up to 0.28 eV. However, for 1-Mes, when we employ an ensemble of 500 geometrical conformations, it seems that the generation of geometries is dominated conformations that present a considerably weaker CT state, leading to the calculated energies being much higher than what was observed experimentally. That problem can be attributed to the inherent nature of the molecule's geometry to be much more sensitive to functional choice than the other two test compounds. To avoid that limitation, we only use the optimized geometry, from which the spectra can be extrapolated by a single gaussian curve with the appropriate width, following equation 2.3 with only one term of the sum being non-null. That brings the absolute average of the shifts down to 0.10 eV, even if the calculated energies for some solvents varied. Thus, Figure 4.9-b shows the comparison between experimental energies and calculated ones from ensembles of 500 conformations for DCM2 and DMAQQ, as well as from the optimized geometry for 1-Mes.

Molecule	Solvent	ε	n	$E_{exp}(eV)$	E_{calc}^{opt} (eV)	E_{calc}^{ens} (eV)
DCM2	Benzene	2.27	1.49	2.19	2.38	2.27
	Chloroform	4.81	1.44	2.08	2.12	2.00
	Ethanol	24.3	1.36	1.92	1.86	1.74
	DMSO	46.7	1.47	1.84	1.85	1.74
DMAQQ	Toluene	2.38	1.49	2.59	2.76	2.66
	Chloroform	4.81	1.45	2.45	2.52	2.44
	EA	6.05	1.37	2.43	2.44	2.37
	THF	7.58	1.41	2.42	2.40	2.34
	Acetone	20.7	1.36	2.33	2.26	2.21
	MeCN	35.7	1.34	2.28	2.22	2.17
	DMF	36.7	1.43	2.27	2.24	2.19
	DMSO	46.7	1.48	2.22	2.25	2.20
1-Mes*	CyH	2.02	1.43	2.82	2.88	2.85
	Diox	2.21	1.42	2.56	2.83	2.83
	Toluene	2.38	1.50	2.68	2.82	2.82
	Chloroform	4.81	1.45	2.25	2.48	2.48
	EtOAc	6.25	1.37	2.30	2.33	2.33
	THF	7.43	1.41	2.28	2.28	2.29
	Acetone	20.5	1.36	2.08	2.04	2.05
	DMF	37.2	1.43	2.01	2.02	2.03

Table 4.2: List of experimental, calculated from optimized geometry and calculated from ensemble energies. *1-Mes ensemble consisted of a single molecular conformation.

4.6 Results B - Estimating dielectric constants through the empirical determination of χ_i and ΔE_{i0}^{vac}

In this section, we show the results of the use of the procedure detailed in section 4.3 for DCM2, 1-Mes and LDs-Red, presented earlier in this chapter. The experimental work of ref. 98 investigated the fluorescence DCM2 in different solvents of varying polarity — benzene, chloroform, ethanol and DMSO — as well as that of aluminum tris(8-hydroxyquinoline) (AlQ_3) films doped with DCM2, that display a large redshift with an increase in DCM2 concentration, which was attributed to the solvatochromic and, the previously mentioned, self-polarizing nature of DCM2. The same effect has also been seen in polystyrene and camphoric anhydride (PS:CA) films, with emission energies varying up to 0.3 eV in a 25% DCM2 concentration[99]. In the same work, the authors calculate the dielectric constants and refractive indexes of the PS:CA:DCM2 films in their different dopant concentrations at 1MHz. Additionally, riarylboranes (TABs) like 1-Mes have shown promise in fluorescence modulation along other photophysical properties through Lewis acid-base interactions combined with the addition of different solvents in order to enhance or reduce the CT character of the excited state of said molecule[100]. In their work, fluorescence is measured in eight different solvents with varying polarities and in four different solid matrices — PS, PMMA, Zeonex and CBP —, which provides us with plenty of data to extract the parameters we are interested in. Lastly, LDs-Red was used to perform spectral scan imaging to visualize the cells' behavior in eight different cellular environments, cancerous and not[101]. In addition, fluorescence spectra were obtained in seven different solvents.

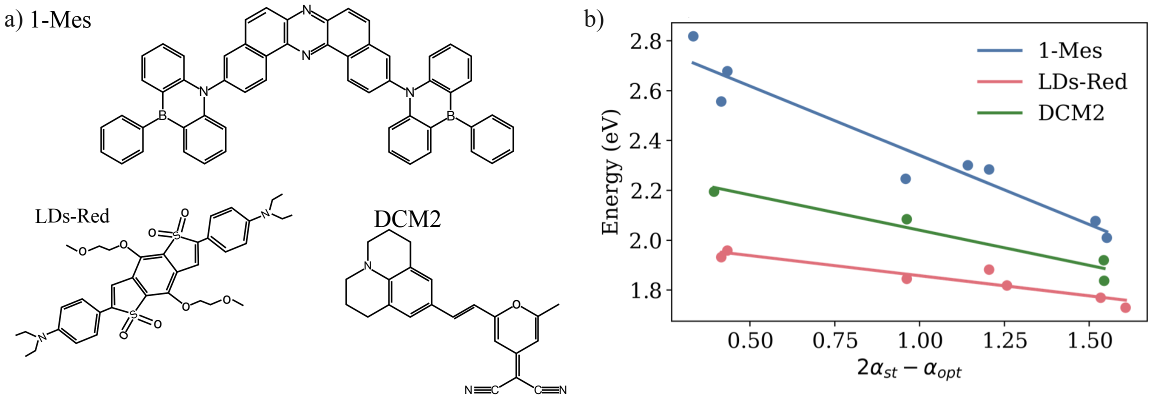

Figure 4.10: a) Test molecules used in this work: 1-Mes, LDs-Red and DCM2. b) Experimental fluorescence peaks for DCM2, 1-Mes and LDs-Red obtained for various solvents as a function of $2\alpha_{st} - \alpha_{opt}$. Lines correspond to fits to Equation 4.39. Experimental data was extracted from refs 99, 100 and 101, respectively.

With the data in hand, Figure 4.10-b shows that experimental fluorescence peaks measured with different solvents of known polarity follow indeed this linear relationship. The plot is made by the spec2epsilon software. The vacuum emission energy (ΔE_{emi}^{vac}) and the susceptibility (χ) extracted by fitting the data to Equation 4.39 are shown in Table 4.3 for our three test molecules and provide a full characterization of the emission energy dependence on medium polarity of each molecule. A look into the actual values also provides some physical insight. Among the three molecules, 1-Mes has the S_1 state of strongest CT character, as evidenced by the highest susceptibility χ of 0.56 eV, followed by DCM2 with 0.28 eV. LDs-Red has the lowest susceptibility at only 0.16 eV. The associated error in this case is simply the error propagation from the linear fit, which provides us with the correlation matrix M, needed for the next steps, as per section 4.3. Higher χ values make for more sensitive polarity probes. This can be seen in the plot where the blue data goes from energies at around 2.8 eV to under 2.2 eV, while LDs-Red and DCM2, shown in red and green, respectively, only vary around 0.2 eV. In fact, since $\Delta E_{emi}^{sol} > 0$, the maximum susceptibility is given by $Max(\chi) = \Delta E_{emi}^{vac}/2$ (when $\alpha_{opt} = 0$), which suggests that more sensitive probes will be found among donor-acceptor molecules with vacuum emission energies near the blue region of the spectrum. This is the case, for instance, of the 1-Mes molecule.

Comparatively with the values of ΔE_{vac}^{opt} and χ^{opt} values obtained through the optimized geometry TD-DFT calculations for DCM2 and 1-Mes shown in Table 4.1, we see that for both cases the calculated values are systematically higher. We can attribute this to several factors. First, the TD-DFT calculations are of vertical energies, while the energies we use for the linear fit are thermally averaged values over experimental measurements. Second, excited states of CT characters are inherently difficult to model, due to the necessity of state-specific perturbative approaches when performing calculations and, even then, no functional in DFT is the perfect functional and calculations may produce varying results. Qualitatively, the tendency is preserved with 1-Mes having a higher vacuum emission energy and presenting itself to be the most polarity sensitive probe of the listed molecules listed.

Molecule	ΔE_{emi}^{vac} (eV)	χ (eV)
LDs-Red	2.02 ± 0.03	0.16 ± 0.03
DCM2	2.32 ± 0.06	0.28 ± 0.05
1-Mes	2.90 ± 0.07	0.56 ± 0.07

Table 4.3: Vacuum emission energies (ΔE_{emi}^{vac}) and solvent susceptibilities (χ) for DCM2, LDs-Red and 1-Mes obtained from fits to Equation 4.39 shown in Figure 4.10-b.

There are limitations to the approach that need to be addressed. First, since our expression accounts only for electrostatic effects, measurements in protic solvents should not be included in the characterization as they may skew results. Protic solvents are those that can donate a hydrogen bond because they contain at least one hydrogen atom covalently bonded to F, O or N. They are often of high polarity and have the ability to stabilize ions or polar molecules both by H-bond and electrostatic interactions. The possible skewness of results comes exactly from the other possible interactions characteristic to these compounds. Classical examples of protic solvents include water, ethanol, methanol, acetic acid. Additionally, deviations from linear behavior may also result from significant changes in equilibrium geometry as ε increases or from reordering of excited states — which we have shown to be a possibility in the previous section with the faulty 1-Mes geometry as an example. This points to a simple plot like this one being, at the very least, a reasonable diagnostic tool of the possibility of other solvent-related phenomena occurring.

Once the vacuum emission energies and solvent susceptibilities have been obtained, we may use this information to infer the static dielectric constant from fluorescence spectra collected under several conditions by following the procedures described in section 4.3. The aforementioned measurements of ε and n of $DCM2$ doped AlQ_3 films[99] — data shown in Table 4.4 — were performed capacitively and the experimental line of the best fit of ε as a function of CA concentration is shown in Figure 4.11-a in red. We took the emission peaks reported for these films and applying our inference procedure with a refractive index of $n = 1.55$[99], we are able to reproduce the same dependence of ε and CA concentration (shown in blue in Figure 4.11-a), effectively using the DCM2 emission as a measuring tool for the static dielectric constant of the different thin films. The uncertainties displayed on the same plot increase with ε. This stems from,

$$\frac{d\alpha_{st}}{d(\Delta E_{emi})} = \frac{d\alpha_{st}}{d\varepsilon}\frac{d\varepsilon}{d(\Delta E_{emi})} \tag{4.46}$$

$$\frac{-1}{2\chi} = \frac{2}{(\varepsilon+1)^2}\frac{d\varepsilon}{d(\Delta E_{emi})} \tag{4.47}$$

$$\Rightarrow \frac{d\varepsilon}{d(\Delta E_{emi})} = \frac{-(\varepsilon+1)^2}{4\chi}. \tag{4.48}$$

Thus, low uncertainty in measurements in highly polar media requires probes with large solvent susceptibility, which is not the case for DCM2. Such uncertainty can also be reduced by improving the characterization of the probe, i.e. by performing the fluorescence measurements in a large ensemble of

Molecule	Solvent/Concentration	ε	n	Fluorescence (eV)
DCM2	Benzene	2.270	1.4967	2.194
	Chloroform	4.810	1.4458	2.084
	Ethanol	24.30	1.3611	1.919
	DMSO	46.70	1.4783	1.837
	C0.0%	-	1.5500	2.204
	C3.5%	-	1.5500	2.154
	C7.0%	-	1.5500	2.128
	C10.5%	-	1.5500	2.097
	C14.0%	-	1.5500	2.080
	C17.5%	-	1.5500	2.060
	C21.0%	-	1.5500	2.050
	C24.5%	-	1.5500	2.040

Table 4.4: Experimental emission energies for DCM2 in different solvents and as a dopant in AlQ_3 films in different concentrations.[99]

solvents, providing more data points for the fit, which, in turn, improves the values of ΔE_{emi}^{vac} and χ.

Moving on to our second test molecule, 1-Mes, with applications related to OLEDs. We have access to experimental data on its fluorescence when measured in solution for several solvents, as well as for when doped in films with different matrix molecules, including Zeonex, PS, CBP (4,4′-Bis(N-carbazolyl)-1,1′-biphenyl) and PMMA. Table 4.5 shows the results of those measurements. Applying our inference procedure to these data, we can extract the ε values corresponding to these different films. Figure 4.11-b shows the results assuming again a refractive index of $n = 1.55$. The inferred dielectric constants for Zeonex and PS match closely their experimental benchmark values for neat films. On the other hand, predictions for CBP and PMMA show greater disparity, with our methodology indicating higher polarity than expected from just the neat films of the matrices used. This implies that the emission energy in these films is lower than the expected based solely on the polarity of the matrix. In order to understand these discrepancies, one can see that the concentration of the probe molecule in the different experiments vary considerably, going from 1.0 wt% and 1.1 wt% in Zeonex and PS to 10.0 wt% in CBP and 6.4 wt% in PMMA. Thus, it stands to reason that in the latter two samples, other effects besides dielectric ones are probably affecting emission. Considering the higher concentration, the most likely explanation would be that of aggregation effects. This highlights two important points. First, when using the approach described here to directly measure static dielectric constants, the concentration of the

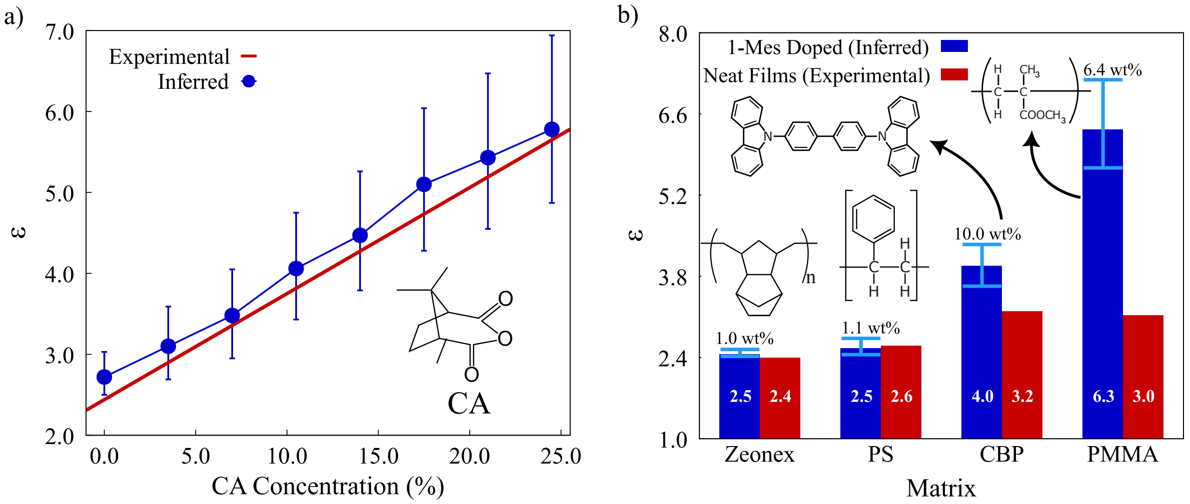

Figure 4.11: a) Dielectric constants of PS:CA films doped with DCM2 measured capacitively99, (red line) and inferred from fluorescence data (this work, blue). b) Dielectric constants of organic thin-films composed of different matrices — Zeonex[114], PS[**?**], CBP[115] and PMMA[116] — doped with 1-Mes inferred from emission energies (blue) are compared with known dielectric constants of the corresponding neat films (red). Dopant concentrations are shown for each film.

probe molecule needs to be kept low enough to prevent it from affecting the measurement itself. The second point is that, if the polarity of the matrix is already known, such as in the case of the 1-Mes films from refs. 100 and 117, our methodology provides a simple diagnostic tool to determine whether non-dielectric effects are affecting the emission properties of the molecule.

Lastly, we consider the bioimaging application of LDs-Red and its data extracted from ref. 101. Authors observe that the droplets in cancerous cells have typically lower polarity, and quantify the effect in terms of the polarity index ET(30)[61]. Said index comes from one single solvatochromic probe, Reichardt's dye, only reflecting how that dye interacts with the solvent, often not generalizing the phenomenon to other molecules as easily. It also mixes electrostatic interactions with specific solute-solvent interactions, such as hydrogen bonding. Table 4.6 shows the fluorescence energy peaks measured in these cells and the corresponding dielectric constant extracted by our method (assuming $n = 1.47$[118]) along with the uncertainty interval. These results provide an improved characterization compared to the ET(30) polarity index, by offering instead the actual dielectric constant with a quantified uncertainty. Knowing ε itself can be quite advantageous because it directly enters electrostatic solvation models, making it a more fundamental and transferable descriptor for fluorescence-based solvent studies.

Molecule	Solvent/Concentration	ε	n	Fluorescence (eV)
1-Mes	CyH	2.016	1.4262	1.958
	Toluene	2.380	1.4969	1.931
	1,4-dioxane	2.209	1.4224	1.881
	EtOAc	6.253	1.3724	1.769
	THF	7.580	1.4072	1.845
	$CHCl_3$	4.910	1.4458	1.818
	Acetone	20.70	1.3586	1.729
	DMF	37.22	1.4305	1.729
	PS	-	1.5500	2.666
	PMMA	-	1.5500	2.317
	Zeonex	-	1.5500	2.761
	CBP	-	1.5500	2.460

Table 4.5: Experimental emission energies for 1-Mes in different solvents and doped solid matrices.[100]

Cell type	Cells	ΔE_{emi}^{exp} (eV)[101]	ε	Interval
Cancerous	HepG2	1.99	2.26	[2.19,2.38]
	HepG2*	1.99	2.27	[2.19,2.41]
	Panc02	1.98	2.28	[2.20,2.42]
	HeLa	1.98	2.29	[2.19,2.47]
	U251	1.95	2.56	[2.30,2.87]
Normal	L929	1.94	2.55	[2.30,2.86]
	Ht22	1.94	2.60	[2.33,2.94]

Table 4.6: Dielectric constants (ε) estimated from LDs-Red fluorescence peaks measured in different cellular environments[101]. Interval corresponds to 16th and 84th percentiles.

CHAPTER 5

CONCLUSIONS

This work set out to better understand the physical mechanisms behind the up-conversion of triplet excitons into singlet excitons, particularly in the context of persistent luminescence and environment-dependent photophysics. By combining ab-initio electronic structure calculations, ensemble based simulated spectroscopy and kinetic Monte Carlo dynamics, we developed a coherent picture that spans two connected domains: (i) the photophysics of the NPB/DCJTB hostguest system, where triplet-to-singlet Förster transfers emerge as an efficient triplet harvesting channel as well as an uncommon pathway to afterglow; and (ii) the quantitative description of solvent- and environment-induced polarization effects in donor-acceptor fluorophores, from which the dielectric constant of solid state mediums can be inferred directly from in-solution spectral data. Together, Chapters 3 and 4 demonstrate how microscopic exciton dynamics and macroscopic environmental polarization can be intertwined in determining the fate of excited states in molecular materials.

In Chapter 3, the photophysical characterization of NPB and DCJTB revealed the internal logic of the observed afterglow in NPB/DCJTB films. Through nuclear ensemble simulations accounting for vibrational and medium effects, we obtained fluorescence, phosphorescence, intersystem crossing (ISC), reverse intersystem crossing (rISC), and nonradiative decay rates for both molecules. The results showed that NPB exhibits very large ISC rates ($\approx 10^8$ s^{-1}) compared to its fluorescence rate, while its rISC and nonradiative triplet deactivation channels — which are the most common sources of afterglow — are negligible. This specific balance along with NPB being an excellent dual emitter make it a natural Förster donor for TTS transfers. DCJTB, on the other hand, displays comparable fluorescence and ISC rates, but its triplet excitons suffer from rapid nonradiative decay, suppressing any internal triplet recycling. The combination of these contrasting properties gives rise to the TTS mechanism as a viable route for triplet harvesting in the composite system. Calculated Förster radii confirmed that TTS transfer from NPB(T_1) $\rightarrow$ DCJTB(S_1) is energetically and spectroscopically allowed, with an average value of about 32 Å— well within experimental uncertainty. KMC simulations parameterized with these rates showed that, in the absence of rISC, TTS becomes the dominant conversion pathway competing directly with phosphorescence in NPB. At low DCJTB concentrations (0.2 wt%), the probability of a triplet exciton in NPB undergoing TTS versus phosphorescence is roughly 47 % to 53 %; at higher concentrations, this efficiency nearly doubles. The delayed fluorescence observed experimentally therefore originates not from phosphorescence, but from singlet emission in DCJTB molecules populated via TTS transfers. The simulated afterglow occurs in the sub-second regime —consistent with experimental observations — confirming that TTS-derived fluorescence can account for persistent luminescence in this system.

An equally important aspect uncovered in Chapter 3 concerns morphology and dielectric effects. Increasing DCJTB concentration not only alters intermolecular distances, therefore modulating Förster rates, but also increases the effective dielectric constant of the composite, producing a self-polarizing environment. This finding bridges into the subject of Chapter 4, where the inclusion of previously neglected corrections pave the way for more detailed descriptions. There, we moved from solid-state host-guest films to the broader question of how medium polarity influences electronic excitation energies. Building upon the perturbative, state-specific solvation model introduced earlier, we redefined the solvation energy in terms of a molecular susceptibility χ, which captures both equilibrium and non-equilibrium solvation regimes. Through extensive electronic-structure calculations across several donor-acceptor fluorophores — including DCJTB, DMAQQ, DCM2, and 1-Mes — we demonstrated that χ serves as a quantitative fingerprint of charge-transfer character of an excited state. Molecules with strong CT states display higher χ values and correspondingly stronger solvatochromism.

By comparing vacuum and solvation emission energies, we showed that the relationship between ΔE_{vac} and χ can be inverted to infer the dielectric constant of the medium directly from fluorescence data, without resorting to empirical polarity scales such as ET(30). This establishes a bridge between molecular-level electronic response and measurable macroscopic parameters. The proposed approach outperforms traditional models such as Lippert-Mataga, which assume a linear and isotropic dielectric cavity, by explicitly treating the mutual polarization between solute and solvent and distinguishing equilibrium from non-equilibrium solvation. The success of this model demonstrates that solvent susceptibility provides a more physically grounded descriptor of environmental effects on emission energies, unifying theoretical predictions and experimental spectra under a single quantitative framework. Taken together, the two chapters portray parts of a solution of a broader problem. The first reveals how local dielectric environment and intermolecular interactions govern exciton fate in a host-guest matrix, while the second formalizes the same physical principle — environmental polarization — into a transferable model applicable to any solvatochromic system. Both studies emphasize that energy transfer and conversion in organic materials cannot be dissociated from the polarizability of their surroundings. The self-consistent feedback between exciton formation, molecular dipoles, and environmental response dictates whether energy is radiatively emitted, harvested through TTS, or dissipated non-radiatively.

Beyond their immediate results, these investigations leave behind a methodological toolkit. The combination of non-empirically tuned range-separated functionals, ensemble-based spectroscopy, and solvent-susceptibility analysis provides a robust route to study excited-state processes across different chemical environments. The KMC framework developed for NPB/DCJTB has been generalized by co-authors L. Evaristo and T. Araujo[119] and can be used for other donor-acceptor pairs, enabling predictive modeling of persistent luminescent materials. Similarly, the solvent-susceptibility approach opens the door to linking fluorescence spectroscopy and dielectric properties in complex media, from solid matrices to biological systems. In conclusion, the thesis establishes a unified understanding of exciton dynamics and solvent response across distinct yet connected domains. The NPB/DCJTB system exemplifies how triplet excitons, often regarded as loss channels, can be harvested through intermolecular interactions to produce long-lived fluorescence. The solvent-susceptibility formalism, in turn, extends the same conceptual language to describe how a molecule's environment governs its optical response. Together, these contributions advance the theoretical basis for designing and characterizing new materials capable of exploiting triplet energy, tuning emission via environmental polarity, and ultimately improving the efficiency and functionality of next-generation optoelectronic and sensing devices.

CHAPTER 6

APPENDIX A

Many-body problem

In the context of a molecular compound, the many-body problem is often identified. Let us consider a molecular system with N electrons and M nuclei, indexed by $\{i, j, ...\}$ and $\{A, B, ...\}$, respectively. Our system is shown in figure 6.1, in which $\vec{r}_i$ is the position vector for the ith electron, $\vec{r}_{ij}$ is the distance between the ith and the jth electron, $\vec{R}_A$ is the position vector for the Ath nucleus, $\vec{R}_{AB}$ is the distance between the Ath and Bth nuclei and $\vec{R}_{Ai}$ is the distance between the Ath nucleus and the ith electron. Schrödinger's non-relativistic time-independent equation is

$$\hat{H}\Psi = E^T\Psi \tag{6.1}$$

where $\hat{H}$ is the Hamiltonian operator and E^T is the eigenvalue for the system's total energy. Taking into account that the nuclei are positively charged, we can express the Hamiltonian as

$$\hat{H} = \hat{T}_n + \hat{T}_e + \hat{V}_{ee} + \hat{V}_{nn} + \hat{V}_{en} \tag{6.2}$$

with $\hat{T}_n$ and $\hat{T}_e$ being the kinetic energy operators for the nuclei and for the electrons, respectively. In addition, $\hat{V}_{nn}$ is the operator for the interaction between nuclei, $\hat{V}_{ee}$ accounts for the interaction between electrons and $\hat{V}_{en}$ considers the interaction energy between electrons and nuclei.

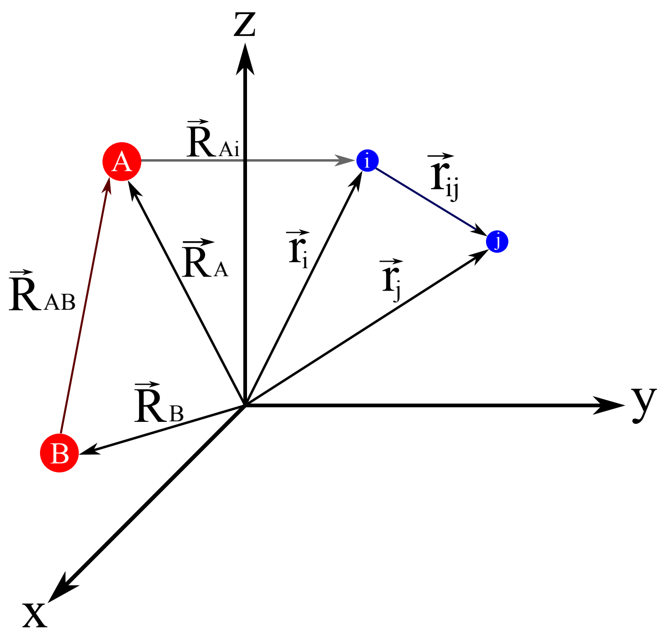

Figure 6.1: Schematic representation of the many-body problem for N electrons (i,j,...) and M nuclei (A,B,...).

We define the kinetic energy operator $\hat{T}$ in terms of the linear momentum operator $\hat{P}$,

$$\hat{T} = \frac{\hat{P}^2}{2m} \tag{6.3}$$

which is, in turn, defined by $\hat{P} = -i\hbar\vec{\nabla}$ when projected into the three dimensional position space. Thus,

$$\hat{T} = \frac{(-i\hbar\vec{\nabla})\cdot(-i\hbar\vec{\nabla})}{2m} = -\frac{\hbar^2\nabla^2}{2m}. \tag{6.4}$$

Considering a purely Coulombic interaction between charges, the remaining operators are, in atomic units ($\hbar = m_e = e = k_e = 1$), expressed by

$$\hat{T}_n = -\frac{\hbar^2}{2}\sum_{A=1}^{M}\frac{\nabla_A^2}{m_A} = -\frac{1}{2}\sum_{A=1}^{M}\frac{\nabla_A^2}{m_A} \tag{6.5}$$

$$\hat{T}_e = -\frac{\hbar^2}{2m_e}\sum_{i=1}^{N}\nabla_e^2 = -\frac{1}{2}\sum_{i=1}^{N}\nabla_e^2 \tag{6.6}$$

$$\hat{V}_{ee} = \sum_{i=1}^{N}\sum_{j>i}^{N}k_e\frac{e^2}{r_{ij}} = \sum_{i=1}^{N}\sum_{j>i}^{N}\frac{1}{r_{ij}} \tag{6.7}$$

$$\hat{V}_{nn} = \sum_{A=1}^{M}\sum_{B>A}^{M} k_e \frac{(Z_A e)(Z_B e)}{R_{AB}} = \sum_{A=1}^{M}\sum_{B>A}^{M} \frac{Z_A Z_B}{R_{AB}} \tag{6.8}$$

$$\hat{V}_{en} = -\sum_{A=1}^{M}\sum_{i=1}^{N} k_e \frac{Z_A e^2}{R_{Ai}} = -\sum_{A=1}^{M}\sum_{i=1}^{N} \frac{Z_A}{R_{Ai}} \tag{6.9}$$

where we have already eliminated twice accounted interactions with the second sum in (6.7) and (6.8). The eigenfunction Ψ depends on the position sets for all electrons, $\{\vec{r}\}$, and nuclei $\{\vec{R}\}$,

$$\hat{H}\Psi(\{\vec{r}\};\{\vec{R}\}) = E^T \Psi(\{\vec{r}\};\{\vec{R}\}). \tag{6.10}$$

Hence, writing the Hamiltonian (6.1) becomes,

$$-\frac{1}{2}\sum_{A=1}^{M}\frac{\nabla_A^2}{m_A}\Psi + -\frac{1}{2}\sum_{i=1}^{N}\nabla_e^2\Psi + \sum_{i=1}^{N}\sum_{j>i}^{N}\frac{1}{r_{ij}}\Psi + \sum_{A=1}^{M}\sum_{B>A}^{M}\frac{Z_A Z_B}{R_{AB}}\Psi - \sum_{A=1}^{M}\sum_{i=1}^{N}\frac{Z_A}{R_{Ai}}\Psi = E^T\Psi. \tag{6.11}$$

Born-Oppenheimer approximation

Note that (6.11) is a differential equation that can only be solved using approximations. The first approximation to be done is to take advantage of separation of variables in Ψ, such as

$$\Psi(\{\vec{r}\};\{\vec{R}\}) = \psi_e(\{\vec{r}\};\{\vec{R}\})\chi_n(\{\vec{R}\}) \tag{6.12}$$

in which ψ_e is related to electron movement and χ_n accounts for nuclei movement. However, ψ_e is parametrically dependent on $\{\vec{R}\}$, that is, comparatively to $\{\vec{r}\}$, $\{\vec{R}\}$ is seen as a constant. This particular choice of variable separation reflects the *adiabatic approximation* for nuclei movement, where due to the considerable difference between electron masses and nuclei masses, one can assume that during the time it takes for an electron to move, the nucleus remains still. To summarize, this means that for obtaining the eigenfunction $\psi_e(\{\vec{r}\};\{\vec{R}\})$ we have to consider that there is no movement for the nuclei.

The Born-Oppenheimer approximation is based on employing the *adiabatic approximation* in $\hat{T}_n$ applied to Ψ, like so,

$$\hat{T}_n\Psi = -\frac{1}{2}\sum_{A=1}^{M}\frac{\nabla_A^2}{m_A}[\psi_e(\{\vec{r}\};\{\vec{R}\})\chi_n(\{\vec{R}\})] \tag{6.13}$$

where the Laplace operator application stays as

$$\begin{aligned}\nabla_A^2[\psi_e(\{\vec{r}\};\{\vec{R}\})\chi_n(\{\vec{R}\})] &= \vec{\nabla}_A\cdot[\vec{\nabla}(\psi_e\chi_n)]\\ &= \vec{\nabla}_A\cdot(\chi_n\vec{\nabla}_A\psi_e+\psi_e\vec{\nabla}_A\chi_n)\\ &= \chi_n\nabla_A^2\psi_e+\psi_e\nabla_A^2\chi_n+2\vec{\nabla}_A\chi_n\vec{\nabla}_A\psi_e\end{aligned} \tag{6.14}$$

in which, following the aforementioned parametric dependence of ψ_e with $\{\vec{R}\}$, the terms $\vec{\nabla}_A\psi_e$ and $\nabla_A^2\psi_e$ are null. Hence,

$$\hat{T}_n\Psi = -\frac{\psi_e}{2}\sum_{A=1}^{M}\frac{\nabla_A^2\chi_n}{m_A} \tag{6.15}$$

such that, using that in (6.11) and dividing the equation for $\psi_e\chi_n$, we conclude

$$-\frac{1}{2}\sum_{A=1}^{M}\frac{1}{\chi_n}\frac{\nabla_A^2\chi_n}{m_A}-\frac{1}{2}\sum_{i=1}^{N}\frac{\nabla_e^2\psi_e}{\psi_e}+\sum_{i=1}^{N}\sum_{j>i}^{N}\frac{1}{r_{ij}}+\sum_{A=1}^{M}\sum_{B>A}^{M}\frac{Z_AZ_B}{R_{AB}}-\sum_{A=1}^{M}\sum_{i=1}^{N}\frac{Z_A}{R_{Ai}}=E^T. \tag{6.16}$$

Choosing $-\varepsilon$ as our separation constant, we can obtain the Electronic Schrödinger equation,

$$\boxed{-\frac{1}{2}\sum_{i=1}^{N}\nabla_e^2\psi_e+\sum_{i=1}^{N}\sum_{j>i}^{N}\frac{\psi_e}{r_{ij}}-\sum_{A=1}^{M}\sum_{i=1}^{N}\frac{Z_A}{R_{Ai}}\psi_e+\sum_{A=1}^{M}\sum_{B>A}^{M}\frac{Z_AZ_B}{R_{AB}}\psi_e=\varepsilon\psi_e} \tag{6.17}$$

where $\varepsilon=\varepsilon(\{\vec{R}\})$, and the Nuclear Schödinger equation,

$$\boxed{-\frac{1}{2}\sum_{A=1}^{M}\frac{\nabla_A^2\chi_n}{m_A}+\varepsilon(\{\vec{R}\})\chi_n=E^T\chi_n}. \tag{6.18}$$

Through the adiabatic approximation, we can understand that for each specific nuclear geometric configuration (or that for each parametric $\{\vec{R}\}$ in (6.17)), we obtain a particular solution for (6.17). Multiple solutions form the potential energy surface for different inter nuclear distances, or simply put, to different molecular geometric conformations.

CHAPTER 7

APPENDIX B

7.1 Density Functional Theory

In the fundamental basis of solving the many-body problem in a molecular context, one may take into consideration the Hartree-Fock picture. At its core is the use of the variational method considering that the wave function can be represented by a single Slater determinant. Nevertheless, dealing with the wave function is not a simple task. The idea of working with a more suitable quantity instead of the wave function itself gave way to massive developments in computational quantum mechanics and chemistry.

As our starting point, let's take the electronic Hamiltonian operator obtained from the Born-Oppenheimer approximation,

$$\hat{H}_{ele} = \hat{T}_e + \hat{V}_{en} + \hat{V}_{ee} \tag{7.1}$$

$$\hat{H}_{ele} = -\sum_{i=1}^{N} \nabla_i^2 - \sum_{i=1}^{N}\sum_{A=1}^{M} \frac{Z_A}{r_{iA}} + \sum_{i=1}^{N}\sum_{j\neq i}^{N} \frac{1}{r_{ij}} \tag{7.2}$$

where $\hat{T}_e$ is the kinetic energy operator for electrons, $\hat{V}_{en}$ is the potential interaction between the i-th electron and the A-th nucleus and $\hat{V}_{ee}$ is the attraction potential due to the interaction between two electrons. We can rewrite the Hamiltonian in terms of the sum of one-electron and two-electron operators, such as,

$$\hat{H}_{ele} = \hat{O}_1 + \hat{O}_2 = \sum_{i=1}^{N} \left(T(i) + \vartheta(i)\right) + \sum_{i=1}^{N}\sum_{j\neq i}^{N} \frac{1}{r_{ij}} \tag{7.3}$$

in which,

$$\vartheta(i) = -\sum_{A=1}^{M} \frac{Z_A}{r_{iA}} \tag{7.4}$$

Notice that such Hamiltonian depends only on the positions and atomic numbers of the nuclei and the total number of electrons. Such dependence suggests the electron density ρ as an observable we can investigate in practical terms without necessarily having to learn the form of the wave function. When integrated over all space, the electron density gives the total number of electrons,

$$N = \int \rho(\vec{r})d\vec{r}. \tag{7.5}$$

For a known wave function ψ, that is, a solution to $\hat{H}_{ele}$, the energy can be expressed as a functional of ψ, such as

$$E[\psi] = \langle\psi|\hat{H}_{ele}|\psi\rangle = \langle\psi|\hat{O}_1 + \hat{O}_2|\psi\rangle \tag{7.6}$$

In the following steps, we will detail the mathematical tools needed to prove the anchoring theorems of Density Functional Theory. From Mechanical Statistics, the density operator of a system is defined as,

$$\gamma = \sum_k |k\rangle\langle k| \tag{7.7}$$

where k indexes all the possible states in which the system can be found. In our case, if ψ is the complete solution for $\hat{H}_{ele}$, it is also the only possible state, which means the density operator can be written as

$$\gamma = |\psi\rangle\langle\psi| \tag{7.8}$$

Using that definition, one can build its matrix element,

$$\begin{aligned}\gamma(\vec{x}_1,\vec{x}'_1,\vec{x}_2,\vec{x}'_2,...,\vec{x}_N,\vec{x}'_N) &= \langle\vec{x}'_1,\vec{x}'_2,...,\vec{x}'_N||\psi\rangle\langle\psi||\vec{x}_1,\vec{x}_2,...,\vec{x}_N\rangle &(7.9)\\ &= \psi(\vec{x}'_1,\vec{x}'_2,...,\vec{x}'_N)\psi^*(\vec{x}_1,\vec{x}_2,...,\vec{x}_N) &(7.10)\end{aligned}$$

where if $\vec{x}_i = \vec{x'_i}$, then

$$\gamma = |\psi(\vec{x}_1,\vec{x}_2,...,\vec{x}_N)|^2 \tag{7.11}$$

recovering the idea of the probability density.

Considering the intrinsic properties of a non-local operator, we can project γ into elements that are not from the same vector space ($\vec{x}_i \neq \vec{x}'_i$). Knowing that i indexes different particles, we can assume the first k particles are not in the density operator's space and integrate over all particles in that space but the first k in γ's space, such as,

$$\gamma_k(\vec{x}'_1,\vec{x}'_2,..,\vec{x}'_k,\vec{x}_1,\vec{x}_2,...,\vec{x}_k) = \binom{N}{k} \int d\vec{x}_{k+1}d\vec{x}_{k+2}...d\vec{x}_N\, \psi(\vec{x}'_1,\vec{x}'_2,..,\vec{x}'_k,\vec{x}_{k+1},\vec{x}_{k+2},...,\vec{x}_N)\times$$

$$\psi^*(\vec{x}_1,\vec{x}_2,..,\vec{x}_k,\vec{x}_{k+1},\vec{x}_{k+2},...,\vec{x}_N) \quad (7.12)$$

This particular integration defines the reduced density operator's matrix element to k-th order. For our focus in Density Functional Theory, we are only interested in $k = 1$ and $k = 2$. Reducing it to the first order ($k = 1$) yields,

$$\gamma_1(\vec{x}'_1,\vec{x}_1) = \frac{N!}{1!(N-1)!} \int d\vec{x}_2 d\vec{x}_3...d\vec{x}_N\, \psi(\vec{x}'_1,\vec{x}_2,...,\vec{x}_N)\,\psi^*(\vec{x}_1,\vec{x}_2,...,\vec{x}_N) \quad (7.13)$$

which we can integrate over spin obtaining,

$$\int d\omega_1 \gamma_1(\vec{x}'_1,\vec{x}_1) = \rho_1(\vec{r}'_1,\vec{r}_1) \quad (7.14)$$

that, in the case of $\vec{r}'_1 = \vec{r}_1$, turns into the known electron density,

$$\rho_1(\vec{r}_1) = \int d\omega_1 \vec{x}_1,\vec{x}_2,...,\vec{x}_N)\,\psi^*(\vec{x}_1,\vec{x}_2,...,\vec{x}_N) \Longrightarrow N = \int d\vec{r}_1 \rho_1(\vec{r}_1) \quad (7.15)$$

Now for $k = 2$,

$$\gamma_2(\vec{x}'_1,\vec{x}'_2,\vec{x}_1,\vec{x}_2) = \frac{N!}{2!(N-2)!} \int d\vec{x}_3...d\vec{x}_N\, \psi(\vec{x}'_1,\vec{x}'_2,\vec{x}_3...,\vec{x}_N)\,\psi^*(\vec{x}_1,\vec{x}_2,\vec{x}_3,...,\vec{x}_N) \quad (7.16)$$

and, integrating it over the spin coordinate,

$$\int d\omega_1 d\omega_2 \gamma_2(\vec{x}'_1,\vec{x}'_2,\vec{x}_1,\vec{x}_2) = \rho_2(\vec{r}'_1,\vec{r}'_2,\vec{r}_1,\vec{r}_2) \quad (7.17)$$

where for $\vec{r}'_1 = \vec{r}_1$ and $\vec{r}'_2 = \vec{r}_2$ we can obtain $\rho(\vec{r}_1,\vec{r}_2)$. Integrating it,

$$\int d\vec{r}_1 d\vec{r}_2 \rho_2(\vec{r}_1,\vec{r}_2) = \frac{N(N-1)}{2} \quad (7.18)$$

which corresponds exactly to the number of electron pairs. We can associate the one and two-electron operators to ρ_1 and ρ_2, respectively.

The one-electron operator contribution to the energy can be written as

$$\langle\psi|\,\hat{O}_1\,|\psi\rangle = \int d\vec{x}_1 d\vec{x}_2 ... d\vec{x}_N \psi^*(\vec{x}_1,\vec{x}_2,\vec{x}_3,...,\vec{x}_N) \left(\sum_{i=1}^{N} \hat{O}_1(\vec{x}_1)\right) \psi(\vec{x}_1,\vec{x}_2,\vec{x}_3,...,\vec{x}_N) \tag{7.19}$$

$$= N \int d\vec{x}_1 d\vec{x}_2 ... d\vec{x}_N \psi^*(\vec{x}_1,\vec{x}_2,\vec{x}_3,...,\vec{x}_N) \hat{O}_1(\vec{x}_1) \psi(\vec{x}_1,\vec{x}_2,\vec{x}_3,...,\vec{x}_N) \tag{7.20}$$

$$= \int d\vec{x}_1 \hat{O}_1(\vec{x}_1) \gamma_1(\vec{x}'_1,\vec{x}_1)|_{\vec{x}'_1=\vec{x}_1} \tag{7.21}$$

$$= \int d\vec{r}_1 \hat{O}_1(\vec{r}_1) \rho_1(\vec{x}_1) \tag{7.22}$$

$$= \int d\vec{r}_1 \left(-\frac{1}{2}\nabla_i^2 + \vartheta(i)\right) \rho_1(\vec{r}_1). \tag{7.23}$$

Doing a similar procedure on the two-electron operator contribution in the energy, we have

$$\langle\psi|\,\hat{O}_2\,|\psi\rangle = \int d\vec{x}_1 d\vec{x}_2 ... d\vec{x}_N \psi^*(\vec{x}_1,\vec{x}_2,\vec{x}_3,...,\vec{x}_N) \left(\sum_{i=1}^{N} \sum_{j\neq i} \hat{O}_2(\vec{x}_1,\vec{x}_2)\right) \psi(\vec{x}_1,\vec{x}_2,\vec{x}_3,...,\vec{x}_N) \tag{7.24}$$

$$= \frac{N(N-1)}{2} \int d\vec{x}_1 d\vec{x}_2 ... d\vec{x}_N \psi^*(\vec{x}_1,\vec{x}_2,\vec{x}_3,...,\vec{x}_N) \hat{O}_2(\vec{x}_1,\vec{x}_2) \psi(\vec{x}_1,\vec{x}_2,\vec{x}_3,...,\vec{x}_N) \tag{7.25}$$

$$= \int d\vec{x}_1 d\vec{x}_2 \hat{O}_2(\vec{x}_1,\vec{x}_2) \gamma_2(\vec{x}'_1,\vec{x}_1,\vec{x}'_2,\vec{x}_2)|_{\vec{x}'_1=\vec{x}_1;\vec{x}'_2=\vec{x}_2} \tag{7.26}$$

$$= \int d\vec{r}_1 d\vec{r}_2 \hat{O}_2(\vec{x}_1,\vec{x}_2) \rho_2(\vec{r}_1,\vec{r}_2) \tag{7.27}$$

However, by doing this, the energy is not uniquely defined by the electron density. To obtain a more expressive result, we can arrange,

$$\langle\psi|\,\hat{O}_2\,|\psi\rangle = \frac{N(N-1)}{2} \int d\vec{x}_1 \left(\int d\vec{x}_2 \hat{O}_2(\vec{x}_1,\vec{x}_2) d\vec{x}_3 ... d\vec{x}_N \psi^*(\vec{x}_1,\vec{x}_2,\vec{x}_3,...,\vec{x}_N) \psi(\vec{x}_1,\vec{x}_2,\vec{x}_3,...,\vec{x}_N)\right) \tag{7.28}$$

$$= \int d\vec{r}_1 \Theta_2(\vec{r}_1) \rho_1(\vec{r}_1) \tag{7.29}$$

leading to,

$$E[\rho] = \int \left(-\frac{1}{2}\nabla_i^2 + \vartheta(\vec{r}) + \Theta_2(\vec{r})\right) \rho(\vec{r}) \tag{7.30}$$

where have defined,

$$\Theta_2(\vec{r}_1) = \frac{N(N-1)}{2}\int d\omega_1 \left(\int d\vec{x}_2 \hat{O}_2(\vec{x}_1,\vec{x}_2) d\vec{x}_3 ... d\vec{x}_N \psi^*(\vec{x}_1,\vec{x}_2,\vec{x}_3,...,\vec{x}_N)\psi(\vec{x}_1,\vec{x}_2,\vec{x}_3,...,\vec{x}_N)\right) \quad (7.31)$$

From equation (7.30), we can visualize that the energy can be written as a functional of the electron density.

Following the historical steps of the development of theoretical investigation into electronic structure calculations, it is prudent to recover the Hartree-Fock method in order to better understand why DFT is viewed as the more convenient and complete method.

7.1.1 Hartree-Fock with electron density

We can also write the Hartree-Fock wave function in terms of the density operators. In the Hartree-Fock approximation, the wave function for the eletronic Hamiltonian is given by a single Slater's determinant, like so,

$$|\psi_{ele}^{HF}\rangle = \frac{1}{\sqrt{N!}}\sum_i (-1)^{\mathscr{P}_i}\mathscr{P}_i(\chi_1(1)\chi_2(2)...\chi_N(N)) \quad (7.32)$$

$$= |\chi_1(1)\chi_2(2)...\chi_N(N)\rangle . \quad (7.33)$$

Using $|\psi_{ele}^{HF}\rangle$ to define γ_1 and γ_2 yields,

$$\gamma_1(\vec{x}_1,\vec{x}_1') = \sum_i^N \chi_i(\vec{x}_1')\chi_i^*(\vec{x}_1) \quad (7.34)$$

and

$$\gamma_2(\vec{x}_1,\vec{x}_2,\vec{x}_1',\vec{x}_2') = \frac{1}{2}\left(\gamma_1(\vec{x}_1,\vec{x}_1')\gamma_1(\vec{x}_2,\vec{x}_2') - \gamma_1(\vec{x}_2,\vec{x}_1')\gamma_1(\vec{x}_1,\vec{x}_2')\right) \quad (7.35)$$

$$= \frac{1}{2}\begin{vmatrix} \gamma_1(\vec{x}_1,\vec{x}_1') & \gamma_1(\vec{x}_1,\vec{x}_2') \\ \gamma_1(\vec{x}_2,\vec{x}_1') & \gamma_1(\vec{x}_2,\vec{x}_2') \end{vmatrix} \quad (7.36)$$

Now we can determine the energy as functional of the density operator and in terms of the one-electron and two-electron operators,

$$
\begin{aligned}
E_{HF}[\gamma] &= \langle \psi_{ele}^{HF} | \hat{H}_{ele} | \psi_{ele}^{HF} \rangle && (7.37)\\
&= \langle \psi_{ele}^{HF} | \hat{O}_1 | \psi_{ele}^{HF} \rangle + \langle \psi_{ele}^{HF} | \hat{O}_2 | \psi_{ele}^{HF} \rangle && (7.38)\\
&= \int d\vec{x}_1 \hat{O}_1(\vec{x}_1)\gamma(\vec{x}_1,\vec{x}_1')|_{\vec{x}_1=\vec{x}_1'} + \int d\vec{x}_1 d\vec{x}_2 \hat{O}_2(\vec{x}_1',\vec{x}_1,\vec{x}_2',\vec{x}_2)\gamma_2(\vec{x}_1',\vec{x}_1,\vec{x}_2',\vec{x}_2)|_{\vec{x}_1'=\vec{x}_1;\vec{x}_2'=\vec{x}_2} && (7.39)
\end{aligned}
$$

where we can express γ_2 from equation (7.35) to obtain,

$$
\begin{aligned}
E_{HF}[\gamma] = \int d\vec{x}_1 \left(-\frac{1}{2}\nabla_i^2 + \vartheta(\vec{r})\right)\gamma(\vec{x}_1)+ \\
+\int d\vec{x}_1 d\vec{x}_2 \frac{1}{r_{12}}\left(\gamma_1(\vec{x}_1,\vec{x}_1)\gamma_1(\vec{x}_2,\vec{x}_2) - \gamma_1(\vec{x}_2,\vec{x}_1)\gamma_1(\vec{x}_1,\vec{x}_2)\right) \quad (7.40)
\end{aligned}
$$

We are looking for the energy in terms of the electron density, which can be easily obtained by integrating equation (7.40) on the spin coordinate,

$$
E_{HF}[\rho] = \int d\vec{r}_1 \left(-\frac{1}{2}\nabla_i^2 + \vartheta(\vec{r})\right)\rho(\vec{r}_1) + \int d\vec{r}_1 d\vec{r}_2 \frac{1}{r_{12}}\rho_2(\vec{x}_1,\vec{x}_2) \quad (7.41)
$$

However, in equation (7.40), we were able to write γ_2 as a linear combination of different γ_1. We to be able to do the same with the electron density. The proof is simple but extensive and since it has been shown for the density operator, we are going straight to the result. It can be done dividing the spin orbitals in those that have spin up (α) and those that have spin down (β) and integrating over the spin coordinates. That process yields,

$$
\rho_2(\vec{r}_1,\vec{r}_2) = \frac{1}{2}\Big(\rho_1(\vec{r}_1)\rho_1(\vec{r}_2) - \rho_1^{\alpha\alpha}(\vec{r}_1,\vec{r}_2)\rho_1^{\alpha\alpha}(\vec{r}_2,\vec{r}_1) - \rho_1^{\beta\beta}(\vec{r}_1,\vec{r}_2)\rho_1^{\beta\beta}(\vec{r}_2,\vec{r}_1)\Big) \quad (7.42)
$$

Ergo, the energy can be written in terms of the electron density, such as,

$$
\begin{aligned}
E_{HF}[\rho] = &\int d\vec{r}_1 \left(-\frac{1}{2}\nabla_i^2 + \vartheta(\vec{r})\right)\rho(\vec{r}_1) + \\
&+ \frac{1}{2}\int d\vec{r}_1 d\vec{r}_2 \frac{1}{r_{12}} \left(\rho_1(\vec{r}_1)\rho_1(\vec{r}_2) - \rho_1^{\alpha\alpha}(\vec{r}_1,\vec{r}_2)\rho_1^{\alpha\alpha}(\vec{r}_2,\vec{r}_1) - \rho_1^{\beta\beta}(\vec{r}_1,\vec{r}_2)\rho_1^{\beta\beta}(\vec{r}_2,\vec{r}_1)\right) \\
&= \int d\vec{r}_1 \left(-\frac{1}{2}\nabla_i^2\right)\rho(\vec{r}_1) + \int d\vec{r}_1 \vartheta(\vec{r})\rho(\vec{r}_1) + \frac{1}{2}\int d\vec{r}_1 d\vec{r}_2 \frac{1}{r_{12}}\rho_1(\vec{r}_1)\rho_1(\vec{r}_2) + \\
&- \frac{1}{2}\int d\vec{r}_1 d\vec{r}_2 \left(\rho_1^{\alpha\alpha}(\vec{r}_1,\vec{r}_2)\rho_1^{\alpha\alpha}(\vec{r}_2,\vec{r}_1) - \rho_1^{\beta\beta}(\vec{r}_1,\vec{r}_2)\rho_1^{\beta\beta}(\vec{r}_2,\vec{r}_1)\right)
\end{aligned}
$$

where we define,

$$
\begin{aligned}
E_{HF}[\rho] &= T[\rho] + V_{ne}[\rho] + \mathscr{J}[\rho] - \mathscr{K}[\rho] && (7.43) \\
&= T[\rho] + V_{ne}[\rho] + V_{ee}[\rho] && (7.44)
\end{aligned}
$$

in which $T[\rho]$ is the the electron kinetic energy operator, $V_{ne}[\rho]$ is the interaction operator between electrons and nuclei, $\mathscr{J}[\rho]$ is the Coulomb integral and $\mathscr{K}[\rho]$ is the exchange integral.

To summarize, we have shown that for the Hartree-Fock solution to the electronic problem, we can obtain the first and second order reduced density operators in order to find its corresponding energy. Said energy can be written in terms of only the electron density. These conclusions lay the ground work to demonstrate theorems in Density Functional Theory.

7.1.2 Hohenberg-Kohn Theorems

In DFT terms, electrons interact with each other through an external potential determined by the nuclei. Here, we show that once such potential is known, the ground state electron density can be determined and, by extension, so can the system's minimum energy.

Theorem 1: for a test function $\bar{\rho}(\vec{r})$ that satisfies $\int d\vec{r}\bar{\rho}(\vec{r}) = N$, being N the number of electrons, and $\bar{\rho}(\vec{r}) \geq 0$ we have that $E[\bar{\rho}(\vec{r})] > E[\rho(\vec{r})]$, where ρ is the exact solution.

The proof follows the variational method, where it's shown that with

$$
E[\bar{\rho}(\vec{r})] = \langle\bar{\psi}|\hat{H}|\bar{\psi}\rangle \qquad\qquad E[\rho(\vec{r})] = \langle\psi|\hat{H}|\psi\rangle \tag{7.45}
$$

then, once the variational principle assures that $\langle\bar{\psi}|\hat{H}|\bar{\psi}\rangle \geq \langle\psi|\hat{H}|\psi\rangle$, necessarily, $E[\bar{\rho}(\vec{r})] \geq E[\rho(\vec{r})]$, being the equal sign valid only when $\bar{\rho}(\vec{r}) = \rho(\vec{r})$, the exact electronic density.

Theorem 2: The ground state electron density is uniquely determined by the external potential $\vartheta(\vec{r})$.

This demonstration may be done via *reductio ad absurdum*, where we show that an assumption contrary to this theorem yields an impossible result. For that, consider two different external potentials, ϑ_A and ϑ_B, that define two corresponding wave functions, ψ_A and ψ_B, that in turn, define densities ρ_A and ρ_B. From the variational method, we have that

$$\langle\psi_A|H_A|\psi_A\rangle < \langle\psi_B|H_A|\psi_B\rangle \tag{7.46}$$

where the left-hand side is

$$\langle\psi_A|H_A|\psi_A\rangle = \langle\psi_A|T|\psi_A\rangle + \langle\psi_A|V_{ee}|\psi_A\rangle + \int d\vec{r}\vartheta_A\rho_A. \tag{7.47}$$

Comparing equation (7.47) to equation (7.2), we can see that — for the same number of electrons, $N_A = N_B$ — the first and last terms in (7.2) are identical in systems A and B, i.e. $T_A = T_B = T$ and $V_{ee_A} = V_{ee_B}$. While the remaining term in (7.2) differs in A and B due to a parametric dependence on the position of the nuclei. The right-hand side in (7.46) is

$$\langle\psi_B|H_A|\psi_B\rangle = \langle\psi_B|T|\psi_B\rangle + \langle\psi_B|V_{ee}|\psi_B\rangle + \int d\vec{r}\vartheta_A\rho_B \tag{7.48}$$

leading equation (7.47) to become

$$\langle\psi_A|T|\psi_A\rangle + \langle\psi_A|V_{ee}|\psi_A\rangle + \int d\vec{r}\vartheta_A\rho_A < \langle\psi_B|T|\psi_B\rangle + \langle\psi_B|V_{ee}|\psi_B\rangle + \int d\vec{r}\vartheta_A\rho_B \tag{7.49}$$

Let us take the hypothesis where $\rho_A = \rho_B$, then equation (7.49) is reduced to

$$\langle\psi_A|T|\psi_A\rangle + \langle\psi_A|V_{ee}|\psi_A\rangle < \langle\psi_B|T|\psi_B\rangle + \langle\psi_B|V_{ee}|\psi_B\rangle. \tag{7.50}$$

Now, taking H_B and applying the same procedure we have,

$$\langle\psi_A|H_B|\psi_A\rangle > \langle\psi_B|H_B|\psi_B\rangle, \tag{7.51}$$

then

$$\langle\psi_A|T|\psi_A\rangle + \langle\psi_A|V_{ee}|\psi_A\rangle > \langle\psi_B|T|\psi_B\rangle + \langle\psi_B|V_{ee}|\psi_B\rangle . \tag{7.52}$$

Finally, comparing equations (7.50) and (7.52) we have a mathematically absurd result. Hence, the hypothesis of two different external potentials resulting in equivalent densities is denied.

We know how to write the kinetic energy operator, $\hat{T}$, and the electron-electron interaction operator, $\hat{V}_{ee}$. However, we do not know how to express them as a functional of ρ, all we known is that it is possible. It is worth noting that both operators depend on the number of electrons, N, such that is reasonable to assume that for different systems with the same N, they will have the same form. In practical terms, each system is individualized only by the electron-nucleus interaction, namely $\vartheta(\vec{r})$. The fact that we don't know how to express them as functionals individually allows for us to define $F_{HK} = T[\rho] + V_{ee}[\rho]$, which is known as Hohenberg-Kohn's universal functional. Thus, the energy in the DFT approximation can be determined as

$$E[\rho] = F_{HK}[\rho] + \int d\vec{r}\vartheta(\vec{r})\rho(\vec{r}). \tag{7.53}$$

The next step, analog to what is done in the Hartree-Fock method, is to determine the functional that minimizes the energy above. There is no explicit exact form for the functional F_{HK}. Nevertheless, the functional we want to obtain can be expressed as

$$S[\rho] = F_{HK}[\rho] + \int d\vec{r}\vartheta(\vec{r})\rho(\vec{r}) - \mu\left(\int d\vec{r}\rho(\vec{r}) - N\right) \tag{7.54}$$

where μ is a Lagrange multiplier.

Functional minimization

Consider two points in space connected by infinite different trajectories. The action S is a functional of the Lagrangian $\mathscr{L}$ in the form of

$$S[\mathscr{L}] = \int_{t_1}^{t_2} dt \mathscr{L}(x,\dot{x},t) \tag{7.55}$$

where

$$\begin{align} \mathscr{L}(x,\dot{x},t) &= T - U \tag{7.56}\\ &= \frac{1}{2}m\dot{x}^2 - U(x). \tag{7.57}\end{align}$$

One can ask the question of which $x(t)$ minimizes S, or in other words, for which $x(t)$ do we have $dS = 0$. Suppose that $x(t) \rightarrow x(t) + \varepsilon(t)$ such that,

$$\frac{dx}{dt} \rightarrow \frac{dx}{dt} + \frac{d\varepsilon}{dt} \tag{7.58}$$

with the boundary condition that $\varepsilon(t_1) = \varepsilon(t_2) = 0$. We can write

$$dS = \int_{t_1}^{t_2} dt d\mathscr{L}(x,\dot{x},t) \tag{7.59}$$

in which

$$\begin{align} d\mathscr{L} &= \frac{m}{2} \cdot 2\frac{dx}{dt}\frac{d\varepsilon}{dt} - \frac{dU}{dx}\varepsilon(t) \tag{7.60}\\ &= m\frac{dx}{dt}\frac{d\varepsilon}{dt} - \frac{dU}{dx}\varepsilon(t) \tag{7.61}\\ &= \frac{d}{dt}\left(m\frac{dx}{dt}\varepsilon\right) - m\frac{d^2x}{dt^2}\varepsilon - \frac{dU}{dx}\varepsilon \tag{7.62}\end{align}$$

From that, we can insert back into dS,

$$dS = \int_{t_1}^{t_2} dt d\mathscr{L}(x,\dot{x},t) = 0 \tag{7.63}$$

$$= \int_{t_1}^{t_2} dt \left(\frac{d}{dt} \left(m\frac{dx}{dt}\varepsilon \right) - m\frac{d^2x}{dt^2}\varepsilon - \frac{dU}{dx}\varepsilon \right) = 0 \tag{7.64}$$

$$= \int_{t_1}^{t_2} dt \left(m\frac{d^2x}{dt^2} - \frac{dU}{dx} \right) \varepsilon = 0 \tag{7.65}$$

resulting in

$$m\frac{d^2x}{dt^2} - \frac{dU}{dx} = 0 \longrightarrow -\frac{dU}{dx} = F = m\frac{d^2x}{dt^2} \tag{7.66}$$

which is a form of obtaining Newton's Second Law. The idea of minimizing an action comes in handy when working on the core theorems of DFT.

It is important to write this functional in terms of integrals in order to facilitate minimization. Moreover, equation (7.54) can be translated to

$$S[\rho] = \int d\vec{r}\rho(\vec{r})df_{HK} + \int d\vec{r}\vartheta(\vec{r})\rho(\vec{r}) - \mu\int d\vec{r}\rho(\vec{r}) + \mu N \tag{7.67}$$

$$= \int d\vec{r}\,(df_{HK} + \vartheta(\vec{r}) - \mu)\,\rho(\vec{r}) + \mu N \tag{7.68}$$

which can be compared to equation (7.55) to visualize that $\mathscr{L} = \rho(\vec{r})(df_{HK} + \vartheta(\vec{r}) - \mu)$.

Proceeding to minimize $S[\rho]$, we make $\rho(\vec{r}) \to \rho(\vec{r}) + \varepsilon(\vec{r})$ such that

$$d\mathscr{L} = \varepsilon(\vec{r})df_{HK} + \varepsilon(\vec{r})\vartheta(\vec{r}) - \varepsilon(\vec{r})\mu \tag{7.69}$$

$$= \varepsilon(\vec{r})\,(df_{HK} + \vartheta(\vec{r}) - \mu) \tag{7.70}$$

leading to

$$dS = \int d\vec{r}\varepsilon(\vec{r})\,(df_{HK} + \vartheta(\vec{r}) - \mu) = 0 \Longrightarrow df_{HK} + \vartheta(\vec{r}) = \mu. \tag{7.71}$$

Although it is an important result, equation (7.71) is vague. We are looking for the density that minimizes the energy and satisfies equation (7.71), but determining $F_{HK}[\rho]$ is still a challenge.

7.1.3 Kohn-Sham Method

The previously demonstrated theorems emphasize how the electron density determines the external potential, which then determines the Hamiltonian, which in turn, determines the wave function. However, if this algorithm is used, its final step is still to solve Schrödinger's equation for that Hamiltonian, which can be unimaginably difficult. When we refer to molecular orbitals, the difficulty in solving such system comes from the interactions between electrons, computed in $F_{HK}[\rho]$ within the Hamiltonian. In 1965, Kohn and Sham thought of a simplification of the problem by completely disregarding the electron-electron interactions. As a result, the Kohn-Sham Hamiltonian could be written simply as a sum of one-electron operators. It would have Slater determinants as eigenfunctions composed of each individual electron eigenfunctions and their eigenvalues are the sum of one-electron eigenvalues.

The Hamiltonian of an arbitrary system (we shall call it the $\mathscr{A}$ system) where electrons do not interact will be, as said before, a sum of one-electron operators,

$$\begin{aligned} H^{\mathscr{A}} &= \hat{T}_{\mathscr{A}} + \hat{V}_{\mathscr{A}} && (7.72)\\ &= \sum_{i}^{N}\left(-\frac{1}{2}\nabla_i^2 + \vartheta(\vec{r}_i)\right) && (7.73)\\ &= \sum_{i}^{N} h^{\mathscr{A}}(\vec{r}_i) && (7.74)\end{aligned}$$

where the individual one-electron Hamiltonians $h^{\mathscr{A}}$ solutions are spin orbitals (χ_i) that satisfy $h^{\mathscr{A}}(\vec{r}_i)\chi_i(\vec{x}_i) = \mathscr{E}_i\chi_i(\vec{x}_i)$. Those solutions can be combined into a Slater determinant to form the solution to $H^{\mathscr{A}}$. Naming the solution to $H^{\mathscr{A}}$ as Λ, we have

$$\Lambda(\vec{x}_1,\vec{x}_2,...,\vec{x}_N) = \frac{1}{\sqrt{N!}}\sum_{i}^{N!}(-1)^{\mathscr{P}_i}\mathscr{P}_i(\chi_1\chi_2\cdots\chi_N) \quad (7.75)$$

which satisfies $H^{\mathscr{A}}\Lambda(\vec{x}_1,\vec{x}_2,...,\vec{x}_N) = E_{\mathscr{A}}\Lambda(\vec{x}_1,\vec{x}_2,...,\vec{x}_N)$, where $E_{\mathscr{A}}$ is the energy.

The kinetic energy and electron-nucleus interactions functionals for the $\mathscr{A}$ system are

$$\begin{aligned} T_{\mathscr{A}}[\rho] &= \langle\Lambda|\,\hat{T}_{\mathscr{A}}\,|\Lambda\rangle && (7.76)\\ &= \sum_{i}^{N}\langle\chi_i|\left(-\frac{1}{2}\nabla^2\right)|\chi_i\rangle && (7.77)\end{aligned}$$

and

$$V_{\mathscr{A}}[\rho] = \langle\Lambda|\hat{V}_{\mathscr{A}}|\Lambda\rangle \tag{7.78}$$

$$= \sum_{i}^{N} \langle\chi_i|\vartheta(\vec{r}_i)|\chi_i\rangle\,. \tag{7.79}$$

Therefore, the energy is simply,

$$E_{\mathscr{A}}[\rho] = T_{\mathscr{A}}[\rho] + \int d\vec{r}\rho(\vec{r})\vartheta(\vec{r}) \tag{7.80}$$

leading to

$$S_{\mathscr{A}}[\rho] = E_{\mathscr{A}}[\rho] - \mu\left(\int d\vec{r}\rho(\vec{r}) - N\right) \tag{7.81}$$

Here we can proceed with the exact same steps done before where we turn $T_{\mathscr{A}}[\rho] = \int d\vec{r}d\tau_{\mathscr{A}}$, find $d\mathscr{L} = d\tau_{\mathscr{A}} + \vartheta(\vec{r}) - \mu$ to minimize $S_{\mathscr{A}}[\rho]$, yielding

$$\mu = d\tau_{\mathscr{A}} + \vartheta(\vec{r}). \tag{7.82}$$

Kohn and Sham's brilliance was to apply the results obtained for the $\mathscr{A}$ system to an actual molecular system. We reproduce their work below.

Kohn-Sham for a Molecular System

It is known that the missing correlation energy between anti-parallel spin orbitals in Hartree-Fock is an important flaw in their results for most molecular systems. Making an *ad-hoc* correction for such correlation in equation (7.43) we obtain the Kohn-Sham energy,

$$E_{KS}[\rho] = T[\rho] + V_{ne}[\rho] + \mathscr{J}[\rho] - \mathscr{K}[\rho] + E_{xc}[\rho] \tag{7.83}$$

$$= T[\rho] + \int d\vec{r}\rho(\vec{r})\vartheta(\vec{r}) + \mathscr{J}[\rho] - \mathscr{K}[\rho] + E_{xc}[\rho] \tag{7.84}$$

$$= T[\rho] + \int d\vec{r}\rho(\vec{r})\vartheta(\vec{r}) + V_{ee}^{KS}[\rho] \tag{7.85}$$

in which we can add $0 = T_{\mathscr{A}}[\rho] - T_{\mathscr{A}}[\rho] + \mathscr{J}[\rho] - \mathscr{J}[\rho]$ to rearrange it as,

$$E_{KS}[\rho] = T_{\mathscr{A}}[\rho] + \mathscr{J}[\rho] + (V_{ee}^{KS}[\rho] + T[\rho] - T_{\mathscr{A}}[\rho] - \mathscr{J}[\rho]) + \int d\vec{r}\rho(\vec{r})\vartheta(\vec{r}) \tag{7.86}$$

where the terms in parenthesis determine the *exchange and correlation functional*, $E_{XC}[\rho]$, leading to

$$E_{KS}[\rho] = T_{\mathscr{A}}[\rho] + \mathscr{J}[\rho] + E_{XC}[\rho] + \int d\vec{r}\rho(\vec{r})\vartheta(\vec{r}) \tag{7.87}$$

Once we have the energy of Kohn-Sham as a functional of the electron density, the next step is to minimize it. Defining

$$S_{KS}[\rho] = E_{KS}[\rho] - \mu\left(\int d\vec{r}\rho(\vec{r})\vartheta(\vec{r}) - N\right) \tag{7.88}$$

$$= \int d\vec{r}\rho(\vec{r})\left(d\tau_{\mathscr{A}} + dj + de_{xc} + \vartheta(\vec{r}) - \mu\right) + \mu N \tag{7.89}$$

$$= \int d\vec{r}\mathscr{L}_{KS} + \mu N \tag{7.90}$$

from where we can obtain,

$$dS_{KS}[\rho] = 0 = \int d\vec{r}d\mathscr{L}_{KS} \tag{7.91}$$

in which,

$$d\mathscr{L}_{KS} = \varepsilon(\vec{r})d\tau_{\mathscr{A}} + dj_{int} + \varepsilon(\vec{r})de_{xc} + \varepsilon(\vec{r})\vartheta(\vec{r}) - \mu. \tag{7.92}$$

The term dj_{int} corresponds to the integral from of $\int d\vec{r}\rho(\vec{r})dj$, which is the only one we have yet to define. In order to do that, we need to take $\mathscr{J}[\rho]$ in terms of $\rho(\vec{r})$ as defined in equation (7.43) so that we can proceed as,

$$\int d\vec{r}\rho(\vec{r})dj = \frac{1}{2}\int d\vec{r}\rho(\vec{r})\int d\vec{r}'\rho(\vec{r}')\frac{1}{|\vec{r}-\vec{r}'|} \tag{7.93}$$

and with $\rho(\vec{r}) \to \rho(\vec{r}) + \varepsilon(\vec{r})$,

$$dj_{int} = \frac{1}{2}\int d\vec{r}\varepsilon(\vec{r})\int d\vec{r}'\rho(\vec{r}')\frac{1}{|\vec{r}-\vec{r}'|} + \int d\vec{r}\rho(\vec{r})\int d\vec{r}'\varepsilon(\vec{r}')\frac{1}{|\vec{r}-\vec{r}'|} \tag{7.94}$$

$$\tag{7.95}$$

where we can exchange $\vec{r} \to \vec{r}'$ and $\vec{r}' \to \vec{r}$, to write

$$dj_{int} = \int d\vec{r}\varepsilon(\vec{r})\int d\vec{r}'\rho(\vec{r}')\frac{1}{|\vec{r}-\vec{r}'|} \tag{7.96}$$

$$\tag{7.97}$$

Placing this result in equation (7.92), we have

$$d\mathscr{L}_{KS} = \varepsilon(\vec{r})\left(d\tau_{\mathscr{A}} + \int d\vec{r}'\rho(\vec{r}')\frac{1}{|\vec{r}-\vec{r}'|} + de_{xc} + \vartheta(\vec{r}) - \mu\right) \tag{7.98}$$

yielding

$$\mu = d\tau_{\mathscr{A}} + \int d\vec{r}'\rho(\vec{r}')\frac{1}{|\vec{r}-\vec{r}'|} + de_{xc} + \vartheta(\vec{r}) \tag{7.99}$$

$$= d\tau_{\mathscr{A}} + V_{eff}(\vec{r}) \tag{7.100}$$

defining an effective potential as,

$$V_{eff}(\vec{r}) = \vartheta(\vec{r}) + de_{xc} + \int d\vec{r}'\rho(\vec{r}')\frac{1}{|\vec{r}-\vec{r}'|}. \tag{7.101}$$

Equation (7.100) can be compared to equation (7.82), which we know how to solve and has

$$\rho(\vec{r}) = \sum_i^{N_\alpha}|\psi_i^\alpha|^2 + \sum_i^{N_\beta}|\psi_i^\beta|^2 = \sum_i\sum_\omega|\psi^\omega(\vec{r})|^2 \tag{7.102}$$

as its density, in which ψ_i is the i-th spatial orbital and α and β represent the corresponding electron spin.

From equation 7.100, Kohn-Sham energy functional is

$$E_{KS}[\rho] = T_{\mathscr{A}}[\rho] + \int V_{eff}(\vec{r})\rho d\vec{r} \tag{7.103}$$

$$= \sum_i \int d\vec{x}\chi_i^*(\vec{x}) \left(-\frac{1}{2}\nabla^2\right) \chi_i(\vec{x}) + \sum_i \int d\vec{x} V_{eff}(\vec{r})\chi_i^*(\vec{x})\chi_i(\vec{x}) \tag{7.104}$$

Note that in order for us to write $T_{\mathscr{A}}[\rho]$ the way done above, it's necessary that the wave functions are orthogonal, thus,

$$\int d\vec{x}\psi_i^*(\vec{x})\psi_i(\vec{x}) = \delta_{ij} \tag{7.105}$$

meaning there is no overlap between electron orbitals. Defining the functional $\Omega[\{\psi_i\}]$ to minimize E_{KS} using the electron density restriction we have,

$$\Omega[\{\psi_i\}] = E_{KS}[\rho] - \sum_i \varepsilon_i \left(\int \psi_i^*(\vec{r})\psi_i(\vec{r})d\vec{r} - 1 \right) \tag{7.106}$$

from which we have

$$d\Omega[\{\psi_i\}] = \frac{dE_{KS}[\rho]}{d\psi_k^*} - \sum_i \varepsilon_i \psi_i(\vec{r})\delta_{ik} = 0 \tag{7.107}$$

$$= \frac{dT_{\mathscr{A}}[\rho]}{d\psi_k^*} + \frac{d}{d\psi_k^*}\int V_{eff}(\vec{r})\rho(\vec{r})d\vec{r} - \varepsilon_k\psi_k(\vec{r}) = 0 \tag{7.108}$$

where

$$\frac{dT_{\mathscr{A}}[\rho]}{d\psi_k^*} = \frac{d}{d\psi_k^*}\int \psi_i^*(\vec{r}) \left(-\frac{1}{2}\nabla^2\right) \psi_i(\vec{r}) \tag{7.109}$$

$$= -\frac{1}{2}\nabla^2\psi_k \tag{7.110}$$

and

$$\frac{d}{d\psi_k^*}\int V_{eff}(\vec{r})\rho(\vec{r})d\vec{r} = \frac{d}{d\psi_k^*}\sum_i \int V_{eff}(\vec{r})\psi_i^*(\vec{r})\psi_i(\vec{r})d\vec{r} \tag{7.111}$$

$$= V_{eff}(\vec{r})\psi_k(\vec{r}) \tag{7.112}$$

turning equation (7.108) into

$$-\frac{1}{2}\nabla^2\psi_k(\vec{r})+V_{eff}(\vec{r})\psi_k(\vec{r})=\varepsilon_k\psi_k(\vec{r}) \tag{7.113}$$

which is the single particle equation for system $\mathscr{A}$ considering $V_{\mathscr{A}}=V_{eff}$.

Note that,

$$\sum_k \varepsilon_k=\sum_k\int d\vec{r}\psi_k^*(\vec{r})\left(-\frac{1}{2}\nabla^2+V_{eff}(\vec{r})\right)\psi_k(\vec{r}) \tag{7.114}$$

$$=T_{\mathscr{A}}[\rho]+\int V_{eff}(\vec{r})\rho(\vec{r})d\vec{r} \tag{7.115}$$

in which

$$V_{eff}(\vec{r})=\vartheta(\vec{r})+\int\frac{\rho(\vec{r}')}{|\vec{r}-\vec{r}'|}+\vartheta_{XC}(\vec{r}) \tag{7.116}$$

where the second term on the right-hand side is known as the Hartree potential and the exchange and correlation term is $\vartheta_{XC}(\vec{r})\ =\ dE_{XC}[\rho]/d\rho$. It follows that the system's total energy is

$$E[\rho]=T_{\mathscr{A}}[\rho]+\mathscr{J}[\rho]+E_{XC}[\rho]+\int\vartheta(\vec{r})\rho(\vec{r})d\vec{r} \tag{7.117}$$

$$=\sum_k\varepsilon_k-\frac{1}{2}\int d\vec{r}d\vec{r}'\frac{\rho(\vec{r}')\rho(\vec{r})}{|\vec{r}-\vec{r}'|}+E_{XC}-\int d\vec{r}\vartheta_{XC}(\vec{r}). \tag{7.118}$$

Physically, that translates into the sum of orbital energies in Kohn-Sham being different than the total electronic energy.

To summarize, Kohn-Sham equations are

$$h_{KS}\psi_i(\vec{r})=\left(-\frac{1}{2}\nabla^2+V_{eff}(\vec{r})\right)\psi_i(\vec{r})=\varepsilon_k\psi_i(\vec{r}) \tag{7.119}$$

$$V_{eff}(\vec{r})=\vartheta(\vec{r})+\int\frac{\rho(\vec{r}')}{|\vec{r}-\vec{r}'|}+\vartheta_{XC}(\vec{r}) \tag{7.120}$$

$$\rho(\vec{r})=\sum_i|\psi_i(\vec{r})|^2. \tag{7.121}$$

It is important to emphasize a key difference between Hartree-Fock and Density Functional Theory. DFT itself is derived without any approximation, and, in principle, it is an exact method. However, one would need to know E_{XC} as a functional of ρ in order to solve a molecular system exactly. Even though Hohenberg-Kohn theorems guarantee the existence of a density dependent functional, they do not provide the means to find it. Hartree-Fock, on the other hand, is deliberately an approximation where we consider a single Slater determinant as sufficient solution to the electronic problem. The approximate part in DFT takes place in trying to obtain E_{XC}, whose exact form is unknown.

7.1.4 Kohn-Sham Self-Consistent Field

In practical terms of using DFT in computational packages to actually calculating electronic structure data, we follow a self consistent field methodology. First we expand Kohn-Sham orbitals in a basis set, namely $\{\phi_\theta\}$ and insert it in equation (7.119) to obtain

$$\psi_i(\vec{r}) = \sum_\theta c_{\theta i}\phi_\theta(\vec{r}) \Rightarrow h_{KS}\sum_\theta c_{\theta i}\phi_\theta(\vec{r}) = \varepsilon_i \sum_\beta c_{\theta i}\phi_\theta(\vec{r}) \tag{7.122}$$

which we can multiply by ϕ_η^* and integrate over the space to get

$$\sum_\theta \int d\vec{r}\phi_\eta^* h_{KS} c_{\theta i}\phi_\theta = \varepsilon_i \sum_\theta \int d\vec{r} c_{\theta i}\phi_\eta^*\phi_\theta = \varepsilon_i \sum_\theta S_{\eta\theta} c_{\theta i} \tag{7.123}$$

where $S_{\eta\theta}$ is the overlap between ϕ_η^* and ϕ_θ. This equation can be written as a matrix problem, as such

$$\mathbf{h}_{KS}\mathbf{C} = \varepsilon\mathbf{S}\mathbf{C} \tag{7.124}$$

As seen above, V_{eff} depends on the wave function and, consequently, depends on the chosen basis $\{\phi\}$. With a selected basis set, we create an tentative ρ which determines V_{eff}. Then, we solve equation (7.124) and determine the expansion coefficients. If the coefficients converge to the initial guessed ones, then the problem is solved. If not, the process is repeated with the new set of coefficients. This algorithm is displayed in figure 7.1.

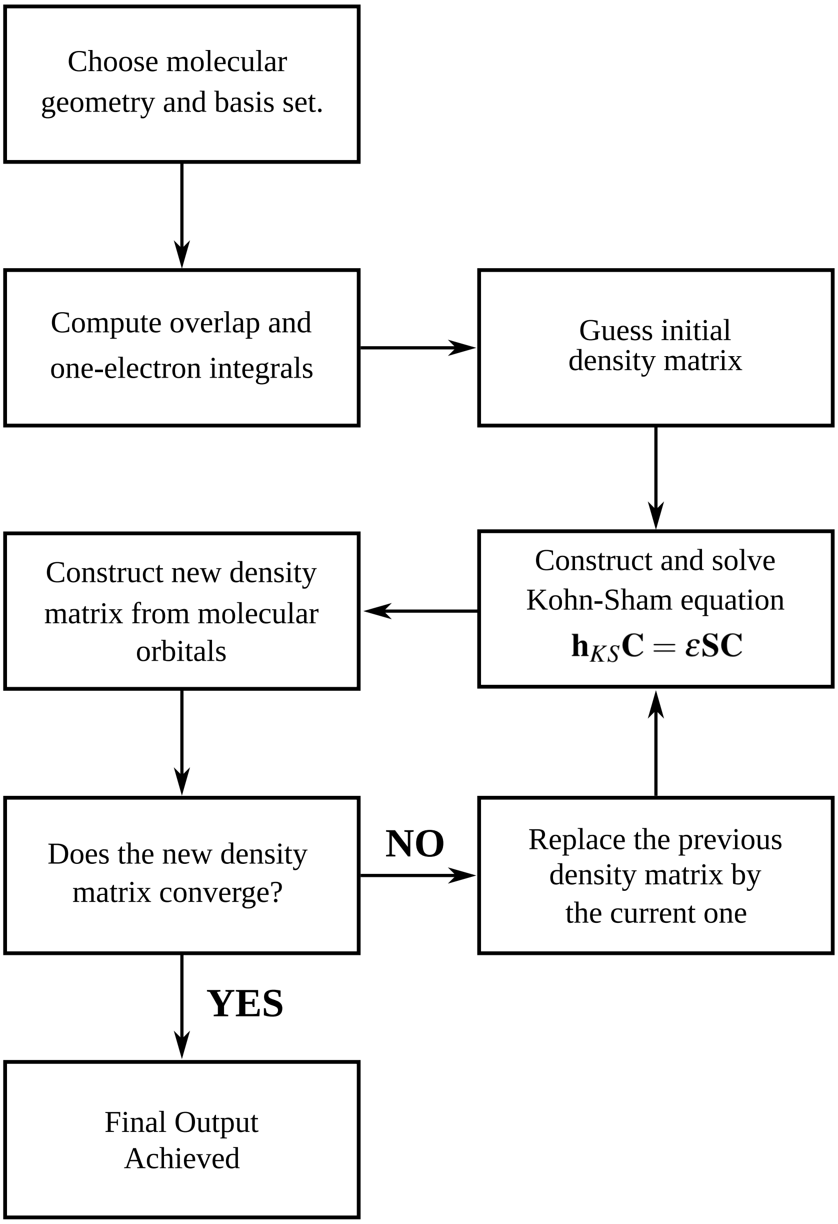

Figure 7.1: Self-consistent field methodology for Kohn-Sham equations in Density Functional Theory.

CHAPTER 8

APPENDIX C

This chapter presents the formal derivation of the density of probability for a set of independent harmonic oscillators in terms of their respective frequencies. We will take advantage of concepts related to the quantum harmonic oscillator in the context of quantum mechanics and mechanical statistics.

The density operator is

$$\hat{\rho} = \frac{e^{-\beta \hat{H}}}{tr(e^{-\beta \hat{H}})} \tag{8.1}$$

where $\beta = 1/k_B T$ (with k_B being Boltzmann's constant and T the temperature) and $\hat{H}$ being the system's Hamiltonian. In the case of the quantum harmonic oscillator we have,

$$\hat{H} = \frac{\hat{P}^2}{2m} + \frac{1}{2} m\omega^2 \hat{x}^2. \tag{8.2}$$

In the interest of avoiding orthogonal polynomials, we shall work with a non-normalized density operator, i.e. $\hat{\rho} = e^{-\beta \hat{H}}$, from which we clearly see that

$$-\frac{\partial \hat{\rho}}{\partial \beta} = \hat{H}\hat{\rho} \tag{8.3}$$

and

$$H = -\frac{\hbar^2}{2m}\frac{\partial^2}{\partial x^2} + \frac{m\omega^2}{2} x^2. \tag{8.4}$$

Our goal is to determine ρ in a tangible form, taking into account the following representations

$$\langle x|\hat{\rho}|x\rangle = \rho(x) \qquad\qquad \langle x|\hat{\rho}|x'\rangle = \rho(x,x') \tag{8.5}$$

which will be used in a ordinary first order differential equation that can be separated. Importantly, the fact that we are representing the density operator in different spaces has its peculiarities.

Before moving on, let us borrow some useful relations from quantum mechanics, them being:

$$\langle x|\hat{P}|\alpha\rangle = -i\hbar\frac{d}{dx}\langle x|\alpha\rangle \tag{8.6}$$

$$\langle\alpha|\hat{P}|x\rangle = i\hbar\frac{d}{dx}\langle\alpha|x\rangle\,. \tag{8.7}$$

From which we can obtain how the momentum operator acts over the bra and ket position spaces, like such

$$\langle x|\hat{P} = -i\hbar\frac{d}{dx}\langle x| \tag{8.8}$$

$$\hat{P}|x\rangle = i\hbar\frac{d}{dx}|x\rangle\,. \tag{8.9}$$

It is worth mentioning that, although these relations are completely analogous to each other, they show derivatives that act on completely different spaces.

Note that

$$\langle x|[\hat{P},\hat{\rho}]|x\rangle = \langle x|\hat{P}\hat{\rho}|x\rangle - \langle x|\hat{\rho}\hat{P}|x\rangle \tag{8.10}$$

$$= -i\hbar\left(\frac{d\langle x|}{dx}\hat{\rho}|x\rangle + \langle x|\hat{\rho}\frac{d|x\rangle}{dx}\right) \tag{8.11}$$

$$= -i\hbar\frac{d}{dx}(\langle x|\hat{\rho}|x\rangle) = -i\hbar\frac{d}{dx}\rho(x) \tag{8.12}$$

thus,

$$\frac{i}{\hbar}\langle x|[\hat{P},\hat{\rho}]|x\rangle = \frac{d}{dx}(\langle x|\hat{\rho}|x\rangle) \tag{8.13}$$

We can use equation 8.6 to analyze non-diagonal terms by making $|\alpha\rangle = \hat{\rho}|x'\rangle$ and equation 8.7

by making $\langle\alpha| = \langle x|\rho$ and $|x\rangle \to |x'\rangle$ to obtain

$$\langle x|\hat{P}\hat{\rho}|x'\rangle = -i\hbar\frac{d}{dx}\langle x|\hat{\rho}|x'\rangle \tag{8.14}$$

and

$$\langle x|\hat{\rho}\hat{P}|x'\rangle = i\hbar\frac{d}{dx'}\langle x|\rho|x'\rangle \tag{8.15}$$

which can be added to each other to obtain,

$$\begin{aligned} \langle x|(\hat{\rho}\hat{P}+\hat{P}\hat{\rho})|x'\rangle &= i\hbar\left[\frac{\partial}{\partial x'}(\langle x|\hat{\rho}|x'\rangle) - \frac{\partial}{\partial x}(\langle x|\hat{\rho}|x'\rangle\right] && (8.16)\\ &= -i\hbar\left[\frac{\partial}{\partial x}\rho(x,x') - \frac{\partial}{\partial x'}\rho(x,x')\right] && (8.17) \end{aligned}$$

$$\Rightarrow \frac{\partial}{\partial x}\rho(x,x') - \frac{\partial}{\partial x'}\rho(x,x') = \frac{i}{\hbar}\langle x|\{\hat{P},\hat{\rho}\}|x'\rangle \tag{8.18}$$

Now, turning our attention back to the harmonic oscillator problem we can perform the following operation,

$$\hat{P}\hat{\rho} = \hat{P}e^{-\beta\hat{H}} \Rightarrow \hat{\rho}^{-1}\hat{P}\hat{\rho} = e^{\beta\hat{H}}\hat{P}e^{-\beta\hat{H}}, \tag{8.19}$$

which can be expanded using the Baker-Hausdorff theorem,

$$e^{x}ye^{-x} = y + [x,y] + \frac{1}{2!}[x,[x,y]] + \frac{1}{3!}[x,[x,[x,y]]] + ... \tag{8.20}$$

where $x = \beta\hat{H}$ and $y = \hat{P}$ are operators, such that we get

$$e^{\beta\hat{H}}\hat{P}e^{-\beta\hat{H}} = \hat{P} + [\beta\hat{H},\hat{P}] + \frac{1}{2!}[\beta\hat{H},[\beta\hat{H},\hat{P}]] + \frac{1}{3!}[\beta\hat{H},[\beta\hat{H},[\beta\hat{H},\hat{P}]]] + ... \tag{8.21}$$

in a way that considering the Hamiltonian shown in equation 8.4, we have

$$\begin{aligned} [\beta\hat{H},\hat{P}] &= im\omega(\beta\hbar\omega)\hat{x} && (8.22)\\ [\beta\hat{H},[\beta\hat{H},\hat{P}]] &= (\beta\hbar\omega)^2\hat{P} && (8.23)\\ [\beta\hat{H},[\beta\hat{H},[\beta\hat{H},\hat{P}]]] &= im\omega(\beta\hbar\omega)^3\hat{x} && (8.24) \end{aligned}$$

bringing our expression to

$$e^{\beta\hat{H}}\hat{P}e^{-\beta\hat{H}} = \left(1+\frac{1}{2!}(\beta\hbar\omega)^2+...\right)\hat{P}+\left(\beta\hbar\omega+\frac{(\beta\hbar\omega)^3}{3!}+...\right)im\omega\hat{x} \tag{8.25}$$

$$= \hat{P}\cosh(\beta\hbar\omega)+\hat{x}im\omega\sinh(\beta\hbar\omega) \tag{8.26}$$

thus,

$$\hat{\rho}^{-1}\hat{P}\hat{\rho} = \hat{P}\cosh(\beta\hbar\omega)+\hat{x}im\omega\sinh(\beta\hbar\omega) \tag{8.27}$$

This is a powerful expression that will allow us to obtain the commutators between the momentum and density operators in terms of anti-commutators between the position and density operators. To that end, we can multiply equation 8.27 from the left by the density operator, yielding

$$\hat{\rho}\hat{\rho}^{-1}\hat{P}\hat{\rho} = \hat{P}\hat{\rho} = \hat{\rho}\hat{P}\cosh(\beta\hbar\omega)+\hat{\rho}\hat{x}im\omega\sinh(\beta\hbar\omega) \tag{8.28}$$

whose conjugated equation is,

$$\hat{\rho}\hat{P} = \hat{P}\hat{\rho}\cosh(\beta\hbar\omega)-\hat{x}\hat{\rho}im\omega\sinh(\beta\hbar\omega) \tag{8.29}$$

such that equations 8.28 and 8.29 can be subtracted to obtain

$$\hat{P}\hat{\rho}-\hat{\rho}\hat{P} = [\hat{P},\hat{\rho}] = (\hat{\rho}\hat{P}-\hat{P}\hat{\rho})\cosh(\beta\hbar\omega)+\{\hat{\rho},\hat{x}\}im\omega\sinh(\beta\hbar\omega) \tag{8.30}$$

$$[\hat{P},\hat{\rho}](1+\cosh(\beta\hbar\omega)) = im\omega\{\hat{\rho},\hat{x}\}\sinh(\beta\hbar\omega) \tag{8.31}$$

$$[\hat{P},\hat{\rho}] = im\omega\frac{\sinh(\beta\hbar\omega)}{1+\cosh(\beta\hbar\omega)}\{\hat{\rho},\hat{x}\} \tag{8.32}$$

$$\Rightarrow [\hat{P},\hat{\rho}] = im\omega\tanh\left(\frac{\beta\hbar\omega}{2}\right)\{\hat{\rho},\hat{x}\} \tag{8.33}$$

Now that we have that in hand, we can insert in equation 8.13 to obtain the differential equation that we were hoping to find so we could evaluate the diagonal terms of the density operator matrix. Doing so, one can find

$$\frac{d}{dx}\rho(x) = \frac{i}{\hbar} im\omega \tanh\left(\frac{\beta\hbar\omega}{2}\right) \langle x|\{\hat{\rho},\hat{x}\}|x\rangle \tag{8.34}$$

$$= -\frac{m\omega}{\hbar} \tanh\left(\frac{\beta\hbar\omega}{2}\right) \left(\langle x|\hat{\rho}\hat{x}|x\rangle + \langle x|\hat{x}\hat{\rho}|x\rangle\right) \tag{8.35}$$

$$= -\frac{2m\omega}{\hbar} \tanh\left(\frac{\beta\hbar\omega}{2}\right) x\rho(x) \tag{8.36}$$

which we can separate and integrate, resulting in

$$\ln\rho = -\frac{m\omega}{\hbar} \tanh\left(\frac{\beta\hbar\omega}{2}\right) x^2 + cte \tag{8.37}$$

therefore,

$$\rho(x) = cte' \exp\left[-\frac{m\omega}{\hbar} \tanh\left(\frac{\beta\hbar\omega}{2}\right) x^2\right] \tag{8.38}$$

Now this is where we can normalize it, using

$$\int \rho(x)dx = 1$$

to obtain cte', which yields the density operator for diagonal terms in its final form to be

$$\rho(x) = \sqrt{\frac{m\omega}{\pi\hbar} \tanh\left(\frac{\hbar\omega}{2k_BT}\right)} \exp\left[-\frac{m\omega}{\hbar} \tanh\left(\frac{\hbar\omega}{2k_BT}\right) x^2\right] \tag{8.39}$$

Bibliography

[1] Ullrich Mitschke and Peter Bäuerle. The electroluminescence of organic materials. Journal of Materials Chemistry, 10(7):1471–1507, 2000.

[2] Navpreet Kaur, Mandeep Singh, Dinesh Pathak, Tomas Wagner, and JM Nunzi. Organic materials for photovoltaic applications: Review and mechanism. Synthetic Metals, 190:20–26, 2014.

[3] Kyoung Soo Yook and Jun Yeob Lee. Organic materials for deep blue phosphorescent organic light-emitting diodes. Advanced materials, 24(24):3169–3190, 2012.

[4] Christoph J Brabec, Jens A Hauch, Pavel Schilinsky, and Christoph Waldauf. Production aspects of organic photovoltaics and their impact on the commercialization of devices. MRS bulletin, 30(1):50–52, 2005.

[5] Gregory D Scholes and Garry Rumbles. Excitons in nanoscale systems. Nature materials, 5(9):683–696, 2006.

[6] Jean-Luc Brédas, Joseph E Norton, Jérôme Cornil, and Veaceslav Coropceanu. Molecular understanding of organic solar cells: the challenges. Accounts of chemical research, 42(11):1691–1699, 2009.

[7] Rainer Waser and Masakazu Aono. Nanoionics-based resistive switching memories. Nature materials, 6(11):833–840, 2007.

[8] J Ross Macdonald. Impedance spectroscopy: emphasizing solid materials and systems. Applied Optics, 28(6):1083, 1989.

[9] Yasunari Tamai, Hideo Ohkita, Hiroaki Benten, and Shinzaburo Ito. Exciton diffusion in conjugated polymers: from fundamental understanding to improvement in photovoltaic conversion efficiency. The journal of physical chemistry letters, 6(17):3417–3428, 2015.

[10] Michael H Stewart, Alan L Huston, Amy M Scott, Eunkeu Oh, W Russ Algar, Jeffrey R Deschamps, Kimihiro Susumu, Vaibhav Jain, Duane E Prasuhn, Juan Blanco-Canosa, et al. Competition between forster resonance energy transfer and electron transfer in stoichiometrically assembled semiconductor quantum dot–fullerene conjugates. Acs Nano, 7(10):9489–9505, 2013.

[11] Guichuan Zhang, Francis R Lin, Feng Qi, Thomas Heumuller, Andreas Distler, Hans-Joachim Egelhaaf, Ning Li, Philip CY Chow, Christoph J Brabec, Alex K-Y Jen, et al. Renewed prospects for organic photovoltaics. Chemical Reviews, 122(18):14180–14274, 2022.

[12] CA Parker and CG Hatchard. Triplet-singlet emission in fluid solutions. phosphorescence of eosin. Transactions of the Faraday Society, 57:1894–1904, 1961.

[13] Martin Pope, Hartmut Paul Kallmann, and Peter Magnante. Electroluminescence in organic crystals. The Journal of Chemical Physics, 38(8):2042–2043, 1963.

[14] Mitsuhiro Koden. OLED displays and lighting. John Wiley & Sons, 2016.

[15] Martin Klessinger and Josef Michl. Excited states and photochemistry of organic molecules. 1995.

[16] Zhongfu An, Chao Zheng, Ye Tao, Runfeng Chen, Huifang Shi, Ting Chen, Zhixiang Wang, Huanhuan Li, Renren Deng, Xiaogang Liu, et al. Stabilizing triplet excited states for ultralong organic phosphorescence. Nature Materials, 14(7):685–690, 2015.

[17] Weijun Zhao, Zikai He, Jacky WY Lam, Qian Peng, Huili Ma, Zhigang Shuai, Gongxun Bai, Jianhua Hao, and Ben Zhong Tang. Rational molecular design for achieving persistent and efficient pure organic room-temperature phosphorescence. Chem, 1(4):592–602, 2016.

[18] Sanjoy Mukherjee and Pakkirisamy Thilagar. Recent advances in purely organic phosphorescent materials. Chemical communications, 51(55):10988–11003, 2015.

[19] Hiroki Uoyama, Kenichi Goushi, Katsuyuki Shizu, Hiroko Nomura, and Chihaya Adachi. Highly efficient organic light-emitting diodes from delayed fluorescence. Nature, 492(7428):234–238, 2012.

[20] Kenichi Goushi, Kou Yoshida, Keigo Sato, and Chihaya Adachi. Organic light-emitting diodes employing efficient reverse intersystem crossing for triplet-to-singlet state conversion. Nature Photonics, 6(4):253–258, 2012.

[21] Yoshimasa Wada, Hiromichi Nakagawa, Soma Matsumoto, Yasuaki Wakisaka, and Hironori Kaji. Organic light emitters exhibiting very fast reverse intersystem crossing. Nature Photonics, 14(10):643–649, 2020.

[22] Jamie Gibson, Andrew P Monkman, and Thomas J Penfold. The importance of vibronic coupling for efficient reverse intersystem crossing in thermally activated delayed fluorescence molecules. ChemPhysChem, 17(19):2956–2961, 2016.

[23] Hiroki Noda, Hajime Nakanotani, and Chihaya Adachi. Excited state engineering for efficient reverse intersystem crossing. Science Advances, 4(6):eaao6910, 2018.

[24] Kristofer Tvingstedt, Koen Vandewal, Abay Gadisa, Fengling Zhang, Jean Manca, and Olle Inganas. Electroluminescence from charge transfer states in polymer solar cells. Journal of the American Chemical Society, 131(33):11819–11824, 2009.

[25] Veaceslav Coropceanu, Xian-Kai Chen, Tonghui Wang, Zilong Zheng, and Jean-Luc Brédas. Charge-transfer electronic states in organic solar cells. Nature Reviews Materials, 4(11):689–707, 2019.

[26] Zbigniew R Grabowski, Krystyna Rotkiewicz, and Wolfgang Rettig. Structural changes accompanying intramolecular electron transfer: focus on twisted intramolecular charge-transfer states and structures. Chemical reviews, 103(10):3899–4032, 2003.

[27] Gloria Hong, Xuemin Gan, Céline Leonhardt, Zhen Zhang, Jasmin Seibert, Jasmin M Busch, and Stefan Bräse. A brief history of oledsemitter development and industry milestones. Advanced Materials, 33(9):2005630, 2021.

[28] Robert J Morris. Lavoisier and the caloric theory. The British Journal for the History of Science, 6(1):1–38, 1972.

[29] Hugh Longbourne Callendar. The caloric theory of heat and carnot's principle. Proceedings of the Physical Society of London, 23(1):153, 1910.

[30] Stephen G Brush. The wave theory of heat: a forgotten stage in the transition from the caloric theory to thermodynamics. The British journal for the history of science, 5(2):145–167, 1970.

[31] John Worrall. How to remain (reasonably) optimistic: scientific realism and the luminiferous ether. Cambridge University Press, 1994(1):334–342, 1994.

[32] Albert A Michelson. Art. xxi.–the relative motion of the earth and the luminiferous ether. American Journal of Science (1880-1910), 22(128):120, 1881.

[33] KVR Murthy and Hardev Singh Virk. Luminescence phenomena: an introduction. Defect and diffusion fórum, 347:1–34, 2014.

[34] Paul S Francis and Conor F Hogan. Luminescence. In Comprehensive Analytical Chemistry, volume 54, pages 343–373. Elsevier, 2008.

[35] Bernard Valeur and Mario N Berberan-Santos. A brief history of fluorescence and phosphorescence before the emergence of quantum theory. Journal of Chemical Education, 88(6):731–738, 2011.

[36] IM Campbell and Brian Arthur-Na4471 Thrush. The recombination of nitrogen atoms and the nitrogen afterglow. Proceedings of the Royal Society of London. Series A. Mathematical and Physical Sciences, 296(1445):201–221, 1967.

[37] FC Fehsenfeld, EE Ferguson, and DK Bohme. Additional flowing afterglow measurements of negative ion reactions of d-region interest. Planetary and Space Science, 17(10):1759–1762, 1969.

[38] Joseph Berkowitz, William A Chupka, and GB Kistiakowsky. Mass spectrometric study of the kinetics of nitrogen afterglow. The Journal of Chemical Physics, 25(3):457–466, 1956.

[39] Frederick Kaufman. The Air Afterglow Revisited, pages 83–100. Springer US, Boston, MA, 1973.

[40] KD Bayes and GB Kistiakowsky. On the mechanism of the lewis-rayleigh nitrogen afterglow. The Journal of Chemical Physics, 32(4):992–1000, 1960.

[41] Kai Jiang, Yuhui Wang, Zhongjun Li, and Hengwei Lin. Afterglow of carbon dots: mechanism, strategy and applications. Materials Chemistry Frontiers, 4(2):386–399, 2020.

[42] Xuepu Wang, Yan Sun, Guangming Wang, Jiuyang Li, Xun Li, and Kaka Zhang. Tadf-type organic afterglow. Angewandte Chemie International Edition, 60(31):17138–17147, 2021.

[43] Panagiotis E Keivanidis, Grigorios Itskos, Zhipeng Kan, Eduardo Aluicio-Sarduy, Hossein Goudarzi, Valentin Kamm, Frédéric Laquai, Weimin Zhang, Christoph Brabec, George Floudas, et al. Afterglow effects as a tool to screen emissive nongeminate charge recombination processes in organic photovoltaic composites. ACS applied materials & interfaces, 12(2):2695–2707, 2019.

[44] Huibin Sun, Shujuan Liu, Wenpeng Lin, Kenneth Yin Zhang, Wen Lv, Xiao Huang, Fengwei Huo, Huiran Yang, Gareth Jenkins, Qiang Zhao, et al. Smart responsive phosphorescent materials for data recording and security protection. Nature communications, 5(1):3601, 2014.

[45] Qingqing Miao, Chen Xie, Xu Zhen, Yan Lyu, Hongwei Duan, Xiaogang Liu, Jesse V Jokerst, and Kanyi Pu. Molecular afterglow imaging with bright, biodegradable polymer nanoparticles. Nature biotechnology, 35(11):1102–1110, 2017.

[46] Zejing Chen, Kenneth Yin Zhang, Xiao Tong, Yahong Liu, Changyong Hu, Shujuan Liu, Qi Yu, Qiang Zhao, and Wei Huang. Phosphorescent polymeric thermometers for in vitro and in vivo temperature sensing with minimized background interference. Advanced Functional Materials, 26(24):4386–4396, 2016.

[47] Xiaobo Zhou, Hua Liang, Pengfei Jiang, Kenneth Yin Zhang, Shujuan Liu, Tianshe Yang, Qiang Zhao, Lijuan Yang, Wen Lv, Qi Yu, et al. Multifunctional phosphorescent conjugated polymer dots for hypoxia imaging and photodynamic therapy of cancer cells. Advanced science, 3(2):1500155, 2016.

[48] Xu Zhen, Ye Tao, Zhongfu An, Peng Chen, Chenjie Xu, Runfeng Chen, Wei Huang, and Kanyi Pu. Ultralong phosphorescence of water-soluble organic nanoparticles for in vivo afterglow imaging. Advanced Materials, 29(33):1606665, 2017.

[49] Shen Xu, Runfeng Chen, Chao Zheng, and Wei Huang. Excited state modulation for organic afterglow: materials and applications. Advanced Materials, 28(45):9920–9940, 2016.

[50] Leonardo Evaristo de Sousa, Larissa dos Santos Born, Pedro Henrique de Oliveira Neto, and Piotr de Silva. Triplet-to-singlet exciton transfer in hyperfluorescent oled materials. Journal of Materials Chemistry C, 10(12):4914–4922, 2022.

[51] Dmytro Volyniuk, Vladyslav Cherpak, Pavlo Stakhira, Boris Minaev, Gleb Baryshnikov, Maryan Chapran, Ausra Tomkeviciene, Jonas Keruckas, and Juozas V Grazulevicius. Highly efficient blue organic light-emitting diodes based on intermolecular triplet–singlet energy transfer. The Journal of Physical Chemistry C, 117(44):22538–22544, 2013.

[52] Anton Kirch, Max Gmelch, and Sebastian Reineke. Simultaneous singlet–singlet and triplet–

singlet forster resonance energy transfer from a single donor material. The journal of physical chemistry letters, 10(2):310–315, 2019.

[53] Mathew D Halls, Carl P Tripp, and H Bernhard Schlegel. Structure and infrared (ir) assignments for the oled material: N, n-diphenyl-n, n-bis (1-naphthyl)-1, 1-biphenyl-4, 4 -diamine (npb). Physical Chemistry Chemical Physics, 3(11):2131–2136, 2001.

[54] Steven A Van Slyke, CH Chen, and Ching Wan Tang. Organic electroluminescent devices with improved stability. Applied physics letters, 69(15):2160–2162, 1996.

[55] RQ Zhang, CS Lee, and ST Lee. Theory of the charge-transport properties of naphthyl diamine used in organic light-emitting devices. Applied physics letters, 75(16):2418–2420, 1999.

[56] RQ Zhang, CS Lee, and ST Lee. The electronic structures and properties of alq 3 and npb molecules in organic light emitting devices: Decompositions of density of states. The Journal of Chemical Physics, 112(19):8614–8620, 2000.

[57] Jung-Sheng Lu, Hsiao-Fan Chen, Jung-Chin Kuo, Ray Sun, Chia-Yu Cheng, Yun-Shiuan Yeh, Hai-Ching Su, and Ken-Tsung Wong. Efficient solid-state white light-emitting electrochemical cells employing embedded red color conversion layers. Journal of Materials Chemistry C, 3(12):2802–2809, 2015.

[58] Wei Zhou, Moo-Chin Wang, and Xiujian Zhao. Poly (methyl methacrylate)(pmma) doped with dcjtb for luminescent solar concentrator applications. Solar Energy, 115:569–576, 2015.

[59] CH Chen, Ching Wan Tang, Jianmin Shi, and Kevin P Klubek. Recent developments in the synthesis of red dopants for alq3 hosted electroluminescence. Thin Solid Films, 363(1-2):327–331, 2000.

[60] Xun Tang, Lin-Song Cui, Hong-Cheng Li, Alexander J Gillett, Florian Auras, Yang-Kun Qu, Cheng Zhong, Saul TE Jones, Zuo-Quan Jiang, Richard H Friend, et al. Highly efficient luminescence from space-confined charge-transfer emitters. Nature Materials, 19(12):1332–1338, 2020.

[61] Christian Reichardt. Solvatochromic dyes as solvent polarity indicators. Chemical reviews, 94(8):2319–2358, 1994.

[62] Andrey S Klymchenko. Solvatochromic and fluorogenic dyes as environment-sensitive probes: design and biological applications. Accounts of chemical research, 50(2):366–375, 2017.

[63] Leonardo Evaristo de Sousa and Piotr de Silva. Photophysics of solvated molecules: Computational protocol combining nuclear ensemble and nonequilibrium state-specific solvation methods. The Journal of Physical Chemistry A, 2023.

[64] Eric R Heller and Jeremy O Richardson. Semiclassical instanton formulation of marcus–levich–jortner theory. The Journal of Chemical Physics, 152(24), 2020.

[65] Leonardo Evaristo de Sousa, Luiz Antonio Ribeiro, Antonio Luciano de Almeida Fonseca, and Demetrio Antonio da Silva Filho. Modeling the emission spectra of organic molecules: a competition between franck–condon and nuclear ensemble methods. The Journal of Physical Chemistry A, 120(27):5380–5388, 2016.

[66] Fernando Bernardi, Massimo Olivucci, and Michael A Robb. Potential energy surface crossings in organic photochemistry. Chemical Society Reviews, 25(5):321–328, 1996.

[67] Boris Minaev, Gleb Baryshnikov, and Hans Agren. Principles of phosphorescent organic light emitting devices. Physical Chemistry Chemical Physics, 16(5):1719–1758, 2014.

[68] Yihan Shao, Zhengting Gan, Evgeny Epifanovsky, Andrew TB Gilbert, Michael Wormit, Joerg Kussmann, Adrian W Lange, Andrew Behn, Jia Deng, Xintian Feng, et al. Advances in molecular quantum chemistry contained in the q-chem 4 program package. Mol. Phys., 113(2):184–215, 2015.

[69] David L Dexter. A theory of sensitized luminescence in solids. The journal of chemical physics, 21(5):836–850, 1953.

[70] Volkhard May and Oliver Kühn. Charge and energy transfer dynamics in molecular systems. John Wiley & Sons, 2008.

[71] Th Förster. Zwischenmolekulare energiewanderung und fluoreszenz. Annalen der physik, 437(1-2):55–75, 1948.

[72] Anna Köhler and Heinz Bässler. Electronic processes in organic semiconductors: An introduction. John Wiley & Sons, 2015.

[73] Aurora Munoz-Losa, Carles Curutchet, Brent P Krueger, Lydia R Hartsell, and Benedetta Mennucci. Fretting about fret: failure of the ideal dipole approximation. Biophysical journal, 96(12):4779–4788, 2009.

[74] Kim F Wong, Biman Bagchi, and Peter J Rossky. Distance and orientation dependence of excitation transfer rates in conjugated systems: beyond the förster theory. The Journal of Physical Chemistry A, 108(27):5752–5763, 2004.

[75] Leonardo Sousa, Fernando Teixeira Bueno, Geraldo Magela e Silva, DEMETRIO A DA SILVA FILHO, and Pedro Henrique Neto. Fast predictions of exciton diffusion length in organic materials. Journal of Materials Chemistry C, 2019.

[76] Shane R Yost, Eric Hontz, Sina Yeganeh, and Troy Van Voorhis. Triplet vs singlet energy transfer in organic semiconductors: the tortoise and the hare. The Journal of Physical Chemistry C, 116(33):17369–17377, 2012.

[77] John S Sears, Thomas Koerzdoerfer, Cai-Rong Zhang, and Jean-Luc Brédas. Communication: Orbital instabilities and triplet states from time-dependent density functional theory and long-range corrected functionals. The Journal of chemical physics, 135(15), 2011.

[78] Rolf Seeger and John A Pople. Self-consistent molecular orbital methods. xviii. constraints and stability in hartree–fock theory. The Journal of Chemical Physics, 66(7):3045–3050, 1977.

[79] Andreas Dreuw and Martin Head-Gordon. Single-reference ab initio methods for the calculation of excited states of large molecules. Chemical reviews, 105(11):4009–4037, 2005.

[80] Ola B Lutnæs, Trygve Helgaker, and Michał Jaszuński. Spin–spin coupling constants and triplet instabilities in kohn–sham theory. Molecular Physics, 108(19-20):2579–2590, 2010.

[81] So Hirata and Martin Head-Gordon. Time-dependent density functional theory within the tamm–dancoff approximation. Chem. Phys. Lett., 314(3-4):291–299, 1999.

[82] Michael JG Peach, Matthew J Williamson, and David J Tozer. Influence of triplet instabilities in tddft. J. Chem. Theory Comput., 7(11):3578–3585, 2011.

[83] Agisilaos Chantzis, Adèle D Laurent, Carlo Adamo, and Denis Jacquemin. Is the tamm-dancoff approximation reliable for the calculation of absorption and fluorescence band shapes? J. Chem. Theory Comput., 9(10):4517–4525, 2013.

[84] Gaussian 16 | gaussian.com. `https://gaussian.com/gaussian16/`. (Accessed on 05/16/2022).

[85] Tamar Stein, Leeor Kronik, and Roi Baer. Reliable prediction of charge transfer excitations in molecular complexes using time-dependent density functional theory. Journal of the American Chemical Society, 131(8):2818–2820, 2009.

[86] Jan-Michael Mewes, Zhi-Qiang You, Michael Wormit, Thomas Kriesche, John M Herbert, and Andreas Dreuw. Experimental benchmark data and systematic evaluation of two a posteriori, polarizable-continuum corrections for vertical excitation energies in solution. The Journal of Physical Chemistry A, 119(21):5446–5464, 2015.

[87] Zhi-Qiang You, Jan-Michael Mewes, Andreas Dreuw, and John M Herbert. Comparison of the marcus and pekar partitions in the context of non-equilibrium, polarizable-continuum solvation models. The Journal of Chemical Physics, 143(20), 2015.

[88] Marco Caricato, Benedetta Mennucci, Jacopo Tomasi, Francesca Ingrosso, Roberto Cammi, Stefano Corni, and Giovanni Scalmani. Formation and relaxation of excited states in solution: A new time dependent polarizable continuum model based on time dependent density functional theory. The Journal of chemical physics, 124(12), 2006.

[89] Ciro A Guido, Denis Jacquemin, Carlo Adamo, and Benedetta Mennucci. Electronic excitations in solution: the interplay between state specific approaches and a time-dependent density functional theory description. Journal of chemical theory and computation, 11(12):5782–5790, 2015.

[90] Ciro Guido and Stefano Caprasecca. Corrected linear response state-specific correction to solvent polarization responsex, 2016.

[91] Marco Caricato. Absorption and emission spectra of solvated molecules with the eom–ccsd–pcm method. Journal of chemical theory and computation, 8(11):4494–4502, 2012.

[92] Gregory D Scholes. Long-range resonance energy transfer in molecular systems. Annual review of physical chemistry, 54(1):57–87, 2003.

[93] Hedi Mattoussi, Hideyuki Murata, Charles D Merritt, Yasuhiro Iizumi, Junji Kido, and Zakya H Kafafi. Photoluminescence quantum yield of pure and molecularly doped organic solid films. Journal of Applied Physics, 86(5):2642–2650, 1999.

[94] Dong-Seok Leem, Hyung-Dol Park, Jae-Wook Kang, Jae-Hyun Lee, Ji Whan Kim, and Jang-Joo Kim. Low driving voltage and high stability organic light-emitting diodes with rhenium oxide-doped hole transporting layer. Applied Physics Letters, 91(1):011113, 2007.

[95] José CS Costa, Adélio Mendes, and Luís MNBF Santos. Thin film deposition of organic hole transporting materials: optical, thermodynamic and morphological properties of naphthyl-substituted benzidines. Journal of Materials Science, 53(18):12974–12987, 2018.

[96] Caterin Salas Redondo, Paul Kleine, Karla Roszeitis, Tim Achenbach, Martin Kroll, Michael Thomschke, and Sebastian Reineke. Interplay of fluorescence and phosphorescence in organic biluminescent emitters. The Journal of Physical Chemistry C, 121(27):14946–14953, 2017.

[97] Denghui Xu, Zhenbo Deng, Ying Xu, Jing Xiao, and Chunjun Liang. Bright red-to-yellow organic light-emitting devices based on polarization-induced spectral shifts and broadening. Displays, 26(4-5):185–189, 2005.

[98] V Bulović, A Shoustikov, MA Baldo, E Bose, VG Kozlov, ME Thompson, and SR Forrest. Bright, saturated, red-to-yellow organic light-emitting devices based on polarization-induced spectral shifts. Chemical Physics Letters, 287(3-4):455–460, 1998.

[99] Conor F Madigan and Vladimir Bulović. Solid state solvation in amorphous organic thin films. Physical review letters, 91(24):247403, 2003.

[100] Nae Aota, Riku Nakagawa, Leonardo Evaristo de Sousa, Norimitsu Tohnai, Satoshi Minakata, Piotr de Silva, and Youhei Takeda. Anion-responsive colorimetric and fluorometric red-shift in triarylborane derivatives: Dual role of phenazaborine as lewis acid and electron donor. Angewandte Chemie, 136(24):e202405158, 2024.

[101] Guishan Peng, Jianan Dai, Ri Zhou, Guannan Liu, Xiaomin Liu, Xu Yan, Fangmeng Liu, Peng Sun, Chenguang Wang, and Geyu Lu. Highly efficient red/nir-emissive fluorescent probe with polarity-sensitive character for visualizing cellular lipid droplets and determining their polarity. Analytical Chemistry, 94(35):12095–12102, 2022.

[102] Lu Liu, Yaya Zhang, Jia Zhou, Jihuan Yang, Cheng Zhong, Yueshou Zhang, Yu Luo, Yang Fu, Jing Huang, Zhibin Song, et al. Design of a quinazolinone-based environment-sensitive fluorescent dye: Solvatochromic fluorescence and application for one-photon and two-photon bioimaging. Dyes and Pigments, 165:58–64, 2019.

[103] Spec2epsilon - estimate dielectric constants from fluorescence spectra. https://github.com/LeonardoESousa/spec2epsilon.

[104] Nemo - photophysics with the nuclear ensemble method. https://github.com/LeonardoESousa/NEMO.

[105] Yi Luo, Hans Ågren, and Kurt V Mikkelsen. Unique determination of the cavity radius in onsager reaction field theory. Chemical physics letters, 275(3-4):145–150, 1997.

[106] Noboru Mataga, Yozo Kaifu, and Masao Koizumi. The solvent effect on fluorescence spectrum, change of solute-solvent interaction during the lifetime of excited solute molecule. Bulletin of the Chemical Society of Japan, 28(9):690–691, 1955.

[107] Roberto Cammi, S Corni, Benedetta Mennucci, and J Tomasi. Electronic excitation energies of molecules in solution: State specific and linear response methods for nonequilibrium continuum solvation models. The Journal of chemical physics, 122(10), 2005.

[108] Ciro A Guido, Pietro Cortona, Benedetta Mennucci, and Carlo Adamo. On the metric of charge transfer molecular excitations: a simple chemical descriptor. Journal of chemical theory and computation, 9(7):3118–3126, 2013.

[109] Ernst Lippert. Dipolmoment und elektronenstruktur von angeregten molekülen. Zeitschrift für Naturforschung A, 10(7):541–545, 1955.

[110] E von Lippert. Spektroskopische bestimmung des dipolmomentes aromatischer verbindungen im ersten angeregten singulettzustand. Zeitschrift für Elektrochemie, Berichte der Bunsengesellschaft für physikalische Chemie, 61(8):962–975, 1957.

[111] Alan R Katritzky, Dan C Fara, Hongfang Yang, Kaido Tämm, Tarmo Tamm, and Mati Karelson. Quantitative measures of solvent polarity. Chemical reviews, 104(1):175–198, 2004.

[112] Chr Reichardt. Empirical parameters of the polarity of solvents. Angewandte Chemie International Edition in English, 4(1):29–40, 1965.

[113] Xiaoyi Zhang, Margaret M Cunningham, and Robert A Walker. Solvent polarity at polar solid surfaces: The role of solvent structure. The Journal of Physical Chemistry B, 107(14):3183–3195, 2003.

[114] Md Tabil Ahammed, Molay Das, MD Anwar Sadath, MD Anwar Hossain, Mehedi Hasan Kaium, MD Ahasan Ali, MD Shamsul Islam, and Chinmoy Das. Design of porous core fiber for terahertz regime using zeonex. In 2021 4th International Conference on Computing and Communications Technologies (ICCCT), pages 538–543. IEEE, 2021.

[115] Pierre Ferdinand Bissi Nyandou, Ali Raza Ayub, Patrick Noudem, Côme Damien Désiré Mveme, David Fouejio, and Serge Sylvain Zekeng. Intrinsic electro-optical and thermodynamic properties of 4, 4-bis (n-carbazolyl)-1, 1-biphenyl (cbp) as a potential candidate for nonlinear optical applications: a dft investigation. Discover Applied Sciences, 7(7):1–24, 2025.

[116] Johannes Brandrup, Edmund H Immergut, Eric A Grulke, Akihiro Abe, and Daniel R Bloch. Polymer handbook, volume 89. Wiley New York, 1999.

[117] Jaijanarthanan Lingagouder, Nae Aota, Riku Nakagawa, Beata Luszczynska, Satoshi Minakata, Leonardo Evaristo de Sousa, Piotr de Silva, Przemyslaw Data, and Youhei Takeda. Thermally activated delayed fluorescence of dibenzophenazine-cored phenazaborines in solid state: Anion modulation of photophysics. The Journal of Physical Chemistry C, 128(39):16805–16812, 2024.

[118] Irina Yu Yanina, Ekaterina N Lazareva, and Valery V Tuchin. Refractive index of adipose tissue and lipid droplet measured in wide spectral and temperature ranges. Applied optics, 57(17):4839–4848, 2018.

[119] Xcharge: A kinetic monte carlo model for exciton and charge dynamics. https://github.com/LeonardoESousa/xcharge.